8-9-2014

GALAXIES IN ABSORPTION: A STUDY OF CHEMICAL AND KINEMATIC PROPERTIES OF SUB-DAMPED LYMAN-ALPHA QUASAR ABSORBERS

Debopam Som
University of South Carolina - Columbia

GALAXIES IN ABSORPTION: A STUDY OF CHEMICAL AND KINEMATIC PROPERTIES OF SUB-DAMPED LYMAN-ALPHA QUASAR ABSORBERS

by

Debopam Som

Bachelor of Science
University of Calcutta, 2004

Master of Science
Indian Institute of Technology Delhi, 2006

Submitted in Partial Fulfillment of the Requirements

for the Degree of Doctor of Philosophy in

Physics

College of Arts and Sciences

University of South Carolina

2014

Accepted by:

Varsha P. Kulkarni, Major Professor

Kuniharu Kubodera, Committee Member

Richard J. Creswick, Committee Member

George Chartas, Committee Member

Lacy Ford, Vice Provost and Dean of Graduate Studies

Dedication

This work is dedicated to Bhalomama who introduced me to the wonderful world of mathematics. I shall, always, do my best to make you proud. I dedicate my dissertation also to Ma, Baba and Somprova. Success is meaningful only when I share it with you.

Acknowledgments

I would like to express my gratitude to all without whose help and support this work would not be possible. First and foremost, I wish to thank my advisor, Dr. Varsha P. Kulkarni, for her tutelage, patience, encouragement and constant support. I would like to thank the members of my dissertation committee, Dr. Kuniharu Kubodera, Dr. Richard Creswick, and Dr. George Chartas for their time, interest and valuable suggestions. I am greatly indebted to my collaborators, Dr. Joseph Meiring, Dr. Donald York, Dr. Celine Péroux, and Dr. Jim Lauroesch who helped me immeasurably with this work. I am grateful to my parents and my wife for their patient understanding and unwavering support: Ma, Baba and Somprova, I can not really thank you enough.

I would like to thank all the present and former graduate students in our Astronomy group, especially, Sean Morrison, Francie Cashman, Dr. Lorrie Straka, and Dr. Soheila Gharanfoli, for their friendship, collaboration and encouragement. I gratefully acknowledge Dr. Monique Aller (former postdoctoral researcher in our group), Bryan DeMarcy, and Franco Godoy for their help with my work. I would like to express my gratitude towards National Science Foundation, National Aeronautics and Space Administration, Space Telescope Science Institute, and National Optical Astronomy Observatory for providing support to this work. Finally, I sincerely thank the staff at the Las Campanas Observatory for their help in carrying out the observations that this work is largely based upon.

Abstract

Study of the chemical composition of the interstellar medium (ISM) in galaxies over cosmic time is essential for a coherent understanding of galaxy formation and evolution. Absorption lines in the spectra of quasars can be used as powerful, luminosity-independent probes of the properties of gas in and around galaxies and have been used extensively to study galaxies, the circumgalactic medium (CGM) and the intergalactic medium (IGM). The Damped Lyman-α systems (DLAs), with neutral hydrogen column densities of log $N_{HI} \gtrsim 20.3$, and sub-Damped Lyman-α systems (sub-DLAs) with $19.0 \lesssim \log N_{HI} < 20.3$ are the highest N_{HI} quasar absorbers and contain the most of the neutral gas available for star formation in the high-redshift Universe. These systems are believed to trace the progenitors of present-day galaxies and accurately probe chemical abundances in the ISM over $\sim 90\%$ of the cosmic history. In contradiction with the cosmic chemical evolution models which predict the mean metallicity of galaxies to rise from low metallicities at high-z to a near-solar level at $z \sim 0$, the DLAs are typically found to be metal-poor at all redshifts, showing little or no evolution. Interestingly, past work showed that the sub-DLAs at $0.6 \lesssim z \lesssim 1.5$ are more metal-rich on average than DLAs, and evolve consistently with the chemical evolution models in this redshift range. This suggests that the DLAs and sub-DLAs may be tracing the progenitors of different populations of present-day galaxies. However, chemical evolution of sub-DLAs is poorly constrained outside of the redshift range $0.6 < z < 1.5$ which hinders a better understanding of galaxy evolution traced by DLAs and sub-DLAs.

This dissertation presents chemical abundance measurements of sub-DLA quasar

absorbers at $z < 0.6$ and $z > 1.5$. The low-z absorbers were studied using medium-resolution UV spectra from the Cosmic Origins Spectrograph on board the Hubble Space Telescope. The systems at $z > 1.5$ were observed with the Magellan Inamori Kyocera Echelle spectrograph at the Magellan-Clay Telescope. Lines of various elements in several ionization stages, present in these spectra, were measured to determine the respective column densities. The metallicity of the absorbing gas was inferred from the nearly undepleted elements Zn or S, and several of the absorbers were found to be near-solar or super-solar in metallicity. We have also investigated the effect of ionization on the observed abundances using photoionization modelling. We find that some of the sub-DLAs have significant amounts of ionized gas, but the ionization corrections to metallicity for all of our sub-DLAs are relatively modest ($\lesssim$0.2 dex). Combining our data with other sub-DLA and DLA data from the literature, we report the most complete existing determination of the metallicity vs. redshift relation for sub-DLAs and DLAs. This work confirms, over a larger redshift baseline, the suggestion from previous investigations that sub-DLAs are, on average, more metal-rich than DLAs and evolve marginally faster. We also find evidence for metallicity being anti-correlated with H I column density in DLAs and sub-DLAs. The relative abundances and abundance ratios seen in these absorbers are discussed in the context of the overall trends seen in quasar absorbers. We have explored the kinematic properties of DLAs and sub-DLAs determined via velocity width measurements of unsaturated absorption lines. We also present initial evidence for higher interstellar cooling rates in metal-rich sub-DLAs than those seen in DLAs. Our findings suggest that DLAs and sub-DLAs may trace different galaxy populations with sub-DLAs being the progenitors of more massive galaxies.

Table of Contents

List of Tables

List of Figures

CHAPTER 1

Introduction

To decipher how our Cosmos unfolded from the featureless 'dark ages' to the present state dominated by large structures has been one of the most fascinating quests of the human mind. Over the last few decades we have made significant advances towards obtaining a coherent picture of galaxy formation and evolution with the help of observational surveys and theoretical models. However, we are yet to obtain a clear understanding of various important aspects such as the epoch at which the very first galaxies started to form; the density and temperature of the gas from which these galaxies were born; the morphologies and chemical contents of the earliest galaxies and the roles played by star formation and gas flows in the evolution of galaxies. In our search to find the answers to these questions, important clues can come from a robust understanding of the properties of gas in and around galaxies at all epochs. The vast expanse between the stars in the Milky Way as well as other galaxies is permeated by interstellar gas which acts as a crucial link in the continuous cycle of star formation from one generation of stars to the next. Consequently, the properties (especially the chemical makeup) of the 'interstellar medium' (ISM) of a galaxy provide important information regarding its star formation and accretion history.

This chapter briefly describes the physical structure of Milky Way's ISM (section 1.1) and provides a discussion on various processes responsible for the chemical

enrichment of interstellar gas in general (section 1.2). Section 1.3 discusses the basics of galactic chemical evolution models. Section 1.4 introduces some of the physical processes governing the interaction of photons with interstellar gas and the resulting observables.

1.1 Structure of the ISM

The Milky Way's ISM is a complex system. The majority of the ISM's mass is in the form of neutral Hydrogen gas, but there are several other important components of the ISM that determine its physical and chemical properties: stellar winds and supernovae 'pollute' the ISM with elements heavier than Hydrogen and Helium which control the temperature of the gas and govern the chemical makeup of the next generation of stars; cosmic rays (high energy particles) stream through the ISM constantly; magnetic fields penetrate deep into gas clouds; photons of Galactic and extragalactic origins interact with atoms triggering transitions between various energy states and also ionizing them; and dust grains extinguish the radiation and act as the sites of chemical reactions. The cosmic microwave background (CMB) photons, although relatively unimportant in affecting the behavior of the ISM, are also present. The ISM can be broadly separated into the following phases based on temperature and density (see Spitzer 1978 for a more detailed description):

- Cold Neutral Medium - T$\sim$100 K with typical particle number densities n $\sim$50 cm^{-3}. This component is usually found in the plane of the Milky Way.
- Warm Neutral Medium - This phase, with $n \sim 1$ cm^{-3} and T$\sim$ 6000 K, comprises $\sim$50% of the volume of the Milky Way and is located mainly in the disk.
- Warm Ionized Medium - This phase densities of n $\sim$0.1 cm^{-3} in diffuse gas to $n \sim 10^4$ cm^{-3} in H II regions and T$\sim 10^4$ K, and is found in the disk and halo

of the Milky Way.

- Hot ISM - Typically found in the halo of Milky Way, this component of the ISM is extremely hot and diffuse (n ∼0.001 cm^{-3}, T∼10^6 K).

- Molecular Clouds - This phase of the ISM is comprised of gas mostly in the molecular form. These regions are highly dense ($n \sim 10^6$ cm^{-3}) and cold with temperatures of the order T∼30 K. These molecular clouds are also usually very dusty with high levels of light extinction at visual wavelengths. This, however is a temporary phase existing right before the first stages of star formation.

1.2 Chemical Enrichment Mechanisms

Shortly after the Big Bang the temperature of the Universe fell to $\sim 10^9$ K, allowing stable Hydrogen nuclei to exist while remaining high enough for fusion reactions between Hydrogen nuclei to proceed. At the same time, the Universe was too cold for proton-neutron inter-conversions through weak interactions and for fusion reactions between nuclei of higher atomic numbers requiring much higher energies. As a result, the big bang nucleosynthesis produced baryonic matter only in the form of Hydrogen, Helium and trace amounts of Lithium. As the Universe continued to evolve to form stars and galaxies, favorable conditions for the nuclear reactions producing heavier elements emerged and all of the "metals" (elements heavier than H and He in the parlance of Astronomy) were synthesized by stars of different masses in various stages of their lives. There are three main mechanisms for the production of metals:

- **Charged Particle Fusion:** Fusion reactions in the cores of stars that produce energy to stabilize the stars against gravity are also responsible for the production of nearly all of the elements up to the Fe peak nuclei (Z$\lesssim$30). Fusion of heavier nuclei require higher energy in comparison with fusion of lighter species

and as stellar core temperatures increase with mass, the elements synthesized in a star depends on its mass. While a solar mass star produces mainly He and C during its lifetime, stars with M>8-10 $M_{\odot}$ are massive enough to fuse the Fe peak elements in their cores. The Fe peak elements have the most tightly bound nuclei, i.e. the highest binding energy per nucleon. As a result, further fusion reactions become endothermic and unsustainable. At the temperatures typical of stellar interiors, charged particle fusion of elements with higher Z than the Fe peak species becomes no longer feasible due to enhanced Coulomb repulsion between the nuclei.

- **The s-process:** The s-process is a synthesis mechanism for elements with Z>30 via neutron capture. The s-process takes place when neutrons are freed during fusion reactions such as

$$^{22}_{10}\mathrm{Ne} + \alpha \rightarrow ^{25}_{12}\mathrm{Mg} + n - 0.48\ \mathrm{MeV}, \tag{1.1}$$

$$^{13}_{6}\mathrm{C} + \alpha \rightarrow ^{16}_{8}\mathrm{O} + n - 0.91\ \mathrm{MeV}, \tag{1.2}$$

in massive stars and are later captured. Unlike the charged particles, these free neutrons are not impeded by the coulomb barriers of Fe peak nuclei. The characteristic timescale for the addition of free neutrons is longer than the subsequent β-decay rates and therefore it is called a 'slow' process. The s-process occurs primarily in highly evolved intermediate mass and massive stars on the Asymptotic Giant Branch (AGB) during thermal pulsations.

- **The r-process:** Most of the heaviest elements are produced in supernovae explosions via the r-process. The explosions produce extremely high densities ($\sim 10^{23}$ cm^{-3}) of free neutrons through electron capture reactions such as

$$p + e \rightarrow n + \nu_e. \tag{1.3}$$

Unstable neutron rich isotopes are produced, through neutron capture, from the rapid accumulation of free neutrons before β-decay can occur. With the eventual subsidence of the flux of free neutrons the unstable isotopes decay into more stable nuclei (see e.g., Pagel 1997 for a more detailed discussion of the s and r processes).

Different elements produced in these processes are released into the ISM on different timescales which depend on the production, ejection and mixing mechanisms. The interstellar gas, in turn, contributes material for the formation of the next generation of stars and the chemical evolution of the galaxy continues in this cyclical process (see Fig. 1.1). The main processes responsible for the injection of heavy elements into the ISM are stellar winds and supernova explosions.

Thermal pulsations at the end of the lives of intermediate mass stars ($\lesssim 10 M_\odot$) give rise to stellar winds. The expanding outer shells of these dying stars carry the elements produced in nuclear fusion and are commonly known as 'planetary nebulae' (see Fig. 1.2). The shells expand at a typical rate of $\sim$10 km s^{-1}, eventually (after $\sim$ 20,000 years) diffusing into the ISM and fading away from visibility. The progenitors of planetary nebulae, being low mass stars, mainly release light elements such as He, C, N, and O (van den Hoek & Groenewgen, 1997) into the ISM and the heavier elements are not produced in significant quantities (see e.g., van den Hoek & Groenewgen 1997; Karakas & Lattanzio 2007 for discussions on elemental yields of planetary nebulae). The timescale of chemical enrichment through stellar winds depends on progenitor masses. However, since the process can only start after the progenitor evolves off the main sequence, the typical timescale is $\gtrsim 10^8$ years for the generally low-mass progenitors.

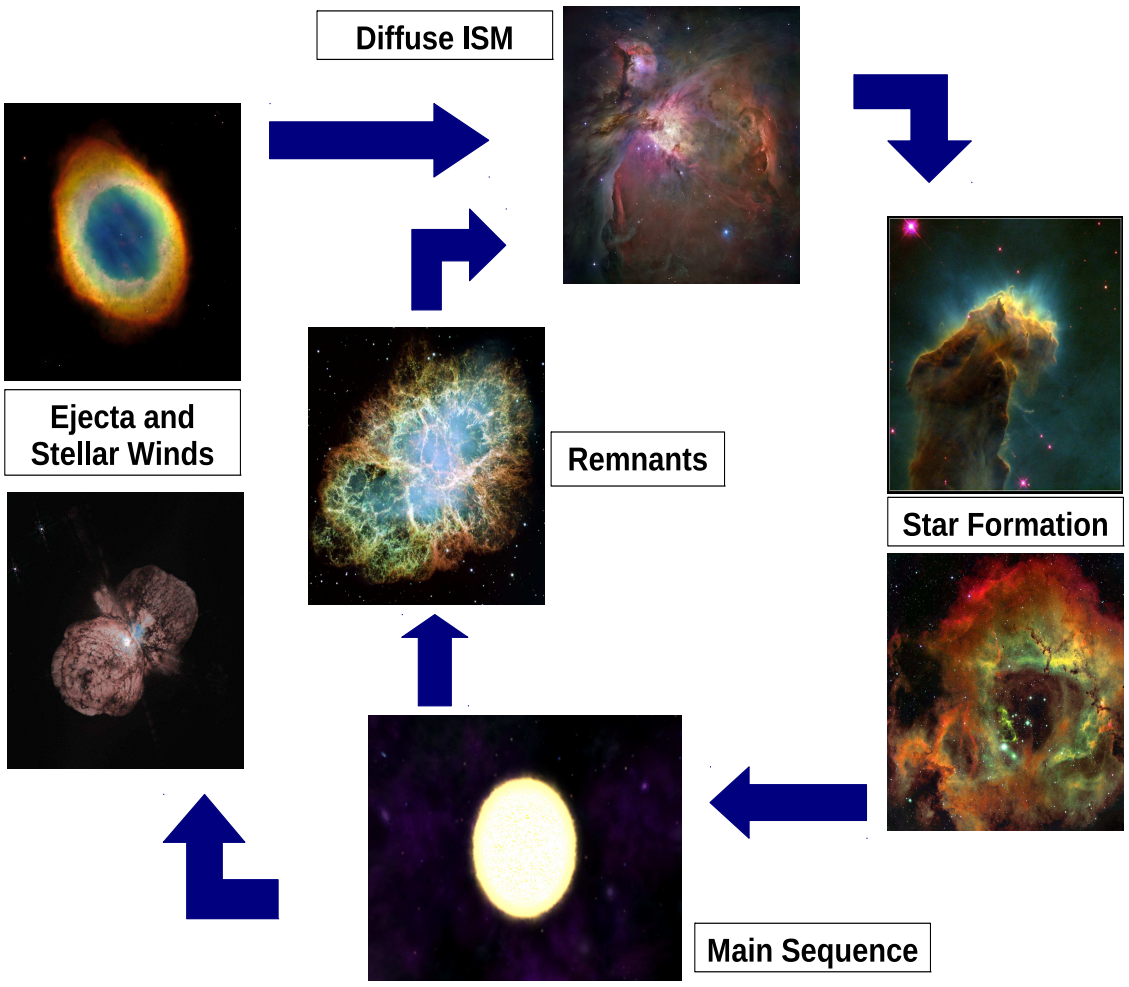

Figure 1.1 A schematic representation of how star formation cycles in galaxies connect stars with the chemical enrichment of the interstellar medium.

Supernova explosions can be classified into two groups based on the presence or absence of absorption lines of Hydrogen in their optical spectra; Type I (no Hydrogen lines) and Type II (Hydrogen lines are present). Type I supernovae can again be subdivided into three classes; Types Ia, Ib and Ic, based on absorption lines (from Silicon and Helium) in their optical spectra. Type Ia supernovae are believed to be caused by the accretion of material from a red giant onto a white dwarf in a binary system. All other classes (Ib, Ic, II) are believed to result from the collapse of cores in massive ($M \gtrsim 10M_{\odot}$) stars at the end of their lives. Due to the difference in progenitor masses, the nucleosynthetic yields and timescales of type Ia and type II

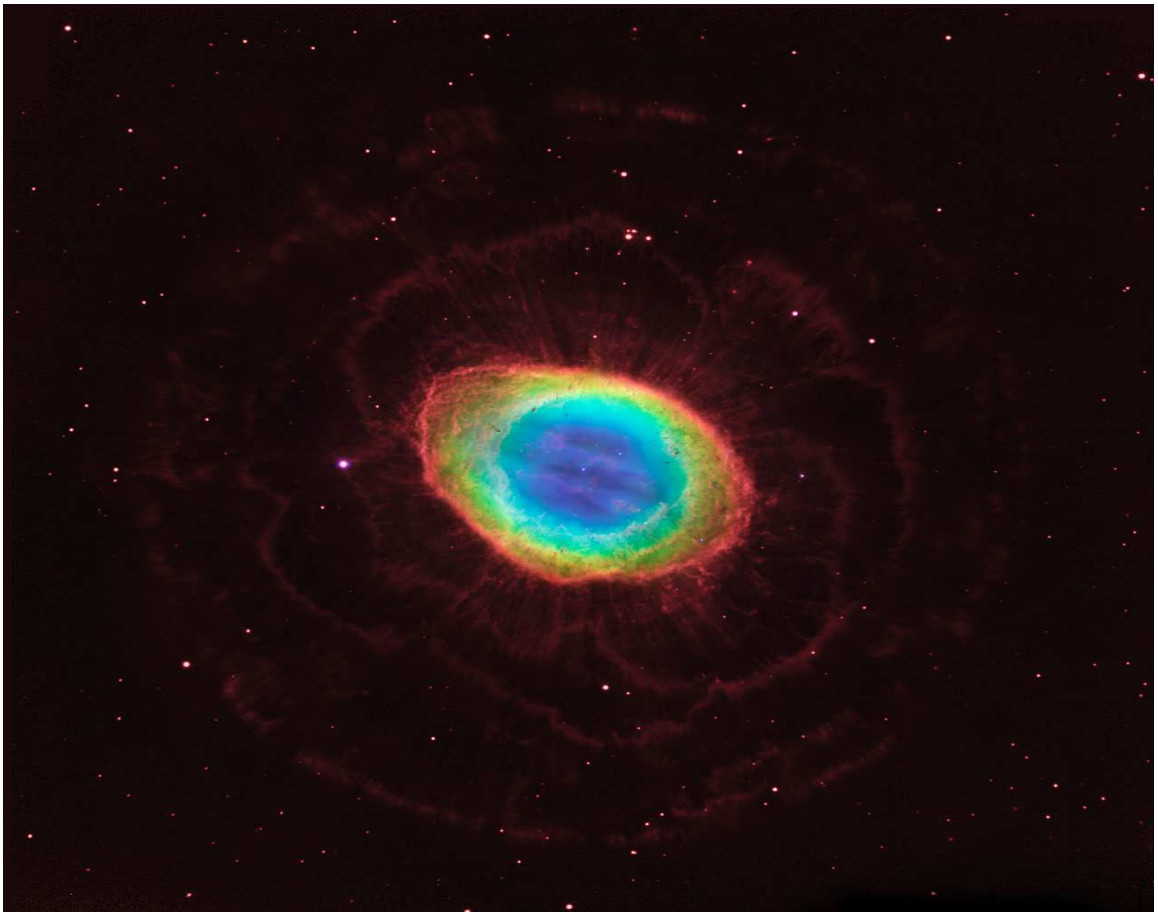

Figure 1.2 Visible and Infrared composite image of the Ring nebula, a planetary nebula in the constellation of Lyra. The observations in visible wavelengths come from NASA's Hubble Space Telescope and the ground-based Infrared observations come from the Large Binocular Telescope. Image Credit: NASA, ESA

supernovae are quite different. Consequently, they influence the chemical evolution of the ISM in different ways. Supernova nucleosynthesis models predict that type II supernovae overproduce α-capture elements such as C, O, Mg, Si, S, Ca, Ar relative to Fe, whereas type Ia supernovae mainly produce the Fe-peak elements (Cr, Mn, Fe, Co, Zn). In other words, type II supernovae are responsible for the creation of the majority of the α-capture elements and type Ia supernovae contribute significantly to the synthesis of Fe-peak nuclei. As a comparison, on average each Type Ia supernova produces $\sim 0.8 M_{\odot}$ of Fe, while a Type II supernova produces $\sim 0.1 M_{\odot}$. The observed ratio of the occurrence frequency of Type Ia to type II supernovae is ~ 0.12 (van den

Bergh & Tammann, 1991). Based on type Ia and type II supernovae yields and their relative frequencies, Nomoto et al. (1997) estimate that $\sim 50-75\%$ of ^{56}Fe is produced in Type Ia supernovae. For further discussions on nucleosynthetic yields in massive stars see, for instance, Woosley, Heger & Weaver (2002) or Nomoto et al. (2006). For Type Ia supernova yields, see Nomoto et al. (1997). In terms of the chemical enrichment timescales, a typical massive star ending its life in a supernova explosion has a lifetime of $\sim 10^7$ years, whereas stars of mass M $\lesssim 10 M_\odot$ producing type Ia explosions require on the order of $\sim 10^9$ years. Therefore, the early galactic chemical evolution is expected to be dominated by type II supernovae. Since stars born at different epochs carry information on the state of enrichment of the interstellar gas they were created from, populations of old stars should be exhibiting overabundance of α-capture elements relative to Fe. Observations of old stellar populations in the halo of the Milky Way confirm this trend indeed.

1.3 Galactic Chemical Evolution Models

Galaxies change constantly driven by internal star formation, gas exchange with the surroundings and gravitational interaction with other nearby galaxies. One of the manifestations of this change, as predicted by galaxy evolution models, is the gradual build-up of metals. As represented in Figure 1.1, the continuous cycles of star formation and death enrich the initially primordial (composed primarily of H and He) ISM with metals and this accumulation should eventually be detectable. Therefore, the state of chemical enrichment of a galaxy narrates its star formation history, which in turn, is closely related to other galaxy properties such as morphology, gas temperature and ionization. Armed with the knowledge of element production, ejection and mixing mechanisms mentioned in the previous section and information on chemical abundances, evolution in galaxies can be deciphered with the help of

galactic chemical evolution models.

1.3.1 Closed Box Model

The simplest galactic chemical evolution model assumes the galaxy to be a closed box, i.e, no gas flows into or out of the system during the entire course of its evolution. This model also assumes the initial material to be uncontaminated with metals, and that the system is homogeneous, or in other words, the gas remains well mixed. Under this assumptions, the amount of interstellar gas is steadily decreased due to star formation, and the gas left over in the ISM gets gradually enriched with metals produced in stars (Searle & Sargent, 1972). If the mass of metals in the ISM at time t is $M_m(t)$, and the mass of gas is $M_g(t)$, then the metallicity of the gas is defined as

$$Z(t) = \frac{M_m(t)}{M_g(t)}. \tag{1.4}$$

By this definition, the Sun's metallicity by mass is $Z_\odot \sim 0.02$. If the total stellar mass in the system is given by $M_s(t)$ then a burst of star formation produces a mass of new stars δM_s in time δt. These stars will form a mass of metals $p\delta M_s$, where p is the yield. However, the amount of metal already locked in these stars is given by $Z\delta M_s$ and taking this into account we get the net mass of new metals as

$$\delta M_m = p\delta M_s - Z\delta M_s = (p - Z)\delta M_s. \tag{1.5}$$

Conservation of mass in the isolated system dictates that $\delta M_s = -\delta M_g$. Therefore, from equations 1.4 and 1.5 we get,

$$\delta Z = -p\frac{\delta M_g}{M_g}, \tag{1.6}$$

which can be solved assuming the yield p to be constant, as

$$Z(t) = -p \ln \left(\frac{M_g(t)}{M_g(0)} \right). \tag{1.7}$$

The yield p can be estimated by measurements of Z and M_g and point to an average yield of $p \sim 0.01$ in the Milky Way. The mass of stars with metallicity less than Z is given by $M_s(< Z) = M_g(0) - M_g(t)$, which according to equation 1.7 is

$$M_s(< Z) = M_g(0) \left(1 - \exp(-\frac{Z}{p}) \right). \tag{1.8}$$

Taking into account the gas fraction in the Milky Way which is ∼0.1, the closed box model predicts that about half of stars in the Milky Way should be less metal rich than $0.25 Z_\odot$. However, the observed fraction of stars with such metallicities is much less at only a few percent. This points out one of the shortcomings, known as the "G-Dwarf problem", of this simplistic model that it predicts too many metal poor stars in the disk of the Milky Way than what is observed.

1.3.2 Accreting Box Model

Observations reveal that the Milky Way is accreting gas constantly from the Magellanic clouds and the inter-galactic medium. This fact contradicts the assumption of the closed box model that galaxies are isolated systems. The accreting box model takes this into account by letting the the total mass, M_{tot}, of the system vary.

$$\delta M_{tot} = \delta M_s + \delta M_g, \tag{1.9}$$

this relation leads to the evolution of metallicity $Z(t)$ as

$$\delta Z = \delta \left(\frac{M_m}{M_g} \right) = \frac{1}{M_g} \left((p - Z) \delta M_{tot} - p \delta M_g \right), \tag{1.10}$$

which upon division by δM_{tot} leads to the differential equation,

$$\frac{dZ}{dM_{tot}} = \frac{1}{M_g}\left[p(1 - \frac{dM_g}{dM_{tot}}) - Z\right]. \tag{1.11}$$

Assuming that the infall rate is equal to the rate at which the star formation is consuming the gas i.e, the total gas mass remains constant and that the initial material as well as the infalling gas are free of metals, the equation above can be integrated to

$$Z = p\left[1 - \exp\left(1 - \frac{M_t(t)}{M_g(t)}\right)\right]. \tag{1.12}$$

From equation 1.12, the mass of stars with metallicity less than Z can be derived to be

$$M_s(< Z) = -M_g \ln\left(1 - \frac{Z}{p}\right). \tag{1.13}$$

For Milky Way's gas fraction $\sim$ 10%, and $p \sim Z_\odot$ (from eq. 1.12), the accreting box model predicts the fraction of stars with metallicities lower than $0.25Z_\odot$ to be $\sim$ 3%. This matches the observations much more closely than the predictions from the closed box model.

The analytical frameworks described above employ many simplifying assumptions to model the highly complex process of chemical evolution in galaxies, and therefore, describe an approximate picture only. However, work in this field has advanced much in the recent decades with more sophisticated analytical, semi-analytical and hydrodynamical simulation models which take various star-formation, accretion and merger scenarios into account. Pei & Fall (1995) and Pei et al. (1999) present good examples of complex analytical models of cosmic chemical evolution that incorporate observational constraints. The model described in Somerville et al. (2001) and those from Argast et al. (2000) and Gibson et al. (2003) are some of the semi-analytical models in use today. For examples of hydrodynamic simulations of cosmic chemical evolution, see Cen et al. (2003); Oppenheimer et al. (2012).

As expected from the basic premise that chemical enrichment of ISM occurs due to continuous star formation cycles, all of the models predict that the metallicity of interstellar gas increases with decreasing redshift (z), starting from a low value at high z (see Appendix A for a brief discussion on redshift). The models are in close agreement with each other in predicting that the mean interstellar metallicity should reach the solar level at $z = 0$, which has been confirmed by observations of the Galaxy's ISM and the ISM of nearby galaxies. Figure 1.3 represents the models from Pei et al. (1999) and Somerville et al. (2001) as examples of the trends predicted by chemical evolution models. Different models, however, disagree in terms of the metallicities at high redshifts resulting in uncertainties in our understanding of the chemical evolution of the young Universe. Constraints derived from observations of interstellar metallicity in galaxies up to very high redshifts and over a long redshift baseline is, therefore, of crucial importance. The observations can help eliminate the less accurate models or lead to new improved ones, and help shed light on star formation, galaxy dynamics and gas flow properties of young galaxies.

1.4 Physics of Spectral Line Formation

The need for studying the ISM in galaxies for the improvement of our understanding of cosmic chemical evolution is evident. Observational data coming from beyond the Milky Way's neighborhood is especially crucial for these purposes. Radiation is emitted by interstellar gas across various wavelength bands and in different intensities based on the temperature, ionization state, density and proximity of the emitting region with other sources of energy. The emission may come in the form of recombination lines (e.g., Hα), molecular lines (e.g., CO, NH_3), or scattered radiation, and the properties of ISM can be studied with the help of imaging or emission spectra. However, due to the diffuse nature of the emission coupled with inverse square law

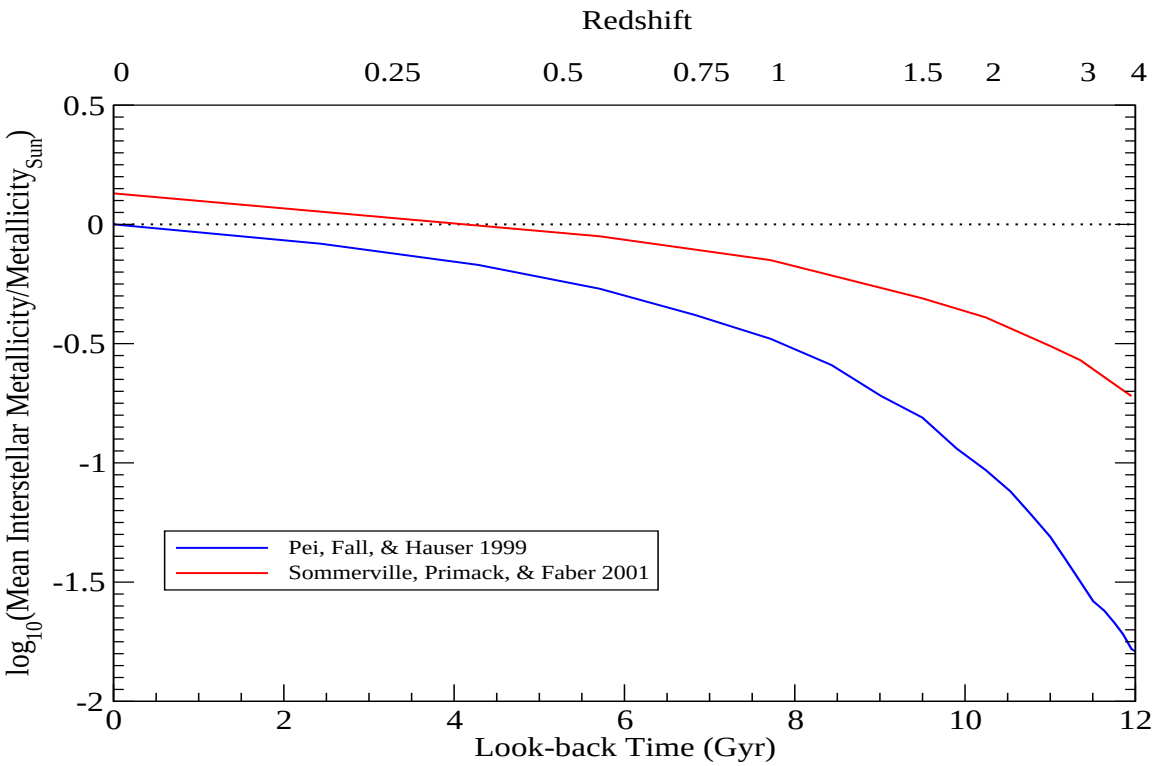

Figure 1.3 Predicted mean interstellar metallicity (relative to solar metallicity) evolution from models described in Pei et al. (1999); Somerville et al. (2001). The abscissa denotes the 'lookback time' with the corresponding redshift, z, shown at the top of the panel. In the lookback time scale, $t = 0$ denotes the present time and increasing t denotes younger Universe. The horizontal dotted line represent the solar metallicity. Note that both the models predict the mean metallicity to evolve from a low value at high redshift (young Universe) to near solar values at $z = 0$ (present time), although the predictions differ widely at high z.

and the expansion of the Universe, the study becomes gradually more difficult with increasing distance. In fact, even light from the stellar component of high redshift galaxies can be extremely difficult to detect and can be observationally expensive even with the 8-10m class telescopes. Most of the high redshift galaxies with reasonable detections have been extremely bright either because they hosted active galactic nuclei or they were star burst galaxies. But these systems can not be considered as typical representation of galaxies and therefore, flux limited studies of high redshift galaxies tend to introduce a bias towards unusual, bright, star forming systems.

An alternate way of exploring the nature of interstellar gas is through its absorp-

tion properties, i.e., through the study of its absorption signatures imprinted on light from background sources such as quasars (see Chapter 2 for details). The absorption study is independent of the brightnesses of the galaxies under consideration and is free from any bias towards bright, star forming galaxies. This section introduces the basics of the physical processes dictating the interaction of light with interstellar medium. The resulting observables are also described, with an emphasis on those relevant to absorption studies. More detailed discussions on these topics can be found in Rybicki & Lightman (1979); Spitzer (1978).

1.4.1 Radiative Transport and Optical Depth

Considering a point source of radiation, the amount of energy in a wavelength range $d\lambda$ passing in time dt through a surface element dA which subtends a solid angle dΩ at the source is given by

$$dE_\lambda = I_\lambda \cos\theta dA\, d\Omega\, d\lambda\, dt, \tag{1.14}$$

where θ is the angle between a ray of light and the normal to the surface, and I_λ is defined as the specific intensity. If the medium through which the radiation is traveling adds photons from other sources to the beam, then the amount of energy added in a volume element dV is given by

$$dE_\lambda = j_\lambda\, dV\, d\lambda\, dt\, d\Omega = j_\lambda\, dA\, ds\, d\Omega\, d\lambda\, dt, \tag{1.15}$$

where j_λ is the emissivity of the medium and ds is the path along the beam within dV. The contribution of dV to the beam intensity is given by

$$dI_\lambda = j_\lambda ds. \tag{1.16}$$

Now, if the medium is also responsible for absorption of photons from the beam, the resulting reduction in the beam intensity is

$$dI_\lambda = n(s)\sigma_\lambda I_\lambda ds \equiv \alpha_\lambda I_\lambda ds, \tag{1.17}$$

where n is the number density of absorbing particles, σ is the absorption cross section, and α_λ is called the attenuation coefficient. Taking both emission and absorption into account, the transfer equation i.e., the differential equation describing the change in beam intensity along the path length ds can be written as

$$\frac{dI_\lambda}{ds} = j_\lambda - \alpha_\lambda I_\lambda, \tag{1.18}$$

or, by rearranging,

$$\frac{dI_\lambda}{ds\,\alpha_\lambda} = \frac{j_\lambda}{\alpha_\lambda} - I_\lambda. \tag{1.19}$$

By defining the 'optical depth' (τ_λ) and the 'source function' (S_λ) of the medium as

$$\tau_\lambda = \int \alpha_\lambda \, ds = \int n(s)\sigma_\lambda \, ds, \tag{1.20}$$

and

$$S_\lambda \equiv \frac{j_\lambda}{\alpha_\lambda}, \tag{1.21}$$

the transfer equation can be re-written in a simpler form

$$\frac{dI_\lambda}{d\tau_\lambda} = S_\lambda - I_\lambda. \tag{1.22}$$

Assuming the source function to be constant along the beam, equation 1.22 can be integrated to obtain the intensity as a function of the optical depth

$$I_\lambda(\tau_\lambda) = I_\lambda(0)e^{-\tau_\lambda} + S_\lambda(1 - e^{-\tau_\lambda}), \tag{1.23}$$

where $I_\lambda(0)$ is the intensity of the beam incident on the medium. If the medium is responsible for only absorption, the source term vanishes and equation 1.23 can be re-written as

$$I_\lambda(\tau_\lambda) = I_\lambda(0)e^{-\tau_\lambda}. \tag{1.24}$$

Equation 1.24 describes the variation of intensity with wavelength in a beam of light passing through an absorbing medium. When applied to the scenario of absorption from intervening material along a line-of site towards a bright background source, this equation essentially describes an absorption spectrum. The quantity $I_\lambda(0)$ represents the unaffected spectrum of the background source and I_λ represents absorption signatures imprinted on the background spectrum by intervening gas which can be characterized by τ_λ. The optical depth is one of the most fundamental observables derived from the study of absorption lines present in the spectra of background sources and as seen from equation 1.20, reveal important properties of the absorbing gas.

In most astrophysical observations and especially for absorption along a line-of-sight, the true densities $n(s)$ are difficult or impossible to determine. However, quantitative information on absorbing particles can be obtained in terms of 'column density', defined as

$$N \equiv \int n(s)\, ds. \tag{1.25}$$

The column density is the number of absorbing particles (e.g., neutral atoms, ions or molecules) along the line of sight in a pencil beam of 1 cm^2 cross-section. The optical depth, using equations 1.20 and 1.25 can be written as

$$\tau_\lambda = N\sigma_\lambda. \tag{1.26}$$

From measurements on the absorption lines produced by different molecules or elements in various ionization stages, their column densities can be determined, which

in turn, reveal information on chemical composition, ionization, and other physical properties of the absorbing gas.

1.4.2 Equivalent Width

Another observable of fundamental importance derived from of an absorption line is the equivalent width, W, defined as

$$W \equiv \int_0^\infty \frac{I_c - I_\lambda}{I_c} d\lambda = \int_0^\infty (1 - e^{-\tau_\lambda}) d\lambda, \tag{1.27}$$

where I_λ is the intensity within the absorption line while I_c stands for the intensity of the continuum, i.e, the intensity of the region in background spectrum around the absorption line but unaffected by any absorption. For a continuum normalized spectrum, $I_c = 1$, and the equivalent width can be thought of as the width of a rectangular box with unit height and having the same area as that enclosed by the spectral line. Figure 1.4 describes this concept.

Due to the Hubble expansion, the observed equivalent width (W_{obs}) of an absorption line from a cloud at redshift $z_{abs}$is stretched by a factor $(1 + z_{abs})$ compared to the equivalent width at the rest frame (W_{rest}) of the absorber. Therefore,

$$W_{obs} = W_{rest}(1 + z_{abs}). \tag{1.28}$$

1.4.3 Line Broadening Processes

The form of the intervening material's optical depth modifying the radiation from the background source is governed by the physical and chemical properties of the absorbing gas. Most of the absorption features important for ISM-studies originate from bound-bound atomic transitions. Although the absorption profiles produced by these transitions are expected to be extremely sharp and well-defined, in reality

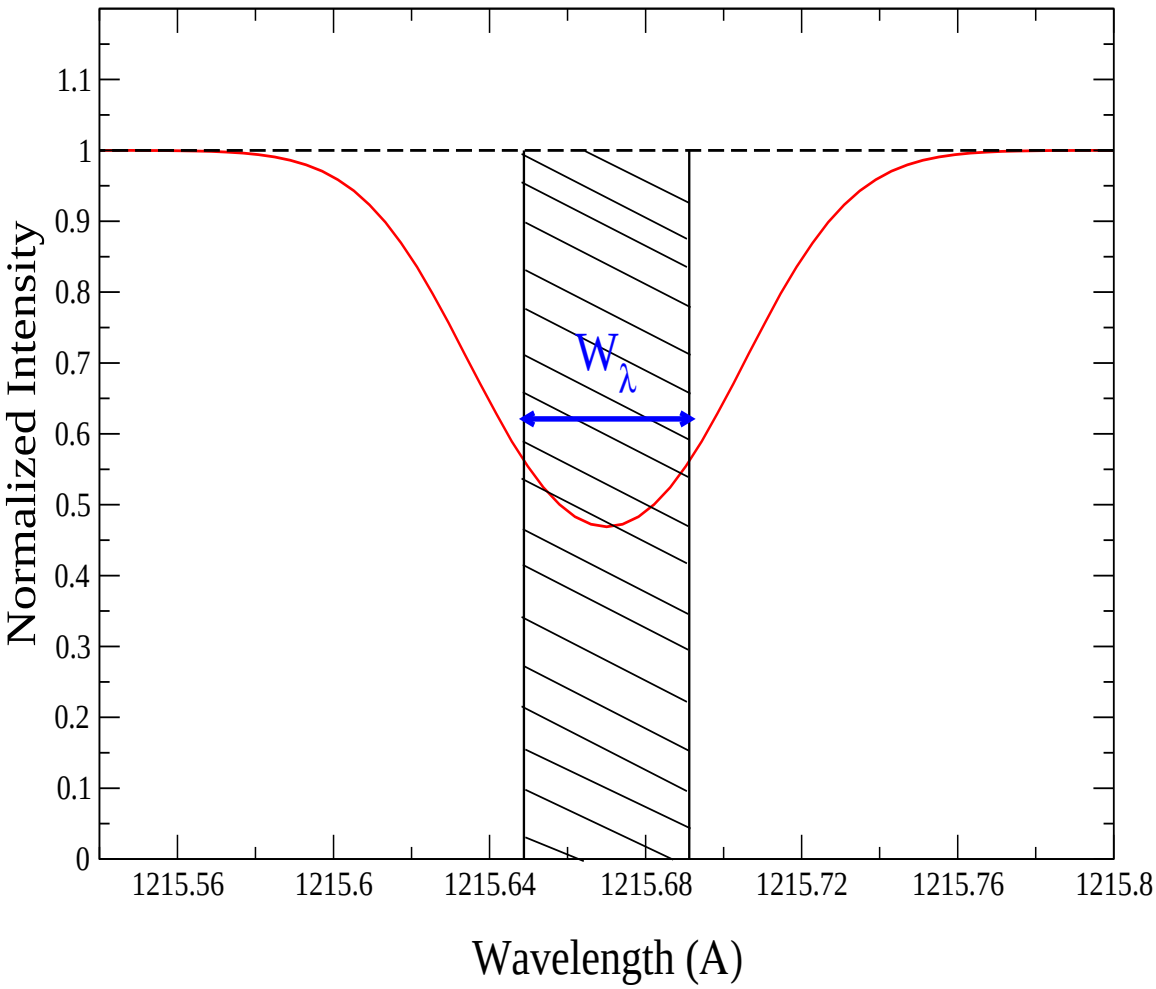

Figure 1.4 The equivalent width of an absorption line. The horizontal dashed line represents the normalized continuum level at $I = 1$. The absorption line is represented with the solid red curve. The area under the line profile is same with the area of the rectangular shaded region of unit height. The width of this rectangle is defined as the equivalent width of the absorption line.

they are observed to be much more complex. The width and shape of a spectral line are governed by several factors such as the column density of the absorbing ion, temperature, turbulence and bulk motion in the gas. The interstellar gas belonging to a galaxy at a certain redshift is usually composed of several sub-structures moving with respect to each other with different relative velocities. Therefore, while a spectral line originating form one particular substructure is broadened due to various underlying physical processes, multiple lines produced by the different velocity

components superpose to result in a complex absorption feature.

There are several mechanism responsible for spectral line broadening but the two main processes at work in a typical ISM environment are the natural or quantum mechanical broadening and the thermal or Doppler broadening. Another common type of broadening, resulting from collisions between atoms, is usually unimportant in interstellar medium owing to its low density. This section provides brief discussions on natural and thermal broadening mechanisms. More detailed descriptions on different broadening processes, including quantum mechanical and thermal broadening, can be found in Mihalas (1970); Thorne et al. (1999).

- **Natural Broadening** The photons in a beam traveling through a medium interact with the material depending on their own energies as well as the energy structure of the atoms in the medium. An atom with energy levels E_u and E_l (where $E_u > E_l$), upon interacting with a photon of energy $h\nu_0 = E_u - E_l$, can absorb the photon to make a transition to the excited state. The atom stays in the unstable excited state for a short time (typically $\sim 10^{-8}s$ for dipole transitions) before spontaneously emitting a photon of the same energy ($h\nu_0$) and returning to the lower energy state. Unlike the incident photon traveling along the beam direction, the spontaneous emission has an isotropic probability distribution, i.e., the photon can be emitted at any random direction. This essentially removes a photon with frequency ν_0 from the sight line. The cumulative effect produced by a collection of such atoms in the medium will result in an absorption line in the spectrum of the background source at $\nu = \nu_0$. However, the line is expected to be have the profile of a delta-function, i.e, to be infinitely sharp. However, the observed lines have finite widths and one of the reasons behind this is the quantum mechanical broadening. The fact that the atom takes a finite amount of time for de-excitation suggests, obeying the uncertainty relation $\Delta E \Delta t \sim \hbar$, that the energy difference between its two states

has a spread around the value given by $E_{ul} = E_u - E_l$. This spread in energy ΔE translates into the finite width of the absorption line. From the classical treatment of an atomic transition as a damped oscillator, we can arrive at the equation for absorption cross section, σ_ν, as

$$\sigma_\nu = \left(\frac{\pi e^2}{m_e c}\right) \phi(\nu) = \left(\frac{\pi e^2}{m_e c}\right) \frac{\gamma/4\pi^2}{(\nu - \nu_0)^2 + (\gamma/4\pi)^2}, \tag{1.29}$$

where γ is the oscillator damping constant. The absorption cross section describes the profile of the spectral line centered at ν_0. Equation 1.29 represents a Lorentzian profile with full width at half maximum of $FWHM = \gamma/2\pi$. Complete quantum mechanical treatment yields the same cross section with a multiplication factor called the oscillator strength f, which describes the probability of the transition in question. The oscillator strength can be expressed as

$$g_l f_{ul} = g_u a_{ul} \frac{m_e c \lambda^2}{8\pi^2 e^2}, \tag{1.30}$$

where λ is in Å, g_u and g_l are the statistical weights of the upper and lower energy levels, respectively and a_{ul} is the transition probability. The absorption cross section, including the oscillator strength is given as

$$\sigma_\nu = \left(\frac{\pi e^2}{m_e c}\right) f_{ul} \phi(\nu). \tag{1.31}$$

The oscillator strength assumes different values for different bound-bound transitions but typically $f \lesssim 1$. Only for for a few very strong transitions $f > 1$. The oscillator strengths corresponding to various transitions in H atom can be calculated analytically and f-values for other atomic transitions can be determined from laboratory measurements of transition lifetimes. The oscillator

strength can be also be thought of as the effective number of classical oscillators (Shu, 1991). In terms of wavelength λ, the absorption cross section can be written as

$$\sigma_\lambda = \sigma_0 \phi_\lambda, \tag{1.32}$$

where σ_0 in the equation above is given by

$$\sigma_0 = \frac{\lambda^4}{8\pi c} \frac{g_u}{g_l} a_{ul}, \tag{1.33}$$

where the broadening function, ϕ_λ, is given as

$$\phi_\lambda = \frac{1}{\pi} \frac{\gamma}{\gamma^2 + (\lambda - \lambda_0^2)}, \tag{1.34}$$

and the radiation damping constant is given by

$$\gamma = \frac{\lambda^2}{4\pi c} \sum_{E_r < E_u} a_{ur}. \tag{1.35}$$

The FWHM of a naturally broadened profile is, in wavelength units, $FWHM = \lambda^2\gamma/2\pi c$, which is typically very small for most transitions in the Ultraviolet and Optical bands.

- **Doppler Broadening** While the absorption cross section, described in equation 1.31, explains the natural broadening of a line around the central wavelength ν_0, individual motion of an atom can shift the central wavelength in accordance with the Doppler effect. Atoms moving with different relative velocities in the gas produce a 'smeared' absorption line or in other words, contribute to the broadening of the line. Aside from bulk motion, thermal velocity dominates the movement of particles in interstellar gas. Collisions in the gas thermalize the medium and produce a Maxwellian velocity distribution in a short

amount of time (Spitzer, 1978). According to the relativistic description of the Doppler effect, the difference between observed and rest-frame wavelengths is is dependent on the velocity as

$$\lambda_{obs} = \lambda_{rest}\sqrt{\frac{1+\frac{v}{c}}{1-\frac{v}{c}}}. \tag{1.36}$$

At temperatures typical for interstellar gas, we can assume $v/c << 1$, and equation 1.36 reduces to

$$\lambda_{obs} = \lambda_{rest}(1 \pm \frac{v_x}{c}), \tag{1.37}$$

where the radial component of the velocity is taken to be in the x direction. From the Maxwellian velocity distribution we get the number of particles with velocities between v and $v + dv$ as

$$N(v)dv = \frac{N_0}{\sqrt{\pi}b}\exp(-v_x^2/b^2)dv, \tag{1.38}$$

where N_0 is the total number of particles in the cloud and b (also called the 'Doppler b-parameter') is the most probable speed, defined as

$$b = b_{th} = \sqrt{\frac{2kT}{m}}. \tag{1.39}$$

Using equation 1.37 with the Maxwell-Boltzmann distribution of velocities, we get the fraction of atoms absorbing radiation between the wavelengths λ and $\lambda + d\lambda$,

$$\psi(\lambda)d\lambda \equiv \frac{N(\lambda)d\lambda}{N_0} = \frac{1}{\sqrt{\pi}\Delta\lambda_D}\exp\left(-\frac{(\lambda-\lambda_{rest})^2}{\Delta\lambda_D^2}\right)d\lambda, \tag{1.40}$$

where the the Doppler width, $\Delta\lambda_D$ is defined as

$$\Delta\lambda_D = \frac{\lambda_{rest} b_{th}}{c}. \tag{1.41}$$

Equation 1.40 represents a Gaussian profile with full width at half max of $FWHM = 2\sqrt{\ln 2}\Delta\lambda_D$. With numerical solutions to equation 1.41, we obtain $FWHM \sim 0.22\sqrt{T/A}$ km s^{-1}, where T is the temperature in Kelvin and A is the atomic mass number.

Besides thermal motions, the interstellar gas undergoes bulk motions, in which the entire cloud or large sub-structures in it move with respect to the observer reference frame. In addition, there are smaller scale turbulent motions within the cloud which also contribute to the broadening of spectral line. This type of broadening can be accounted for by adding a term to the Doppler parameter and by defining an 'effective Doppler parameter'

$$b_{eff}^2 = b_{th}^2 + b_{turb}^2. \tag{1.42}$$

Ideally, it is possible to separate the turbulent and thermal motions from observed spectra to determine the kinetic temperature of the gas. Due to the mass dependence of the Doppler parameter, different atomic species in a certain absorber have different thermal broadening of their absorption features while the effect of turbulence will be the same. If observations of two lines of species (e.g., Si and Fe) with very different masses exist for an absorbing cloud, one can estimate the temperature by measuring the FWHM of the lines independently and by eliminating b_{turb}. The temperature can be obtained as

$$T = \frac{m_{Si} m_{Fe} (b_{Si}^2 - b_{Fe}^2)}{(m_{Fe} - m_{Si}) 2k}. \tag{1.43}$$

However, high resolution and high S/N spectra are needed for accurate parameter estimates to achieve this goal (see for instance Jenkins et al. (2005)). Even

with high resolution spectra blending of individual lines can lead to artificially high Doppler parameters and hence temperatures.

1.4.4 The Voigt Profile

Natural and thermal broadening are independent processes. Therefore, the combined broadening produced by these mechanisms can be represented by a function, also called the Voigt function, which is the convolution of the natural and Doppler broadening functions:

$$\phi_\lambda(Voigt) = \phi_\lambda(Natural) \otimes \psi_\lambda(Doppler). \tag{1.44}$$

Qualitatively, this can be viewed as the superposition of the natural line profiles produced by the fractional number of particles absorbing radiation between λ and $\lambda + d\lambda$, over all wavelengths. Using equations 1.34 and 1.40 we get,

$$\phi_\lambda(Voigt) = \frac{1}{\pi^{3/2}\,\Delta\lambda_D} \int_{-\infty}^{\infty} \frac{\gamma}{\gamma^2 + (\lambda - \lambda')^2} \exp\left[-\frac{(\lambda - \lambda')^2}{\Delta\lambda_D^2}\right] d\lambda'. \tag{1.45}$$

The absorption cross section can be written in terms of the Voigt function as

$$\sigma_\lambda = \sigma_0 \phi_\lambda(Voigt), \tag{1.46}$$

and, using equations 1.24 and 1.26, the absorption line profile can be written in terms of the column density of the absorbing species as

$$I_\lambda = I_0 e^{-N\sigma_0\phi_\lambda(Voigt)}. \tag{1.47}$$

Comparing equations 1.34 and 1.40 we find that the probability that an atom will absorb $\Delta\lambda$ away from λ_0 ($\Delta\lambda = |\lambda - \lambda_0|$) decreases as the inverse square of $\Delta\lambda$ for natural broadening and exponentially in the case of Doppler broadening. Therefore,

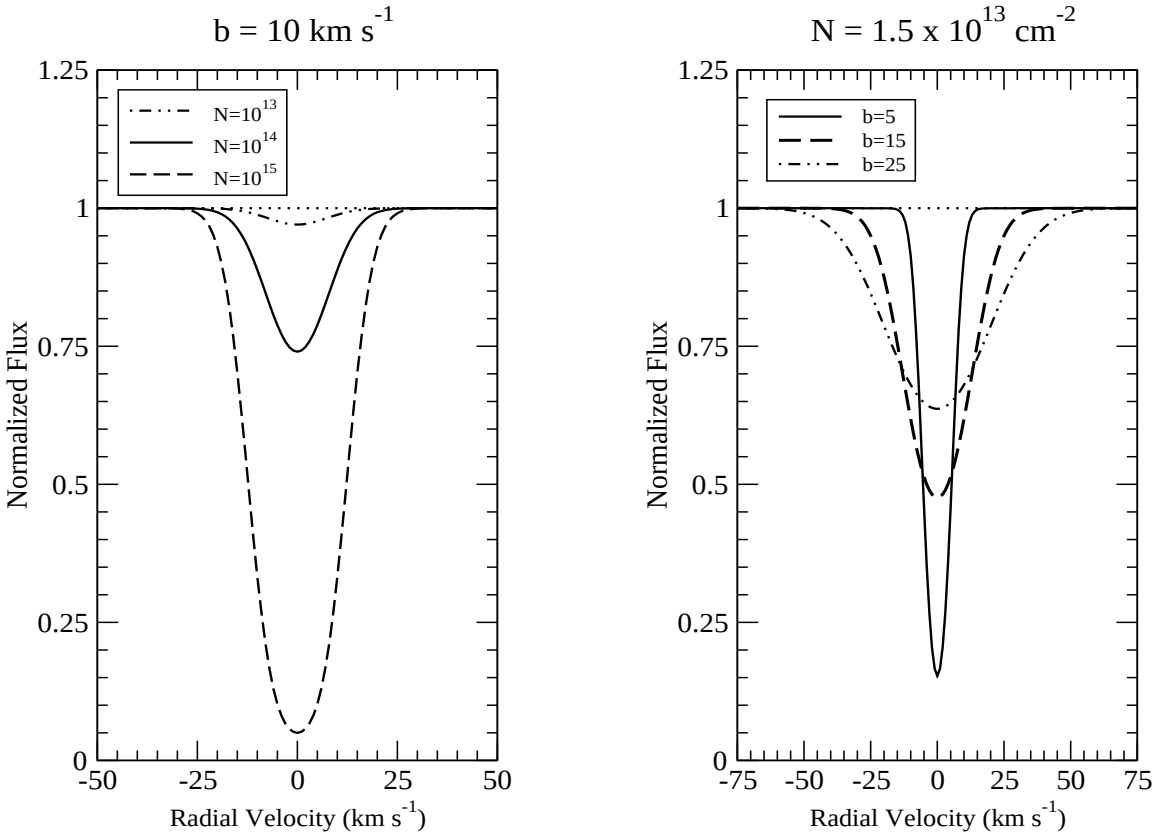

Figure 1.5 Left panel: Theoretical Voigt profiles for the S II 1259.5 Å transition with $b = 10$ km s^{-1} and column densities of $10^{13} cm^{-2}$, $10^{14} cm^{-2}$, and $10^{15} cm^{-2}$. Right panel: Theoretical Voigt profiles for the Lyman-α line of Hydrogen with $N = 1.5 \times 10^{13} cm^{-2}$ and b-parameters of 5, 15 and 25 km s^{-1}. The horizontal dotted line in both panels represents the normalized continuum level.

equating 1.34 and 1.40 it can be seen that at $\Delta\lambda \times (\frac{c}{\lambda}) \simeq 3b$ the probabilities of absorption due to these broadening processes are comparable (for the values of a_{ul} corresponding to commonly seen interstellar absorption lines). Therefore, the absorption in a Voigt profile is dominated by motion in the gas for $\Delta\lambda < \frac{3b\lambda}{c}$, while for $\Delta\lambda > \frac{3b\lambda}{c}$, the absorption is primarily due to natural damping. Figure 1.5 depicts the Voigt profiles of several absorption lines for different N (with a fixed b-parameter) and b-parameter (with a fixed N) values.

In addition to broadening processes mentioned above, the instrument used for observations contributes to the blurring of absorption lines through imperfections in the optics, diffraction gratings and detectors. As a result, the observed spectral

profile is the convolution of the theoretical Voigt profile and the blurring profile of the instrument, also called the instrument spread function (ISF). The following equation describes the process:

$$I_{obs}(\lambda) = \left[I_0(\lambda)e^{-\tau_\lambda}\right] \otimes \phi_{ISF}(\lambda), \tag{1.48}$$

or from equation 1.46,

$$I_{obs}(\lambda) = \left[I_0(\lambda)e^{-N\sigma_0\phi_\lambda(Voigt)}\right] \otimes \phi_{ISF}(\lambda). \tag{1.49}$$

The ISF can be determined from observations of emission lines from gas discharge lamps in the laboratory. Since these emission lines have extremely small natural widths which can be calculated using equation 1.31, the observed line profiles can be used to determine the ISF. Typically, the instrumental spread function can be approximated as a Gaussian. With the knowledge of the ISF, column densities of various ions can be extracted from their absorption line profiles by Voigt profile fitting via χ^2 minimization routines.

1.4.5 The Curve of Growth

The curve of growth (COG) describes how the equivalent width, W_λ, of a line grows with increasing column density of the absorbing atoms, and therefore, can be used to derive the column density from the observed W_λ. For an absorption line, the functional dependence of W_λ on N is determined by the optical depth at the line core, τ_0. The COG can be divided into three distinct regions depending on the value of τ_0 and N:

- **Linear Part** This part of the COG can be seen when the line is optically thin, i.e., for $\tau_0 << 1$. This regime allows us to the use the approximation $e^{-x} \simeq 1-x$ and from equations 1.26,1.27 and 1.46 we get,

$$W_\lambda = N\sigma_0 \int_{-\infty}^{\infty} \phi_\lambda d\lambda = N\sigma_0, \tag{1.50}$$

since, ϕ_λ represents a probability distribution and $\int_{-\infty}^{\infty} \phi_\lambda d\lambda = 1$. Upon using the numerical values for σ_0, we get.

$$N = 1.13 \times 10^{20} . \frac{W_\lambda}{\lambda^2 f}\, cm^{-2}. \tag{1.51}$$

In this region, $W_\lambda \propto N$, and the relation is independent of b. On this linear regime, W_λ provides accurate determination of N.

- **Logarithmic Part** The residual intensity at the line core decreases (depth of the line increases) with increasing τ_0. This process continues until all of the photons at the line core are absorbed from the beam of light. With further increase in τ_0 (i.e., with increasing N), the number of additional photons removed from the beam is very little, or in other words, W_λ increases very little with increasing N, and the line becomes 'saturated'. On this part of the COG, for $10 \lesssim \tau_0 \lesssim 10^3$, $W_\lambda \propto b\sqrt{ln(N/b)}$ and the growth function becomes sensitive to the Doppler b-parameter. In this regime, W_λ is not an accurate measure of N.

- **Damped Part** With further increase in τ_0 beyond the logarithmic part, the optical depth values become significant at wavelengths far from the line center, where absorption is dominated by the natural damping. As a result, the line profile exhibits 'damping wings' (where $\sigma_\lambda \propto \Delta\lambda^{-2}$) and the equivalent width starts to increase again as $W_\lambda = 2(N\sigma_0\gamma)^{1/2}$ Å. In this regime ($\tau_0 \gtrsim 10^4$), the growth of equivalent width is independent of the b-parameter and allows accurate determination of column density.

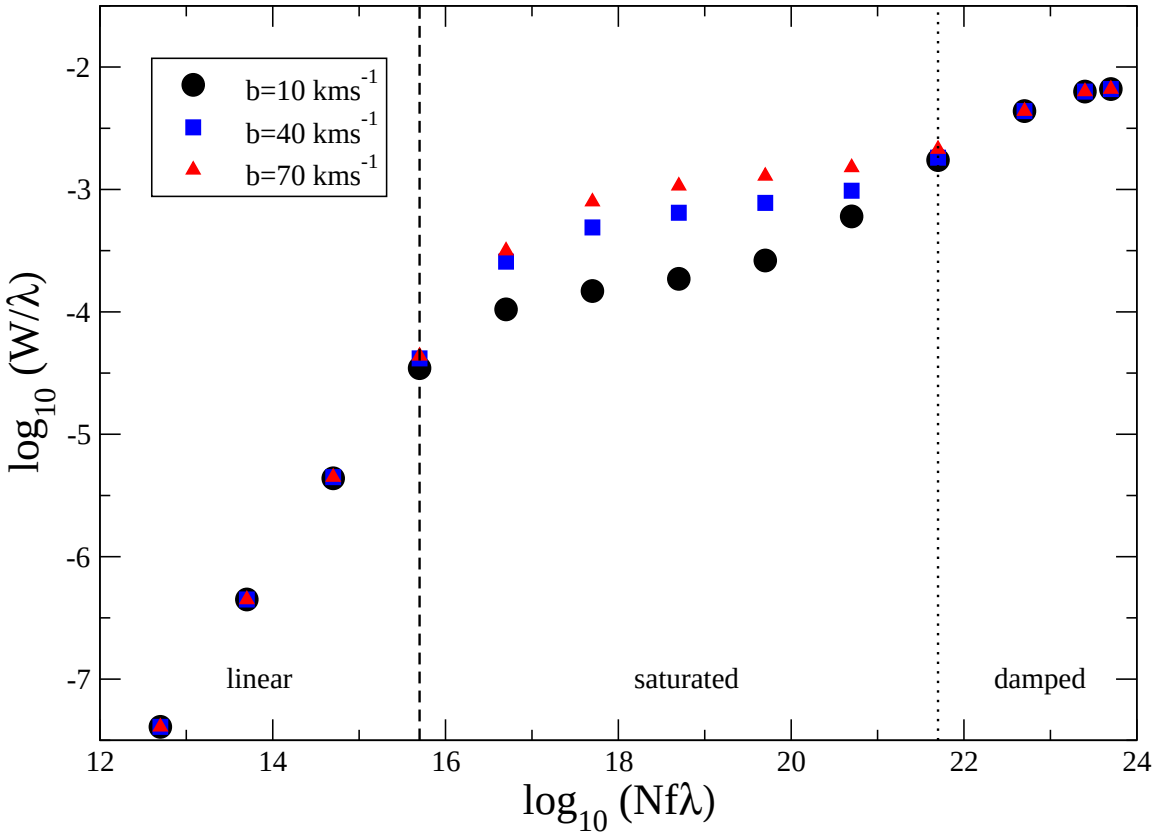

Figure 1.6 The growth function of the equivalent width with respect to the column density for the Lyman-α line of Hydrogen corresponding to b-parameters of 10, 40 and 70 km s^{-1}. It can be noted that the equivalent width is independent of the b-parameter in the linear and the damped regions. The threshold between the logarithmic and the damped regions corresponds to $N_{HI} \sim 10^{19}$.

Figure 1.6 represents the curves of growth for the H I Lyman-α line corresponding to various Doppler b-parameters. The figure suggests that the damped region in the COG of Lyman-α corresponds to $N_{HI} \gtrsim 10^{19}$.

1.4.6 The Apparent Optical Depth

In addition to the method described in Sections 1.4.4 and 1.4.5, column densities can be derived from the 'Apparent Optical Depth' (AOD) measured from the observed line profiles (Savage & Sembach, 1991). The spectral continuum of the background sources used in absorption line studies usually vary slowly with wavelength and we can assume

the continuum level to be nearly constant over the extent of the absorption line, provided the line width is small. With this assumption, we can re-write equation 1.48 as

$$I_{obs}(\lambda) = I_0(\lambda) \left[e^{-\tau_\lambda} \otimes \phi_{ISF}(\lambda) \right]. \tag{1.52}$$

The AOD, or the instrumentally blurred version of the true optical depth can be obtained, using equation 1.52, as

$$\tau_a(\lambda) = \ln[I_0(\lambda)/I_{obs}(\lambda)] = \ln[1/(e^{-\tau_\lambda} \otimes \phi_{ISF}(\lambda)]. \tag{1.53}$$

For well resolved lines, FWHM(ϕ_{ISF}) << FWHM(line), and the apparent optical depth $\tau_a(\lambda)$ is a good approximation of the true optical depth, τ_λ. The AOD can, therefore, be described in terms of column density as

$$\tau_a(\lambda) = \frac{\pi e^2}{m_e c^2} f \lambda^2 N(\lambda), \tag{1.54}$$

where $N(\lambda)d\lambda$ is the column density responsible for absorption between λ and $\lambda + d\lambda$ and the total column density is given by $N = \int N(\lambda)d\lambda$. In terms of the radial velocity, the relation takes the form

$$\tau_a(v) = 2.654 \times 10^{-15} f \lambda N(v), \tag{1.55}$$

when the wavelength λ is given in Å. The total column density is given by

$$N = \int N(v)dv = \frac{3.768 \times 10^{14}}{f\lambda} \int \ln\left(\frac{I_0(v)}{I(v)}\right) dv. \tag{1.56}$$

The AOD method works accurately when the line is resolved in a high S/N spectrum and for weak features. However, even for moderately strong lines in moderate resolution spectra, the AOD method has been demonstrated to determine column densities accurate to $\lesssim 10\%$ (Savage & Sembach, 1996).

1.4.7 Abundances of Elements

The column densities of various elements derived from absorption lines can be used to calculate abundances in the absorbing gas. If N_X and N_Y are the column densities of elements X and Y respectively, then the abundance of X relative to Y is given by

$$[X/Y] = log(N_X/N_Y) - log(X/Y)_\odot, \tag{1.57}$$

where log $(X/Y)_\odot$ is the solar system abundance ratio between X and Y. The absolute abundance of an element X is defined as its abundance relative to Hydrogen in the absorber and is given by

$$[X/H] = log(N_X/N_H) - log(X/H)_\odot. \tag{1.58}$$

The solar system abundances are determined from measurements of Sun's photosphere and the composition of meteorites. There are many compilations of the solar system abundances in the literature which vary only slightly from each other. The abundance data adopted for this work come from Asplund et al. (2009). The solar abundances of various elements commonly observed in the ISM are given in Table B.1 and a plot of the adopted solar abundance pattern is shown in Figure 1.7.

With a knowledge of the physical processes and measurement techniques described above, absorption lines from interstellar gas prove to be a powerful tool to study the state of chemical enrichment in galaxies at various epochs. This technique is extensively used in the study of the absorption line systems seen in the spectra of background quasars. Chapter 2 provides an introduction to the quasar absorption line systems.

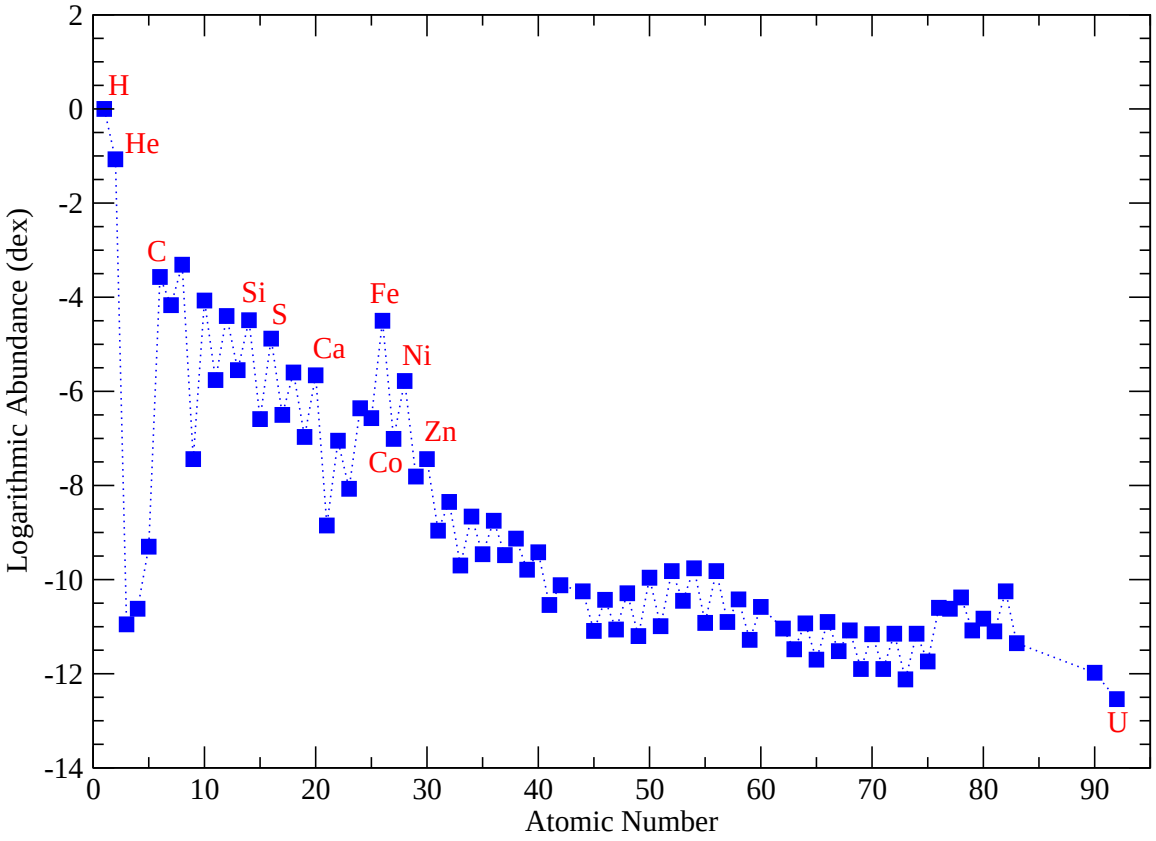

Figure 1.7 Solar system abundances of various elements relative to Hydrogen. The abundance data are from Asplund et al. (2009).

CHAPTER 2

Quasar Absorption Line Systems

As seen from Chapter 1, study of absorption lines in the spectra of bright background sources is a powerful way to learn about interstellar gas in galaxies at high redshifts. Absorption line systems in the spectra of quasars have been used most extensively to this purpose and the current chapter provides a description of these absorption systems.

2.1 Quasi-Stellar Object (QSO)

At the time of their discovery, these objects appeared as star like objects in their images but showed very different colors (spectral energy distributions) from stars. They were also found to be of extra-Galactic origins and at large distances. The estimated intrinsic (distance-corrected) luminosities of these objects were far too high for them to be stellar sources. Hence the name quasi-stellar objects (or quasars) was ascribed to them. The quasars typically are many times more luminous than the entire Milky Way ($\sim 10^{46}$ ergs s^{-1}). The size of the emitting region in these sources can be estimated from the variation time scales in their flux and the observed variations, typically of the order of weeks, suggest sub-parsec scale emitting regions. The enormous energy output from such small regions and the presence of broad

emission lines in the spectra indicate relativistic processes responsible for the energy production in quasars and the presently accepted notion puts accreting super-massive black holes ($M_{BH} \sim 10^6 - 10^9 M_\odot$) as the central engines driving these sources. The continuum of a typical quasar can be fit, in parts of the electromagnetic spectrum, by power law functions of the form $F_\nu \propto \nu^\alpha$. Using a large sample of HST spectra, Zheng et al. (1997) showed that the average quasar continuum obeys the power law with an index $\alpha \sim -1$. Synchrotron radiation is thought to be responsible for the non-thermal continuum of quasars. Quasar spectra also show broad emission lines. Another important property of the spectral energy distribution of quasars is that they produce an enormous amount of radiation at short wavelengths, or in other words, the rest-frame quasar spectra have an abundance of high energy photons. This is responsible for their intrinsic blue colors.

Quasars are among the farthest sources known to us and the most distant quasar detected till date is at $z = 7.1$ (Momjian et al., 2014). Consequently, quasars have extensively been used to study the Universe at the largest scales. A number of large scale surveys have discovered more than 200,000 quasars so far, the majority of them come from the Sloan Digital Sky Survey (York et al., 2000). Quasars, due to their high luminosity and large redshift baseline, are ideal as background sources for absorption line studies. The intrinsic blue colors of high redshifts quasars, considering the expansion of the Universe, are suitable for ground based observations in visual wavelengths. The high abundance of low wavelength photons in quasar emission provide high flux density in the UV-Blue wavelength range at the rest-frame of intervening absorbers. The most important transitions for absorption line studies take place in this wavelength range. In addition, the predictable and slowly varying continuum along with the broad emission lines in quasar spectra make the measurements of absorption lines less complicated than, for instance, in the case of background galaxy spectra.

2.2 Lyman-α Absorption Lines In Quasar Spectra

A quasar sight line may interact with intervening gas of various densities and temperatures at various locations such as the intergalactic medium, circum galactic medium and ISM in galaxies. The spectrum of the quasar shows the absorption signatures from various elements in these absorption systems. Figure 2.1 provides an illustration of this process. A schematic representation of the line of sight towards a quasar and the observed spectrum are shown in the figure. The broad peak in the spectrum represents Hydrogen emission from the quasar and the strong Hydrogen absorption line at $\sim$ 4700 Å is produced by an intervening galaxy. The narrow absorption signatures to the right of the H-emission peak represent metal absorption from the galaxy. Numerous other Hydrogen absorption features of various strengths can be seen to the left of the peak, representing various other absorbers along the same line of sight. Hydrogen (the most abundant element in the Universe) lines are most common among the different absorption features seen in quasar spectra. As most of the neutral Hydrogen atoms present in gas clouds inhabit the ground state, Lyman-series transitions dominate the features produced by neutral Hydrogen. The Lyman-α transition ($n = 1 \rightarrow 2$) at 1215.6701 Å is the strongest member of this series and can be detected abundantly in quasar spectra. The different absorption systems detected in quasar spectra can broadly be classified into four categories (see Table 2.1) based on their neutral Hydrogen column densities derived from the Lyman-α lines.

The quasar absorption line systems at the low-end of the N_{HI} scale constitute the Lyman-α forest. The weak absorption features produced by these systems are ubiquitously seen blueward of the Lyman-α emission peak in the spectra of distant quasars. The rate of incidence of these absorbers is much higher than that expected of intervening galaxies and they exhibit weak clustering properties. As a result, these absorbers are thought to be separate from galaxies and they are identified with

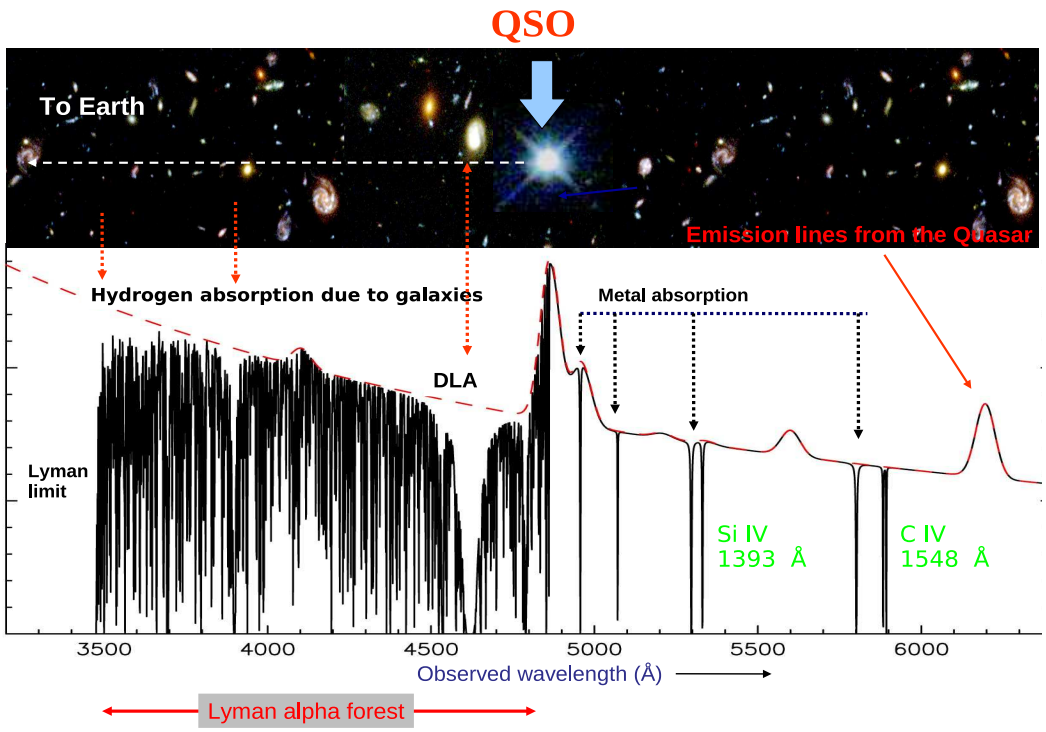

Figure 2.1 A schematic representation of the quasar absorption line technique. This illustrates the absorption by material along the line of sight to a quasar and the resulting lines imprinted on the quasar spectra. This representation is created from a version produced by John Webb and published in Pettini (2004).

intergalactic gas clouds. These absorbers are seen to consist hot and highly ionized gas, with $T \sim 4 \times 10^4$ K and $n_{HI}/n_H \sim 10^{-4}$. Although these clouds are extremely diffuse, their high rate of incidence implies that they contain the majority of the baryons in the Universe while most of the neutral gas is thought to reside in higher

Table 2.1 The classification, based on N_{HI}, of absorption systems seen in quasar spectra.

Column Density	Classification
log N_{HI} <17.2	Lyman-α forest
17.2 $\lesssim$ log N_{HI} $\lesssim$ 19.0	Lyman Limit System (LLS)
19.0 $\lesssim$ log N_{HI} $\lesssim$ 20.3	sub-Damped Lyman-α (sub-DLA)
log N_{HI} >20.3	Damped Lyman-α (DLA)

column density absorbers (Petitjean et al., 1993). Because of their high population and large redshift baseline, the Lyman-α forest clouds provide crucial constraints for simulations of structure formation in the Universe and several smoothed particle hydrodynamic (SPH) simulations (Cen et al., 1994; Zhang et al., 1998; Springel et al., 2004) have been successful in reproducing the observed properties of Lyman-α forest. The observed redshift evolution of the number of Lyman-α forest lines $\mathcal{N}$ obeys a broken power law of the form

$$\frac{d\mathcal{N}}{dz} = \left(\frac{d\mathcal{N}}{dz}\right)_0 (1+z)^{\gamma}, \tag{2.1}$$

and is shown in Figure 2.2. The number of forest clouds per unit redshift is seen to be roughly constant in $0 < z \lesssim 1$ and shows a steep increase with $\gamma \sim 2$ at $z \gtrsim 1.5$ (Kim et al., 2002). This suggests a significant evolution in the population of Lyman-α forest systems. However, the sample may be affected by incompleteness at very low redshifts and for very low column densities due to non-detectability in low S/N UV spectra. Another important property of the Lyman-α forest is that it appears similar along sight lines in any direction, implying large scale uniformity and isotropy.

The class of quasar absorbers appearing above the Lyman-α forest on the N_{HI} scale is called Lyman-limit systems (LLSs). These absorbers with $19.0 \gtrsim \log N_{HI} > 17.2$ contain gas which is denser and more neutral compared to that in Lyman-α forest clouds. At $\log N_{HI} = 17.2$, a cloud becomes optically thick ($\tau = 1.0$) at 912 Å (the limit of the Hydrogen Lyman series, corresponding the ionization potential of H). This column density, therefore, marks a physically meaningful boundary between the mostly ionized forest systems and the moderately ionized Lyman-limits systems. The neutral fraction of Hydrogen increases with increasing N_{HI} due to self-shielding effects. An important property of the Lyman-α line profile is its change in shape with increasing N_{HI}. As shown in Figure 2.3, the Voigt profile corresponding to a low N_{HI} value is dominated by the Gaussian component determined by the Doppler

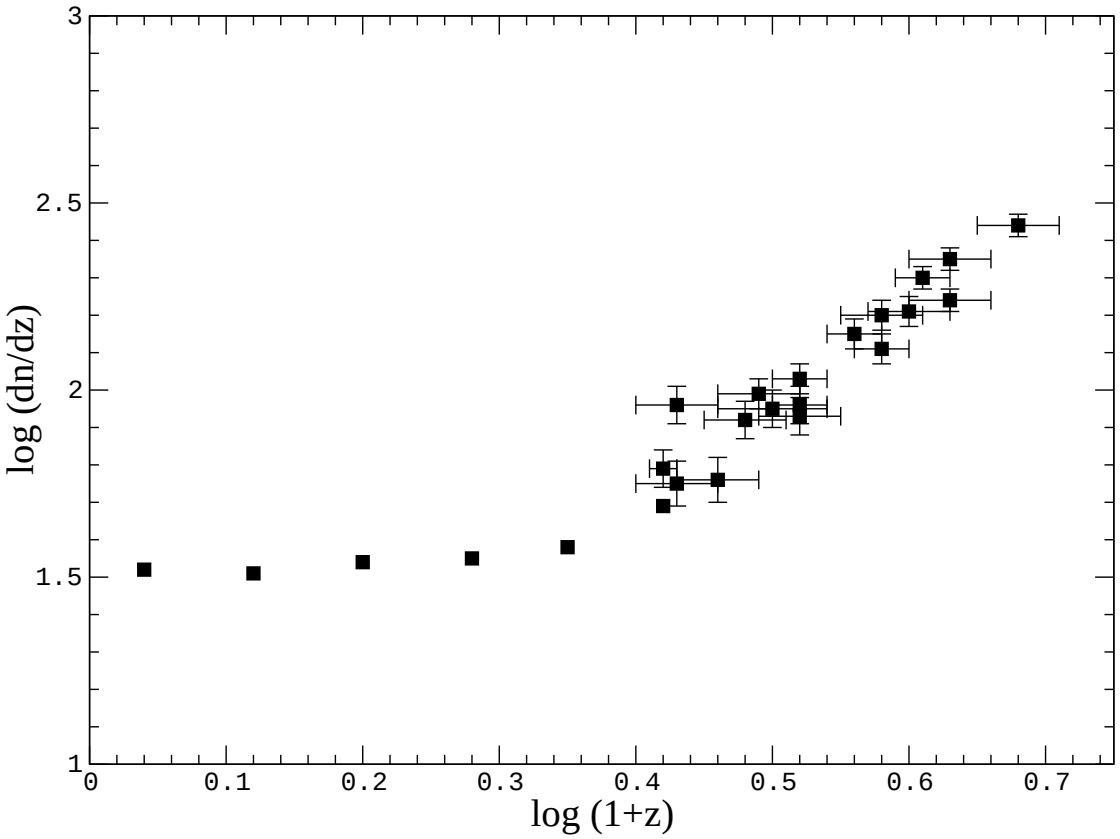

Figure 2.2 The redshift evolution of number density for Lyman-α forest lines. A broken power law fit suggests strong evolution of the Lyman-α forest lines. The data presented in this plot are from Kim et al. (2002).

b-parameter. However, with increasing column density, the Lorentzian component starts to become important and at log $N_{HI} > 19.0$, the damping wings of the the natural line width become evident. Consequently, $N_{HI} = 10^{19}\ cm^{-2}$ marks the boundary between the LLSs and the class of quasar absorbers giving rise to damped Lyman-α lines. The Lyman-limit systems are believed to trace gas around galaxies (the circum galactic medium). Lehner et al. (2013) reported a bimodality in terms of metallicity in a sample of 28 LLSs and suggested that while the metal-poor branch trace cold accretion streams, the metal-rich branch is likely to originate in winds, recycled outflows and tidally stripped gas from galaxies. However, owing to the high ionization fraction in LLSs, their observed metallicities may not represent true chemical enrichment in the gas unless the observations are corrected for ionization effects (see Chapter 4 for

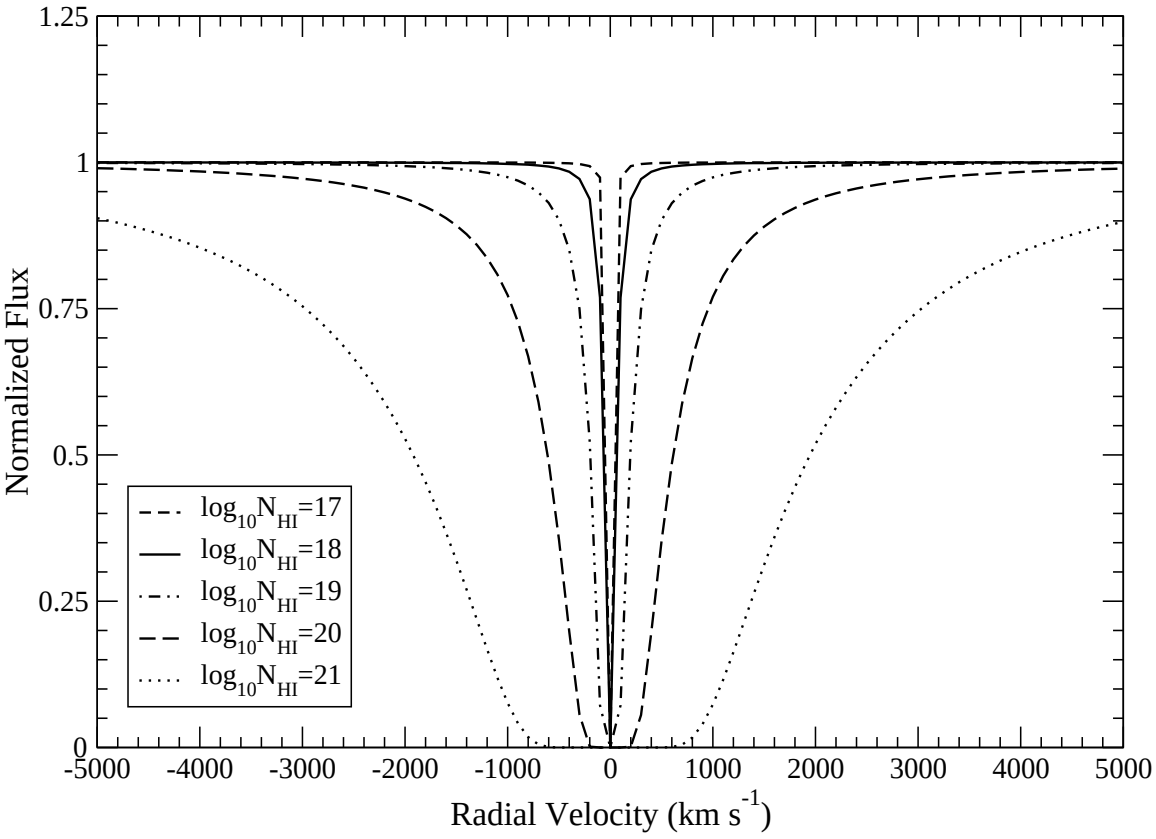

Figure 2.3 Theoretical Voigt profiles for the H I Lyman-α transition with $b = 10$ km s^{-1} and column densities of 10^{17}, 10^{18}, 10^{19}, 10^{20} and 10^{21} cm^{-2}. The Lorentzian profile increasingly dominates the Voigt profile with rising N_{HI}. The damping wings start to become evident for log $N_{HI} \gtrsim 19.0$

more details).

Systems with log $N_{HI} > 19.0$ are the highest column density quasar absorbers and trace large amounts of neutral gas. For reasons described in Section 2.3, these absorbers are believed to be associated with galaxies along the sight lines and are extremely important for chemical evolution studies. These systems are further sub-divided into two classes; the sub-damped Lyman-α systems ($19.0 \leq$ log $N_{HI} < 20.3$) or sub-DLAs, and the damped Lyman-α systems (log $N_{HI} \geq 20.3$) or DLAs. The boundary ($N_{HI} = 10^{20.3}$) between sub-DLAs and DLAs is arbitrary and historically resulted from the initial DLA surveys carried out with low-resolution spectrographs. This column density represents the lower limit of the strengths of the features detected

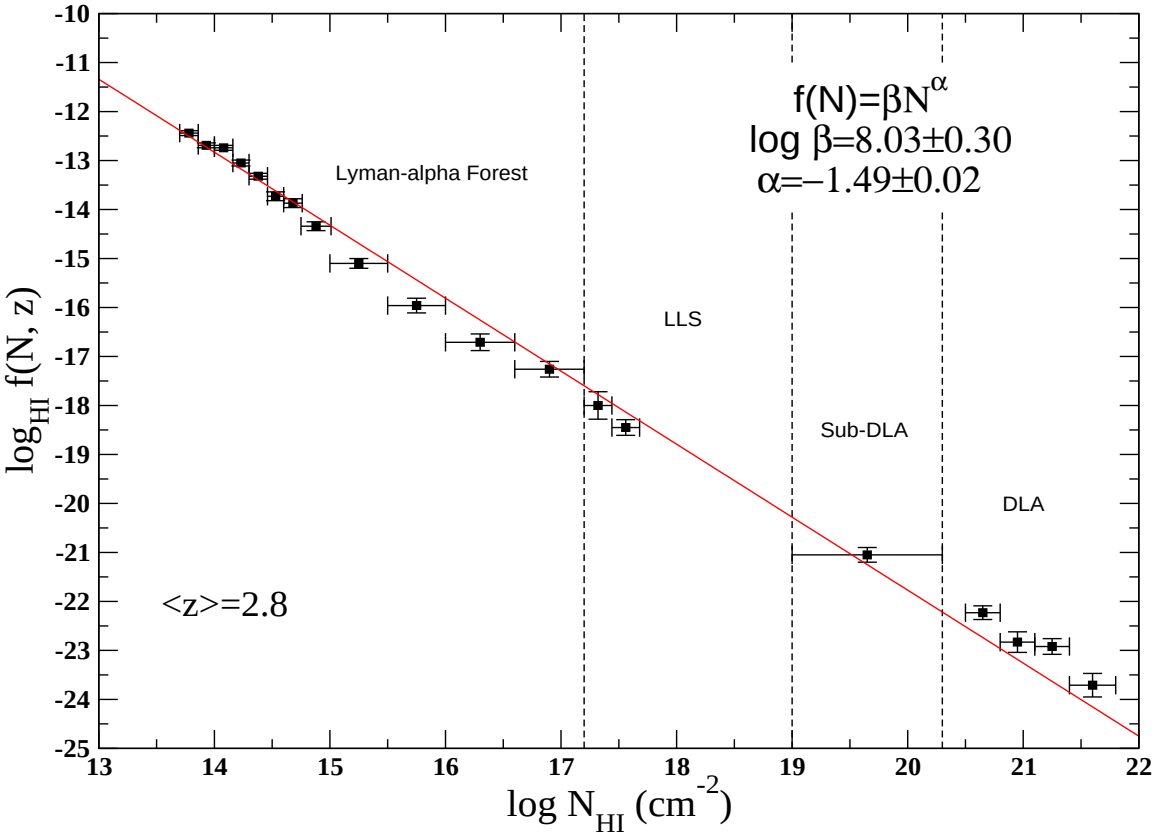

Figure 2.4 The Column Density Distribution Function (CDDF) at $< z >= 2.8$ for Lyman-α lines in quasar spectra. The Lyman-α forest, LLS and DLA data are from Petitjean et al. (1993) and the sub-DLA data are from Péroux et al. (2003b). The solid red line represents a single power law with index $\alpha = -1.49$ which provides a reasonable fit to the data over ~ 8 orders of magnitude.

in these studies. However, although a sharp boundary between sub-DLAs and DLAs does not exist, the sub-DLAs and DLAs seem to differ in various aspects which will be discussed in due course.

A fundamental property of quasar absorption line systems is that the rate of incidence decrease with increasing column density. This is demonstrated via the column density distribution function (see Fig. 2.4). The column density distribution function (CDDF) at a redshift z is defined as the number of absorbers in a given column density range $(N,\ N + \Delta N)$ detected in m-number of quasar spectra with a total absorption distance of $\sum_{i=1}^{m} \Delta X_i$ and can be written as

$$f_{HI}(N,z)dNdX = \frac{n}{\Delta N \sum_{i=1}^{m} \Delta X_i} dNdX. \tag{2.2}$$

In the equation above, $X(z)$ is the absorption distance defined as

$$\frac{dX}{dz} = \frac{(1+z)^2}{[\Omega_\Lambda + \Omega_m(1+z)^3 + \Omega_r(1+z)^4 + (1-\Omega)(1+z)^2]^{\frac{1}{2}}}, \tag{2.3}$$

where Ω_Λ, Ω_m and Ω_r are the vacuum, matter and radiation energy density parameters, respectively (the total energy density parameter, Ω, is given by $\Omega = \Omega_\Lambda + \Omega_m + \Omega_r$). The zeroth moment of the CDDF gives the total number of absorbers (at redshift z) per redshift interval,

$$\frac{d\mathcal{N}}{dX} = \int_{N_{min}}^{N_{max}} f_{HI}(N,z)dN. \tag{2.4}$$

Figure 2.4 clearly shows that the weakest Lyman-α forest systems are much more numerous in quasar spectra than the DLAs and sub-DLAs. The solid red line in the plot represents a single power law fit with index $\alpha = -1.49$ and coefficient $\beta = 8.03$. The CDDF, however, is difficult to constrain at low redshifts as the redshift path is lower for low z quasars decreasing the probability of intersection with an absorber (Péroux et al., 2003b). The requirement of space based UV observations to detect low redshift Lyman-α lines and the incompleteness introduced due to non-detectability of very low N_{HI} lines also contribute to this problem.

In addition to the Lyman-α line, absorption features corresponding to various elements are produced by quasar absorption systems and these lines can be measured to determine the chemical abundances in these systems following equations 1.57 and 1.58. These lines are detected more frequently in the highest N_{HI} systems, i.e, in sub-DLAs and DLAs. Many elements such as Ar, C, N, O, P, Mg, S, Si, Ca, Ti, Cr, Mn, Ni, Fe, Zn have been detected in quasar absorption systems and can be used to shed light on the chemical enrichment histories of the gas they represent. Although Fe has been extensively used to determine metallicity of stars, it is not a reliable metallicity

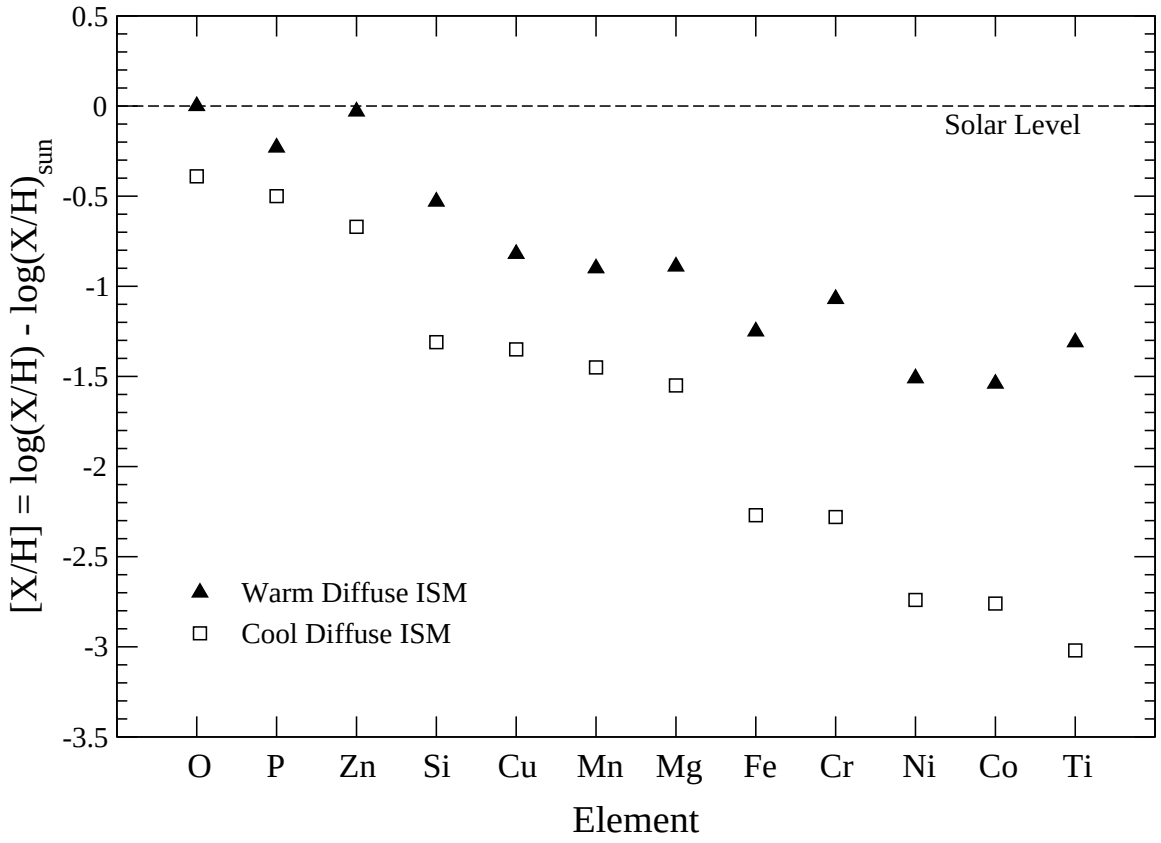

Figure 2.5 Abundance pattern (relative to the Solar abundance) of various elements in the warm and cool diffuse ISM clouds in the sight line towards ζ Oph. The elements are arranged in the order of increasing condensation temperatures. As expected, the elements with low condensation temperatures have solar or near-solar abundances i.e, they show little or no depletion onto dust grains, especially in the warm ISM. On the other hand, elements with higher condensation temperatures show moderate to high depletion. (Based on Savage & Sembach 1996b)

indicator for interstellar gas due to its depletion onto dust grains (see Fig. 2.5). Zn, on the other hand, is found to be relatively undepleted in the Galactic ISM, especially for warm diffuse gas with low molecular fraction of H. This is typically the case with quasar absorption systems and therefore, Zn is usually the preferred tracer of gas phase metallicity in quasar absorbers. Another advantage of using Zn is that the lines Zn II $\lambda\lambda 2026, 2062$ used to measure N_{Zn} are relatively weak and therefore, the abundance is relatively free from saturation effects, especially for high N_{HI} systems. S, with its low condensation temperature is another reliable indicator of gas phase

metallicity and are often used in abundance studies when Zn is not available.

2.3 Properties of DLA and sub-DLA Absorbers

The damped Lyman-α systems (DLAs and sub-DLAs), although rare, are believed to contain majority of the neutral gas in the Universe. The cosmological neutral gas mass density of absorbers with $N_{min} < N_{HI} < N_{max}$ can be determined from the first moment of $f_{HI}(N, z)$ as

$$\Omega_g = \frac{H_0 \mu m_H}{c \rho_{crit}} \int_{N_{min}}^{N_{max}} N f(N, z) dN, \tag{2.5}$$

where ρ_{crit} is the critical density, m_H is the mass of hydrogen atom, and μ is the mean molecular weight which takes into account the contributions from He. The observed CDDF at various redshifts indicate that most of the contribution to Ω_g come from DLAs and sub-DLAs. Using a single power law fit to the observed data, such as the one seen in Figure 2.4, Lanzetta, Wolfe, & Turnshek (1995) estimated that $\sim 90\%$ of the neutral gas estimated from quasar absorption line systems resides in DLAs. The contribution of sub-DLAs to Ω_g increases with redshift and $\Omega_g^{sub-DLA}$ becomes comparable with Ω_g^{DLA} at high z (Péroux et al., 2003b; Zafar et al., 2013). Moreover, the cosmological gas mass density at $z \sim 3.5$ determined from the damped Lyman-α systems has been found to match the cosmological stellar mass density (Ω_s) in the local Universe ($z = 0$) very closely (Lanzetta, Wolfe, & Turnshek, 1995). This implies that the neutral gas contained in high N_{HI} systems at high redshifts is sufficient to produce all the stars in the local Universe. Thus, DLAs and sub-DLAs are believed to probe largely neutral, star forming gas in the distant Universe and offer an opportunity to study the progenitors of modern day galaxies (Storrie-Lombardi & Wolfe, 2000; Péroux et al., 2003b). Indeed, several low-z DLA host galaxies have been confirmed through deep imaging and follow-up spectroscopy (e.g., Chen $ Lanzetta 2003;

Gharanfoli et al. 2007). These systems offer the most precise element abundance measurements in distant galaxies, independent of electron temperature, complementing the emission-line abundances in Lyman-break galaxies (LBG's) or star-forming UV selected galaxies (e.g., Shapely et al. 2004; Erb et al. 2006). The metallicities, relative abundances, and gas kinematics of DLAs/sub-DLAs provide unique indicators of the star formation history, regardless of galaxy redshift or morphology. In the era of precision cosmology, the snapshots of galaxy properties offered by DLAs/sub-DLAs are crucial for constraining the cosmic densities of gas and metals and their evolution (e.g., Kulkarni et al. 2007).

Owing to their high N_{HI}, DLAs have historically been the focus of chemical abundance studies (Prochaska & Wolfe, 2002; Kulkarni et al., 2005; Meiring et al., 2006). However, most DLAs have been found to be metal poor, typically far below the solar level ($\sim 20\% Z_{\odot}$ at $z = 0$) and below the model predictions for the mean metallicity (see Section 1.3) at the corresponding redshifts at which they are seen (e.g, Kulkarni et al. 2005, 2007, 2010; Péroux et al. 2006b; Battisti et al. 2012; Rafelski et al. 2012 and references therein). The mean metallicity of DLAs show little evolution with time except a sharp drop at $z \sim 5$ reported recently by Rafelski et al. (2014). Thus, study of chemical evolution in galaxies using DLAs alone lead to a deficiency of metals in the low redshift Universe. A missing metals problem was also noted in high-z DLAs from star formation rate (SFR) estimates based on C II* absorption (Wolfe et al., 2003). In fact, after adding up the metal content of known DLAs, Ly-α forest, UV-selected galaxies, and sub-mm galaxies, $\gtrsim 1/3$ of the predicted metals at $z \sim 2$ appear to be missing (e.g., Pettini 2006; Bouché et al. 2007).

Study of chemical abundances of sub-DLA systems had not attracted much attention until recently, although the CDDF suggests sub-DLAs to be ∼4 more numerous than DLAs and therefore better probes of neutral gas in terms of availability. Péroux et al. (2003b) suggested, based on a small sample of ~ 20 sub-DLAs, that these lower

column density absorbers could show a faster metallicity evolution than DLAs. However, their conclusion was based on metallicity measurements using Fe and therefore could be affected by depletion. Subsequent studies of chemical abundance in sub-DLAs at $0.6 \lesssim z \lesssim 1.5$, using Zn or S as metallicity indicators, have shown that chemical evolution of sub-DLAs is indeed different from that of DLAs (Péroux et al. 2006a; Meiring et al. 2007, 2008, 2009a,b; Nestor et al. 2008; Dessauges-Zavadsky et al. 2009; and references therein). In this redshift range, sub-DLAs are typically found to be more metal-rich and evolving marginally faster than DLAs. These findings suggested that, at least in the observed redshift range, sub-DLAs and DLAs could represent progenitors of different populations of present-day galaxies. One possibility is that the gas-poor, metal-rich sub-DLAs may be representing massive galaxies which convert their gas mass into stars at an earlier epoch than the DLA galaxies. In other words, the observed differences between the chemical evolution of DLAs and sub-DLAs at $0.6 \lesssim z \lesssim 1.5$ may be giving us glimpses of the mass downsizing in galaxies where more massive galaxies undergo star formation more rapidly.

However, to obtain a better understanding of the nature of these quasar absorption systems and the galactic chemical evolution they trace, one needs to compare their behavior at a much wider redshift range. While DLAs have been studied extensively over $0 \lesssim z \lesssim 5$, several issues remain unanswered regarding the chemical evolution of sub-DLAs at $z < 0.6$ and $z > 1.5$. An extrapolation of the $z > 0.6$ data to lower redshifts suggests that the mean metallicity of sub-DLAs is solar at $z \sim 0$ (e.g., Kulkarni et al. 2007, 2010; see also York et al. 2006; Prochaska et al. 2006). In fact, sub-DLAs may contribute several times more than DLAs to the cosmic metal budget at $z < 1$ (Kulkarni et al., 2007). However, one of the main issues is whether the observed trends and the extrapolations are reliable, given the small-number statistics, especially at $z < 0.6$, where the samples are particularly sparse. The sub-DLA sample at $z \lesssim 0.6$ consists of a total of 6 Zn or S based metallicity measurements

out of which only two are robust measurements from detected Zn/S lines while the rest are upper-limit estimates. Study of the low-z sub-DLAs is crucial also because they offer an unique opportunity to study their host galaxies via direct imaging and emission spectra and therefore provide firm constraints on the connection between these absorption line systems and their host galaxies. On the other hand, it is essential to trace sub-DLA chemical evolution at $z \gtrsim 1.5$ to investigate the effect of star formation on the observed differences between DLAs and sub-DLAs, given that the global SFR density attained its peak at $z \sim 2-3$ (e.g., Bouwens et al. 2007; Reddy & Steidel 2009). However, there exist a total of 17 metallicity measurements (Zn or S based) at $z > 1.5$, out of which only 10 are based on line detections, resulting in poor constraints on the chemical evolution trends of sub-DLAs in the high redshift regime.

This work is devoted to the study of sub-DLA quasar absorbers at $z \lesssim 0.6$ and $z \gtrsim 1.5$, using UV spectra from the Hubble Space Telescope and high-resolution optical echelle spectra from the Magellan Clay Telescope. Chapter 3 describes the observations, data reduction and analysis techniques used in this work and presents the measurements from our data. Chapter 4 discusses our observations in the context of the properties of sub-DLAs in general. The conclusions made from this study are presented in Chapter 5 along with an outline of futre work.

CHAPTER 3

Observations, Data Analysis and Results

3.1 Sample Selection

With the motivation discussed in the previous chapter, we observed 5 sub-DLAs at $1.7 < z < 2.3$, including 3 at $z > 2$, with the Magellan Inamori Kyocera Echelle (MIKE) spectrograph on the Magellan Clay Telescope. It is to be noted that very few abundance measurements exist for sub-DLAs at these redshifts, especially at $z > 2$ (e.g., Dessauges-Zavadsky et al. 2003, 2009; Ellison & Lopez 2001; Ledoux et al. 2006; Noterdaeme et al. 2008; Pettini et al. 1994). These absorbers were selected based on their N_{HI} values known previously either from the Large Bright Quasar Survey or measured from the Lyα λ 1215.7 line seen in SDSS spectra. However, for the absorbers with the Lyα 1215.7 line falling within the spectral coverage of our MIKE observations (which is the case for all the systems except the absorber toward Q1311-0120), we report N_{HI} values determined from our high resolution data. The H I column densities for the absorbers in our sample lie in the range $19.35 \leq \log N_{HI} \leq 20.00$. We aimed to determine the metallicities of these systems based on

Zn. For the redshift range spanned by our sample, the absorption lines from Zn fall roughly in the middle of the wavelength range covered by the spectrograph, giving high sensitivity to our spectra. Our sample selection criteria also included the brightness of the background quasar. We restricted the sample to moderately bright sightlines (m_V or $m_g < 18.5$) to achieve moderate-to-high signal-to-noise ratio in our spectra (necessary to measure the inherently weak absorption lines from Zn) without being too observationally expensive.

We also observed four sub-DLAs at $0.1 < z < 0.5$ toward quasars with reasonably high NUV/FUV fluxes from GALEX (NUV mag =15.70-17.77 and FUV mag =16.36-18.34) with the Cosmic Origins Spectrograph (COS) on board the Hubble Space Telescope (HST). The N_{HI} values were known for these absorbers from archival low-resolution UV spectra from HST FOS/STIS (e.g., Rao, Turnshek, & Nestor 2006). For the absorbers with the Lyα line falling within the spectral coverage of our COS observations, we report N_{HI} values determined from our higher resolution data. The N_{HI} for the absorbers in our sample lie in the range $19.18 \leq \log N_{HI} \leq 19.63$. Our observations were designed to obtain S based metallicities for these systems.

3.2 MIKE: Observations and Data Reduction

The MIKE spectrograph on the 6.5m Magellan Clay telescope at Las Campanas Observatory is a double sided optical spectrograph (Bernstein et al., 2003). This instrument consists of both a blue and a red camera, providing for simultaneous wavelength coverage from ∼3340 Å to ∼9400 Å. The spectra of the quasars presented here were obtained over 2 separate epochs, 2008 March and 2010 May, respectively. The sightlines were observed in multiple exposures of 1800 to 2700 seconds each, to minimize cosmic ray defects. During data acquisition, seeing was typically $< 1''$, averaging $\sim 0.7''$. The target QSOs were observed with the $1''$x$5''$ slit and the spectra

were binned 2x3 (spatial by spectral) during readout. The resolving power of the MIKE spectrograph is ∼19,000 and ∼25,000 on the red and blue sides respectively with a 1″x5″ slit. Table 3.1 gives a summary of the observations.

Our primary objective was to measure the absorption lines of Zn II, S II, Fe II, Mg II, Si II, Si III, Si IV, C II, C II*, C IV, Cr II, Mn II, Al II and Al III. The wide spectral coverage of MIKE also allowed us to cover lines of P II, C I, Fe III and Mg I for some absorbers. The presence of multiple lines corresponding to most ions helped to remove confusion with Ly-α forest lines and to correct for saturation effects and blends with other absorption features. We designed our exposure times using the m_V or m_g fluxes of the target quasars and the published performance characteristics of the spectrograph. Our aim was to achieve a 3σ detection sensitivity of ~ 0.1 solar level of Zn abundance in our absorbers. Using the H I column density of each absorber, we estimated, using the curve of growth, the corresponding equivalent width limit to detect the Zn II λ2026 line at a 3σ level and designed the exposure times to reach the signal-to-noise ratio (S/N) required for such a detection.

We reduced the spectra using the MIKE pipeline reduction code in IDL developed by S. Burles, J. X. Prochaska, and R. Bernstein. The MIKE software makes use of the overscan region to perform bias subtraction and then flat-fields the data. The software then performs sky-subtraction and extracts the spectral orders using the traces from flat field images. The pipeline calibration code uses Th-Ar comparison lamp exposures, taken before and after each science exposure, to perform wavelengths calibration. The software also corrects for heliocentric velocities and converts the wavelengths to vacuum values. Each individual echelle order was then extracted from the IDL structure created by the pipeline software and corresponding orders from multiple exposures were combined in IRAF using rejection parameters to reduce the effects of cosmic rays. The spectra from these combined orders were then normalized individually, using the IRAF "CONTINUUM" task, with Legendre

polynomial functions to fit the continuum. Typically, these functions were of order five or less.

3.3 HST COS: Observations and Data Reduction

The Cosmic Origins Spectrograph on board the Hubble Space Telescope is capable of producing low-to-medium resolution spectra of point sources with a wavelength coverage of ∼1150 Å to ∼3200 Å (Holland et al., 2014). The observations can be carried out with either the far-ultraviolet (FUV; 1150 − 2050 Å) or the near-ultraviolet (NUV; 1700 − 3200 ang) channel of COS. The spectra presented here were acquired as part of the HST program GO 12536. The observations were obtained with the COS FUV or NUV channels (depending on the redshift of the absorber) in the TIME-TAG mode with the G130M, G160M, or G185M gratings. Each sightline was observed in multiple exposures spanning four offset positions (FP-POS=1-4) for each central wavelength setting in order to minimize the effects of fixed-pattern noise in the detector. For Q0154+0448 and Q2131-1207, one exposure each (for 1412 s and 1462 s, respectively) was lost due to an error in the fine guidance sensors. Table 3.1 summarizes the observations.

Our main goal was to measure the absorption lines of Fe II, Fe III, S II, S III, Si II, and Si III. In addition, our settings also covered lines of C II, C II*, N I, N V, O I, O VI, Si II*, P II, Ar I, Mn II, and/or Ni II for some absorbers. The presence of multiple lines for most ions helps to remove confusion with Ly-α forest lines and to correct for saturation effects. The exposure times were designed using the COS online Exposure Time Calculator and the FUV/NUV fluxes for our target quasars. Our goal was to reach a 3σ sensitivity of 0.1 solar metallicity in our absorbers. Using the H I column density of each absorber, we estimated the S II column density corresponding to a 0.1 solar metallicity, and hence the corresponding equivalent width limit needed

to detect the S II λ1253 line at a 3σ level. We designed the exposure times so as to reach the corresponding S/N needed for each object to reach this limit.

The spectra were reduced and extracted with standard Image Reduction and Analysis Facility (IRAF) and Space Telescope Science Data Analysis System (STSDAS) packages. The data were processed with CALCOS (version 2.19.7) during retrieval via the "On the Fly Reprocessing" (OTFR) system. For Q0154+0448 and Q2131-1207, the OTFR-processing included the compromised exposures mentioned above; therefore these OTFR-processed files were not used in further analysis. The raw data for these two sightlines, after retrieval, were reprocessed without the compromised exposures using CALCOS. The pipeline processed raw TIME-TAG data from each exposure into a flat-fielded, background-subtracted, flux- and wavelength-calibrated one-dimensional extracted (x1d) spectrum (see Massa et al. 2013 for a detailed description of the data flow through FUV and NUV TIME-TAG spectroscopic pipelines). The x1d files corresponding to all the exposures from a single visit were then co-added by the pipeline to produce a single one-dimensional spectrum. The spectra from multiple visits for a sightline (where applicable) were then combined using IRAF. The un-binned spectra used for the analysis have dispersions of $\sim$ 9.6 mÅ pixel^{-1} and $\sim$ 37 mÅ pixel^{-1} for FUV and NUV, respectively. The S/N near the S II $\lambda\lambda$ 1250, 1253, 1259 triplet are in the range $\sim$ 7-8 pixel^{-1} for the FUV data and $\sim$ 17-30 pixel^{-1} for the NUV data. The spectra were continuum-fitted with cubic spline or Legendre polynomial functions using the IRAF "CONTINUUM" task. The continuum-normalized spectra were then used for identifying and measuring absorption features at the known sub-DLA redshifts.

3.4 Determination of Column Densities

Column densities were determined by fitting the normalized absorption profiles using the FITS6P package (Welty et al., 1991), which has evolved from the code by Vidal-Madjar et al. (1977). FITS6P iteratively minimizes the χ^2 value between the data and a theoretical Voigt profile that is convolved with the instrumental profile. A discussion of our profile-fitting technique can also be found in Khare et al. (2004). The atomic data used in the identification of lines and profile fitting were adopted from Morton (2003). While a few oscillator strengths have been improved recently (see, e.g., Kisielius et al. 2014 for S II), the changes are relatively small (e.g., ≈ 0.04 dex for S II).

For the absorbers toward Q1039-2719, Q1103-2645, Q1551+0908, Q2123-0050, Q0154+0448 and Q0441+4313, our data covered corresponding the H I Ly-α absorption lines. In these cases, the H I column densities were estimated using Voigt profile fitting. These Voigt profile fits are shown in Figs. 3.1 - 3.3. Our N_{HI} values match within $1-2\sigma$ with those estimated from lower resolution SDSS or HST spectra in past studies (e.g., Petitjean et al. 2000; Srianand & Petitjean 2001; Noterdaeme et al. 2009; Kaplan et al. 2010; Rao, Turnshek, & Nestor 2006).

The fits to the metal line absorption profiles seen in our data used multiple components, tailored to the individual system. For the central, core components, the Doppler parameters (b_{eff}) and radial velocities (with respect to the redshift determined from the Ly-α absorption) were determined from the weaker and less saturated lines such as Fe II λ 1082, S II λ 1253, Fe II λ 2374 and Mg I λ 2852. For the weaker components at higher radial velocities, the b_{eff} and component velocity values were determined from stronger transitions such as N II λ 1084, Si II λ 1193, Fe II $\lambda\lambda$ 2344, 2382 and Mg II $\lambda\lambda$ 2796, 2803. Thus, a set of b_{eff} and v values were determined that provide reasonable fits to all of the lines observed in the system. For each

absorber, we adopted the minimum number of velocity components that were necessary to explain all the absorption lines observed. This was done to avoid over-fitting and erroneous column density determinations, especially in the case of the moderate spectral resolution and S/N spectra from COS.

If a multiplet was observed, the lines were fitted simultaneously. For all of the high-z systems, the Fe II λ 2344, 2374, 2382 lines were fitted simultaneously to arrive at a set of column densities that provide reasonable fits to the spectra. Similarly, the Mg II $\lambda\lambda$ 2796, 2803 lines were also fitted together. At the resolution of our data, the Zn II λ 2026 line is blended with the Mg I λ 2026 line. The Mg I contribution to the blend was estimated using the Mg I λ 2852 line, for which fλ $\sim$32 times that of the Mg I λ 2026 line. The Zn II contribution was determined by fitting the rest of the blend while keeping the Mg I contribution fixed. N_{CrII} was determined by simultaneously fitting the Cr II λ 2056 line and the blended Cr II + Zn II λ 2062 line, where the contribution from Zn II was estimated from the Zn II + Mg I λ 2026 line. In the case of the low-z absorbers, the lines in multiplets such as S II $\lambda\lambda$ 1250, 1253, 1259; Si II $\lambda\lambda$ 1021, 1193, 1260; N I $\lambda\lambda$ 1199.6, 1200.2, 1200.7, were fitted simultaneously. The contribution from Si II, as obtained from the typically saturated Si II λ 1193 or Si II λ 1260 (if the former was not available), to the blend between Si II λ 1190.2 and S III λ 1190.4, was used to obtain an upper limit on the contribution from S III.

Figures 3.4 - 3.14 show the velocity plots (absorption profiles in velocity space) along with the corresponding Voigt profile fits for the observed metal lines in the various absorbers in our sample. Tables 3.2 - 3.12 list the Voigt profile fit parameters, i.e., the radial velocities in km s^{-1}, the effective Doppler parameters (b_{eff}, and column densities for each component fitted to the various metal ions for each absorber. The column densities in the weaker components that could not be well constrained due to noise are each marked with "..." in these tables; their contributions to the total column densities are negligible. Total column densities were determined from adding

the column densities of individual components, and the uncertainties in the total column densities were estimated by adding in quadrature the uncertainties in the column densities of the individual components. Tables 3.13 - 3.17 list the total column densities of various ions detected in the sub-DLAs in our sample.

In addition to the Voigt profile fitting method, the package SPECP, also developed by D.E. Welty, was used to determine column densities via the apparent optical depth method (AOD) (Savage & Sembach, 1996). The integrated column densities thus determined were compared with the total column densities determined from the Voigt profile fits and they are found to agree closely (see Tables 3.13 - 3.17). We used SPECP to measure the equivalent widths of various transitions as well. We present the rest-frame equivalent widths (W_0) of various lines in Tables 3.18 and 3.19. The 1σ errors for the equivalent widths are also given and include the effect of both the photon noise and the uncertainty in continuum placement. In the case a line was not detected, the limiting equivalent width was determined from the local signal to noise ratio (S/N), and a corresponding 3σ column density upper limit was determined, assuming a linear curve of growth. Cells with "..." entries represent lines which could not be measured due to one or a combination of the following: lack of coverage, blending with Lyα forest lines, blending with atmospheric absorption bands, very poor S/N due to spectrograph inefficiency at wavelength extremes and coincidence of the line with damaged portions of the detectors.

3.5 Determination of Abundances

The total column density (N_X) for an element X in an absorber, derived as described in section 3.4, and the corresponding N_{HI} were used to determine its abundance [X/H] (relative to Solar) as,

$$[X/H] = log(N_X/N_{HI}) - log(X/H)_\odot,$$

where $log(X/H)_\odot$ represents the Solar system abundance for the element in question. We adopted Solar abundances from Asplund et al. (2009) for the abundance determinations. The relation described above assumes that most of the hydrogen present in the absorbing gas is in neutral state. In addition, the column density for the dominant ion (the ionization stage expected to dominate the distribution of ions under the physical conditions in the presence of neutral hydrogen) of an element was used in the abundance determination, i.e., if XII is expected to be the dominant ionization state for an element X, $[XII/HI] \equiv [X/H]$. The abundances of various elements in the absorbers studied here are given in Tables 3.20 and 3.21. The metallicity for an absorber was determined from N_{ZnII} (derived from measurements on Zn II $\lambda\lambda$ 2026, 2062 lines) or N_{SII} (derived from the S II $\lambda\lambda$ 1250, 1253, 1259 lines). Sulphur was adopted as the metallicity indicator when the Zn lines were not covered in our data (in the case of the low-z absorbers) or when the Zn lines could not be detected (for the absorbers toward Q1103-2645 and Q1551+0908).

3.6 Discussion of Individual Absorbers

3.6.1 Q1039-2719, z_{abs}=2.139

The sightline to this moderately bright BAL QSO traces a strong sub-DLA system at $z_{abs} = 2.139$ in addition to a weak absorber at $z_{abs} = 2.082$ and three broad absorption systems at $z_{abs} = 1.518, 1.702, 1.757$ (Srianand & Petitjean, 2001). The continuum around the Lyman-α line of the sub-DLA is affected by Si IV absorption from the BAL systems at $z_{abs} = 1.702$ and 1.757 as well as N V absorption from the $z_{abs} = 2.082$ absorber. A relatively un-affected part of the spectrum redward of the Lyman-α line was used to constrain the continuum. We made use of the residual flux at ∼3815

Å to eliminate contribution from the N V $\lambda\lambda$ 1239, 1243 lines in the z_{abs} = 2.082 absorber as well as from the Lyα forest and to estimate log N_{HI} = 19.55±0.15. The Voigt profile fit to the Lyman-α line is shown in the upper panel of Figure 3.1.

The absorption profiles of this sub-DLA system show three strong components at velocities -9, 10, and 46 km s^{-1} along with several weak satellites spanning a total $\sim$ 430 km s^{-1}. The sub-DLA is detected in absorption from several elements in multiple ionization stages such Mg I, Mg II, Fe II, Fe III, Si II, Si III, Si IV, C I, C II, C IV, Al II, Al III, P II, Cr II, Mn II, Ni II, S II and Zn II. Table 3.2 shows the column densities in individual velocity components for various ions. Total column densities of various ions detected in this system are listed in Table 3.13. The Voigt profile fits to some of the lines of interest are shown in Figure 3.4. It is to be noted that, abundance measurements for various elements in this absorber have previously been reported by Srianand & Petitjean (2001). However, their results included measurements from the two strongest absorption components only and contributions from the weaker components, although small, were ignored. Therefore, the abundances were affected by underestimation of column densities of various ions, including Zn II and S II. To check the consistency of our abundance determinations from the MIKE spectra, we derived column densities of various ions (e.g., log N_{SII} = 14.76±0.09, log N_{FeII} = 14.69±0.06, log N_{SiII} = 14.99±0.01) using AOD measurements on the UVES spectra from Srianand & Petitjean (2001) and compared them with our results. For most of the ions, the column densities agree within 1σ uncertainties. We also detect C II* λ 1335.7 in this sub-DLA, but the components of C II* at velocities -9 and 10 km s^{-1} are blended with the C II λ 1334 line in our MIKE spectrum. Although, we were able to measure the contribution from the component at 10 km s^{-1} using the higher resolution UVES data from Srianand & Petitjean (2001), the component at -9 km s^{-1} could not be separated from the blend, resulting in the placement of only a lower limit on the abundance of C II*. The C II* column densities listed in Table 3.2 are from our

measurements on the UVES data. Photoionization calculations for this system, as described in section 4.2, suggest that the observed metallicity ([Zn/H] = −0.02 dex) and depletion ([Zn/Fe] = +0.28 dex) underestimate the true values significantly. The corrected values for [Zn/H] and [Zn/Fe] were estimated to be +0.46 dex and +0.95 dex, respectively.

3.6.2 Q1103-2645, z_{abs} = 1.839

This QSO sightline probes a sub-DLA at z = 1.839 (Petitjean et al., 2000). We estimate log N_{HI} = 19.52±0.04 for the absorber by fitting a Voigt profile to the Lyman-α line (see the lower panel of Figure 3.1). Absorption features of various elements in different ionization stages such as Mg I, Mg II, Fe II, C II, C II*, S II, Si II, Si IV and Mn II, were detected in this system. The absorption profiles reveal 11 components ranging from -163 km s^{-1} to 39 km s^{-1} but most of the absorption comes from two main components at -49 and -12 km s^{-1}. Several key lines such as C IV $\lambda\lambda$ 1548, 1550; Al IIλ 1670 and Ni II λ 1741 fell on a damaged portion near the red end of the blue CCD of MIKE, preventing us from making reliable determination of column densities.

Table 3.3 summarizes the results from profile fitting analysis for this system and the velocity plots for some of the lines of interest are shown in Figure 3.5. Total column densities are listed in Table 3.13. There was no detection of Zn with a S/N $\sim$ 45 near Zn II λ 2026. Based on the 3σ limiting rest equivalent width, W_{rest} = 3.9 mÅ, we estimate log N_{ZnII} < 11.3 and [Zn/H] < -0.82 for this absorber. S II was detected in this system with log N_{SII} = 13.9 and [S/H] = -0.82. We note that, [S/H] for this system has also been reported by Petitjean et al. 2000 and their value of -0.94±0.16 is consistent with our measurement within 1σ uncertainties. Ionization modelling for this absorber indicates a moderate correction of -0.3 dex in S abundance (see 4.2). The data also show presence of Mn II λ 2576 but this line is blended with

an unidentified feature. Since no other Mn II lines were detected, we could only place an upper limit on Mn abundance of this absorber.

3.6.3 Q1311-0120, $z_{abs} = 1.762$

This QSO sightline has a sub-DLA absorber, identified in the LBQS survey (Wolfe et al., 1995), at $z = 1.762$ with Lyman-α rest-frame equivalent width of 7.3±0.7 Å. The Lyman-α line was partially covered in the extreme blue order of our echelle data and because of the very poor S/N in that wavelength region, neutral hydrogen column density could not be determined using a Voigt profile fit. Instead, we estimate log N_{HI} = 20.00±0.08 from the rest-frame equivalent width reported by Wolfe et al. (1995), using the curve of growth for the H I Lyman-α line. This absorber shows a relatively complex velocity structure and 12 components, spanning $\sim$ 550 km s^{-1} in velocity space were required to fit the observed absorption profiles. While most of the absorption occurs in two component clusters appearing between -5 km s^{-1} and 200 km s^{-1}, a weaker absorption complex, separated from the main components by more than 500 km s^{-1}, is detected in most of the strong transitions. Additional weaker components, bridging the gap between the satellite and the main absorption, are seen only in the strongest of transitions such as Fe II λ 2382 and Mg II $\lambda\lambda$ 2796, 2803. Results from the profile fitting analysis for this system are shown in Table 3.4, while total column densities for the ions are listed in Table 3.13.

Our data near the extreme blue end of the spectral coverage were affected by poor S/N owing to the combination of lower sensitivity and continuum absorption form the Lyα forest clouds. Several of the lines of interest such as S II $\lambda\lambda\lambda$ 1250, 1253, 1259; Si II λ 1304; Ni II $\lambda\lambda$ 1317, 1370; C II λ 1334; C II* λ 1336 and Si IV $\lambda\lambda$ 1393, 1402 were located in this region and therefore could not be analyzed reliably. Due to the high redshift of the background QSO, even lines with higher rest wavelengths such as C IV $\lambda\lambda$ 1548, 1550 were blended with Lyα forest lines. Si II λ

1526 was partly blended with forest lines resulting in the placement of only a lower limit on Si II abundance. Zn II λ 2026 line was detected in several components in this system. However, a part of the core component structure of the line is blended with a strong unidentified feature and therefore, we report only a lower limit of log $N_{ZnII} > 12.57$ and [Zn/H] > -0.06, based on the measurements of the un-blended components. The component at 546 km s^{-1}, unlikely to be associated with the main absorber galaxy, contributes $\sim$ 15% of the observed Zn II column density. However, the system is found to be metal rich ([Zn/H] > -0.14) even if contribution from this high-velocity component is ignored. This near-solar metallicity absorber also shows a high depletion with [Zn/Fe] > +1.18. Ni II λ 1741 and Al II λ 1670 were affected by cosmetic defect in the chip, however, we were able to place a lower limit on Al II abundance based on unaffected regions in the line. Velocity plots for several lines of interest are shown in Figure 3.6.

3.6.4 Q1551+0908, $z_{abs} = 2.320$

This QSO sightline has a sub-DLA absorber at $z = 2.320$ (Noterdaeme et al., 2009). A Voigt profile fit to the Lyman-α line, shown in the upper panel of Figure 3.2, yields log N_{HI}=19.70$\pm$0.05. This sub-DLA is detected in absorption from Fe II, Fe III, Si II, Si IV, C II, C III, C IV, Al II, Al III, S II, and Ni II. Mg I λ 2852 and Mg II $\lambda\lambda$ 2796, 2803 were not covered. The observed absorption profiles show a relatively simple velocity structure for this system requiring 5 components for an adequate fit. Table 3.5 shows results from profile fitting analysis for this absorber. Zn II λ 2026 was not detected in our data with S/N $\sim$ 40 near the expected position of the line. Our estimate of a 3 σ limiting rest-frame equivalent width of $W_{rest} = 4.38$ mÅ places an upper limit on the Zn II column density at log $N_{ZnII} < 11.38$ and [Zn/H] < -0.95. Measurement of the detected S II lines yield [S/H] = -0.46 and suggest significant α-enhancement with [S/Zn] > 0.49. Figure 3.7 shows velocity plots for several lines

of interest along with their Voigt profile fits. Table 3.13 summarizes the total column densities.

3.6.5 Q2123-0050, $z_{abs} = 2.058$

This quasar sightline traces a sub-DLA at $z = 2.058$ (Kaplan et al., 2010) with log $N_{HI} = 19.35 \pm 0.10$. The lower panel of Figure 3.2 shows the Voigt profile we used to determine the neutral hydrogen column density for this system. A complex structure with 13 components spanning more than 350 km s^{-1} in velocity was required to model the absorption characteristics of the sub-DLA. Details of the absorption structure analysis are given in Table 3.6. Table 3.13 summarizes the total column densities. Absorption signatures from various ions such as Mg I, Mg II, Fe II, Si II, Si IV, Al II, Al III, C II, C II*, C IV, Mn II, Ni II, S II and Zn II were detected in QSO spectrum at the sub-DLA redshift. Figure 3.8 shows the velocity plots of several lines of interest along with their Voigt profile fits. The metallicity of this system, based on the observed Zn II column density of log $N_{ZnII} = 12.23$, is super-solar ([Zn/H] = +0.25), making it the most metal-rich sub-DLA QSO absorber known so far at $z > 2$ (we note here, that higher metallicities in some lower-redshift sub-DLAs have been reported by Meiring et al. 2007, 2008, 2009b; Péroux et al. 2006a, 2008; Prochaska et al. 2006). In any case, due to the relatively low N_{HI} of this absorber, it is necessary to explore the extent of ionization effects on the metallicity value. Indeed, the observed high values of column density ratios between adjacent ions such as Al III/Al II, Si III/Si II, and Al III/Fe II in this absorber suggest a high level of ionization. Our photoionization calculations indicate a correction of +0.59 dex for [Zn/H] (see section 4.2 for further details on photonionization modelling).

3.6.6 Q0154+0448, $z_{abs} = 0.1602$

Bergeron et al. (1988) discovered two spiral galaxies of Sbc and Scd types at $z = 0.1592$ and $z = 0.1597$ with angular separations of 6.4″ and 10.9″ from the quasar Q0154+0448, corresponding to impact parameters of 17.7 and 30.1 kpc, respectively. They also discovered an Mg II absorption system at $z = 0.1602$ in the spectrum of Q0154+0448, and suggested that this absorber was associated with either of the two spiral galaxies.

From an analysis of archival HST FOS spectra, Rao & Turnshek (2000) found that the $z = 0.1602$ system is not a DLA. Analysis of these archival HST spectra suggested an H I column density of log $N_{HI} = 19.70^{+0.15}_{-0.22}$ (see Christensen et al. 2005). Our HST COS observations gave a higher quality spectrum of the Ly-α line. The upper panel of Figure 3.3 shows the result of Voigt profile fitting for this Ly-α line, from which we obtain log $N_{HI} = 19.48 \pm 0.10$. Our COS data also targeted lines of S II, S III, Si II, Si III, Fe II, C II, P II, N I, N V, O I, and O VI. Figs. 3.9 and 3.10 show the velocity plots for the various metal lines in this absorber. Tables 3.7 and 3.8 list the results of the Voigt profile fits for the lower ions and the higher ions, respectively. Table 3.14 summarizes total column densities for various ions.

Strong N II, N V, and O VI absorption is detected in this system. The components in the low ions show a velocity spread of ~ 200 km s^{-1}, while the higher ions extend over a total of ~ 460 km s^{-1}. The O VI λ1032 profile is especially strong and striking, and shows strong asymmetry, possibly suggesting the presence of outflows. The O VI λ1037 line is consistent with O VI λ1032, but has additional absorption in some components due to blends with other unrelated absorption. The implied O VI column density is much higher than in diffuse interstellar clouds in the Milky Way, such as that toward α-Vir (e.g., York & Kinahan 1979).

3.6.7 Q0441+4313, $z_{abs} = 0.1012$

This absorber is known to have strong absorption lines of Mg II, Fe II, Si II, Al II, and C IV. A galaxy at $z = 0.101$ has been detected at an impact parameter of 7.6 kpc from the quasar (Petitjean etal, 1996; Chen et al., 2005). Petitjean etal (1996) suggested that the Mg II absorber in this sightline is a DLA. Kanekar et al. (2001) reported a weak 21-cm absorber in this sightline, with an estimated spin temperature of $\gtrsim 730$ K. Based on an absence of 21-cm emission, they estimate a 3σ upper limit to the gas mass of the absorber of $2.25 \times 10^9 M_\odot$. Thus, they claim that this galaxy is not a large, gas-rich spiral.

The lower panel of Figure 3.3 shows our Voigt profile fit to the Ly-α feature in this absorber, which gives the H I column density of $\log N_{HI} = 19.63 \pm 0.15$. Our COS spectra of this absorber reveal lines of several metal ions, i.e. N I, N II, N V, O VI, Si II, Si II*, P II, S II, S III, Ar I, Mn II, Fe II, and Fe III. Figs. 3.11 and 3.12 show the velocity plots for the various metal lines in this absorber. Table 3.9 lists the Voigt profile fitting results for the lower ions, while Table 3.10 lists the results for the higher ions. Column densities for various ions in this system are listed in Table 3.15.

This absorber shows strong N II absorption and also shows N V and O VI. This indicates a significant amount of ionized gas in this absorber. The velocity spread of the higher and lower ions is comparable, and relatively large (~ 400 km s^{-1}).

3.6.8 Q0456-2159, $z_{abs} = 0.4744$

Rao, Turnshek, & Nestor (2006) report $\log N_{HI} = 19.45^{+0.02}_{-0.03}$ for this absorber, based on archival HST UV spectra. Robertson et al. (1988) reported the discovery of Mg II, Ca II, and Fe II absorption in this absorber from moderate-resolution spectra obtained at the Anglo-Australian Telescope (AAT). Based on curve of growth analysis, they reported $\log N_{MgII} = 15.48$, $\log N_{CaII} = 12.20$, and $\log N_{FeII} = 14.90$. Based on

data from the Keck High-Resolution Echelle Spectrometer (HIRES), several velocity components appear to be present in this system (Churchill et al., 2000). Churchill & Vogt (2001) provide column density estimates for Mg I, Mg II, and Fe II from the HIRES data. Using the apparent optical depth (AOD) method, they estimate total column densities log $N_{MgII} > 14.27$ and log $N_{FeII} > 14.52$, which are consistent with the estimates of Robertson et al. (1988). For Mg I, Robertson et al. (1988) estimated log $N_{MgI} = 12.18$, while Churchill & Vogt (2001) reported log $N_{MgI} = 12.53 \pm 0.01$. The latter value is likely to be more accurate than the former, owing to the much higher spectral resolution of the Keck data (0.09 Å) compared to that of the AAT data (1.4-2.0 Å); in any case, both Mg I values are far smaller than the Mg II column density. These measurements (without ionization corrections) would imply [Mg/H] = 0.43, [Fe/H] = -0.05, and [Ca/H] = -1.59 dex. The relative abundances [Ca/Fe] = -1.54 and [Ca/Mg] = -2.02 imply large depletions of Ca.

Figure 3.13 shows velocity plots from our HST COS data for the various metal lines in this absorber. Table 3.11 lists the Voigt profile fitting results. Total column densities are summarized in Table 3.16. Our measurements indicate [S/H] = 0.45 ± 0.04, in close agreement with the [Mg/H] value estimated from the data of Robertson et al. (1988). Likewise, our measurement of [Ni/H] = 0.01 ± 0.08 is in close agreement with [Fe/H] = -0.05 estimated by Robertson et al. (1988). This agreement is reassuring, given that S and Mg are both α elements, while Ni and Fe are both Fe-group elements. Nucleosynthetic differences are not expected between S and Mg, or between Fe and Ni. [Mg/S] = -0.02 would suggest that dust depletion may not play a significant role in this absorber. Moreover, this absorber appears to show an intrinsic nucleosynthetic enhancement of the α-elements with respect to the Fe-group elements.

The components detected in the low ions covered in our data show a velocity spread of ~ 170 km s^{-1}. Our data did not cover N II λ1084, or lines of higher ions

such as N V $\lambda\lambda 1239, 1243$, O VI $\lambda\lambda 1032, 1037$ or Si III $\lambda 1207$ in this absorber.

3.6.9 Q2131-1207, $z_{abs} = 0.4297$

This system was originally reported by Weymann et al. (1979). Bergeron (1986) discovered a galaxy at a redshift 0.430, located 8.6″ away from the quasar, corresponding to an impact parameter of 48.2 kpc. Rao, Turnshek, & Nestor (2006) reported log $N_{HI} = 19.18 \pm 0.03$ for this system based on archival HST UV spectra. Keck HIRES data covering Mg I, Mg II, and Ca II are available for this system. Churchill & Vogt (2001) showed that this system has primarily low-velocity components. They fitted 4 velocity components over a velocity interval of about 52 km/s (with one component dominating by far compared to the others) and reported total column densities of log $N_{MgI} = 12.31$ and log $N_{MgII} = 15.25 \pm 0.52$. However, with the AOD method, they derived log $N_{MgI} = 12.25$ and log $N_{MgII} = 13.47 \pm 0.003$. (We note that there is a large discrepancy between the Voigt profile fitting value and the AOD value of Churchill & Vogt (2001) for N_{MgII}. We believe the AOD value to be more accurate in this case, for the reasons given below.)

Figure 3.14 shows velocity plots from our COS data for the various metal lines in this absorber. Table 3.12 lists the Voigt profile fitting results. Total column densities for various ions in this systems are given in Table 3.17. We detect S II, Si II, and C II clearly in this absorber, with mutually consistent velocity structures. We also constrain the column density of S III, based on the $\lambda 1190.2$ line. Owing to the blend with Si II $\lambda 1190.4$, we can only put an upper limit on the S III column density. Our results indicate that the S abundance is near-solar in this absorber, while both Si and C are considerably sub-solar. This is not an artifact of saturation as S II $\lambda\lambda 1253, 1259$, Si II $\lambda\lambda 1190, 1260$ and C II $\lambda 1334$ all appear to be relatively unsaturated. The low Si and C abundances do not appear to be a result of ionization effects either (see section 4.3). The low abundance of Si relative to S suggests significant depletion. We

note that our value of [Si/H] $= -1.33 \pm 0.04$ is comparable to [Mg/H] $= -1.24 \pm 0.03$ deduced (without ionization correction) from the AOD values of Churchill & Vogt (2001). We also note that the Voigt profile fitting value of N_{MgII} from Churchill & Vogt (2001) would imply [Mg/H] $= +0.54$ dex, higher than even [S/H], which seems unlikely. Higher resolution and higher S/N data may help to resolve this issue.

HST FOS spectra showed the presence of relatively weak C IV and possibly Si IV absorption in this absorber (Churchill et al., 2000). Our data did not cover the N II λ1084, Si III λ1207, or O VI $\lambda\lambda 1032, 1037$ lines. Our data did cover N V $\lambda 1239, 1243$, but these lines were not detected. Overall, this absorber appears to be relatively modestly ionized. The components in the ions detected in our data (C II, Si II, S II) show a spread of ~ 100 km s^{-1}. Compared to the more strongly ionized absorbers toward Q0154+0448 and Q0441+4313, this absorber appears to have a narrower velocity spread in the low ions.

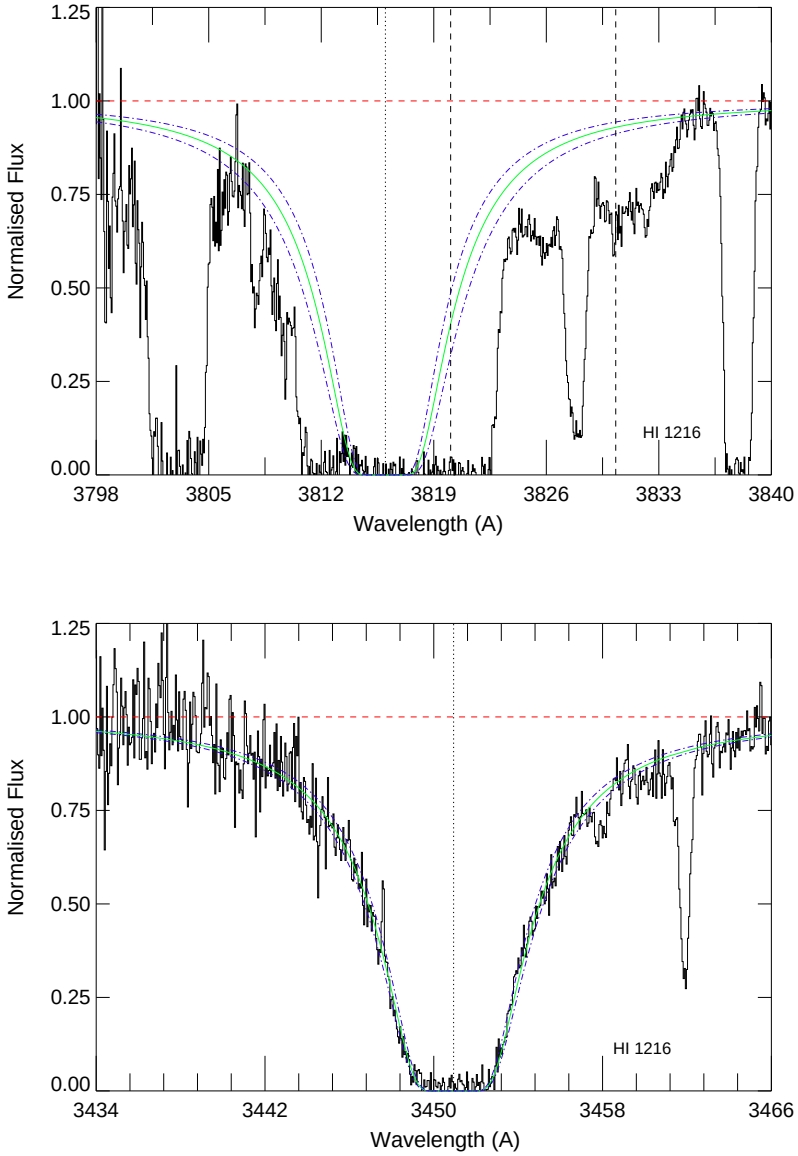

Figure 3.1 **Upper panel:** Lyman-α absorption feature in the $z_{abs} = 2.139$ system towards Q1039-2719. The solid green curve is the Voigt profile for log $N_{HI} = 19.55$. The blue dotted and dashed curves above and below the green curve are Voigt profiles for log $N_{HI} = 19.40$ and 19.70, respectively. The red dashed line represents the normalized continuum while the black dotted line denotes the profile center. The vertical dashed lines denote the locations of the N V $\lambda\lambda$ 1239, 1243 lines from the $z_{abs} = 2.082$ absorber. **Lower panel:** The Lyman-α line in the $z_{abs} = 1.839$ system towards Q1103-2654. The solid green curve shows the Voigt profile for log $N_{HI} = 19.52$ while the blue dotted-dashed curves represent an uncertainty of 0.04.

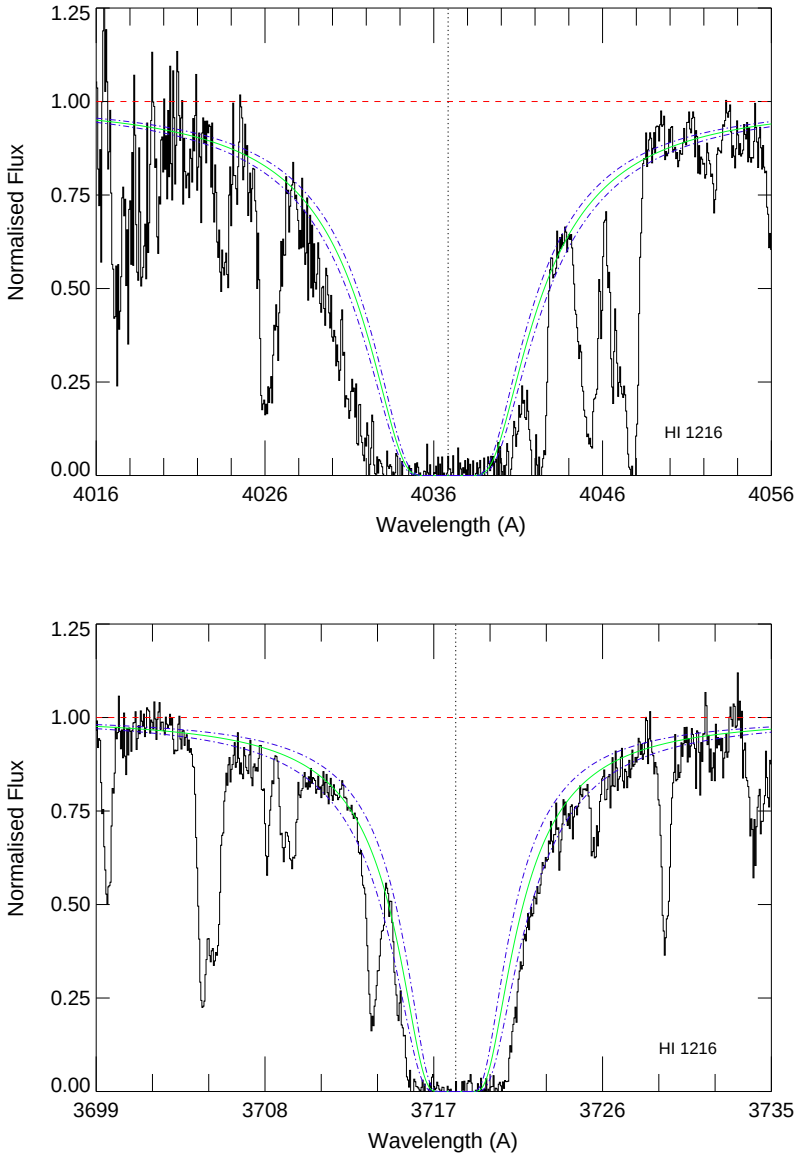

Figure 3.2 **Upper panel**: The Lyman-α line in the $z_{abs} = 2.320$ system towards Q1551+0908. The solid green curve shows the Voigt profile for log $N_{HI} = 19.70$ while the blue dotted-dashed curves represent an uncertainty of 0.05. **Lower panel:** The Lyman-α line in the $z_{abs} = 2.058$ system towards Q2123-0050. The solid green curve shows the Voigt profile for log $N_{HI} = 19.35$ while the blue dotted-dashed curves represent an uncertainty of 0.10.

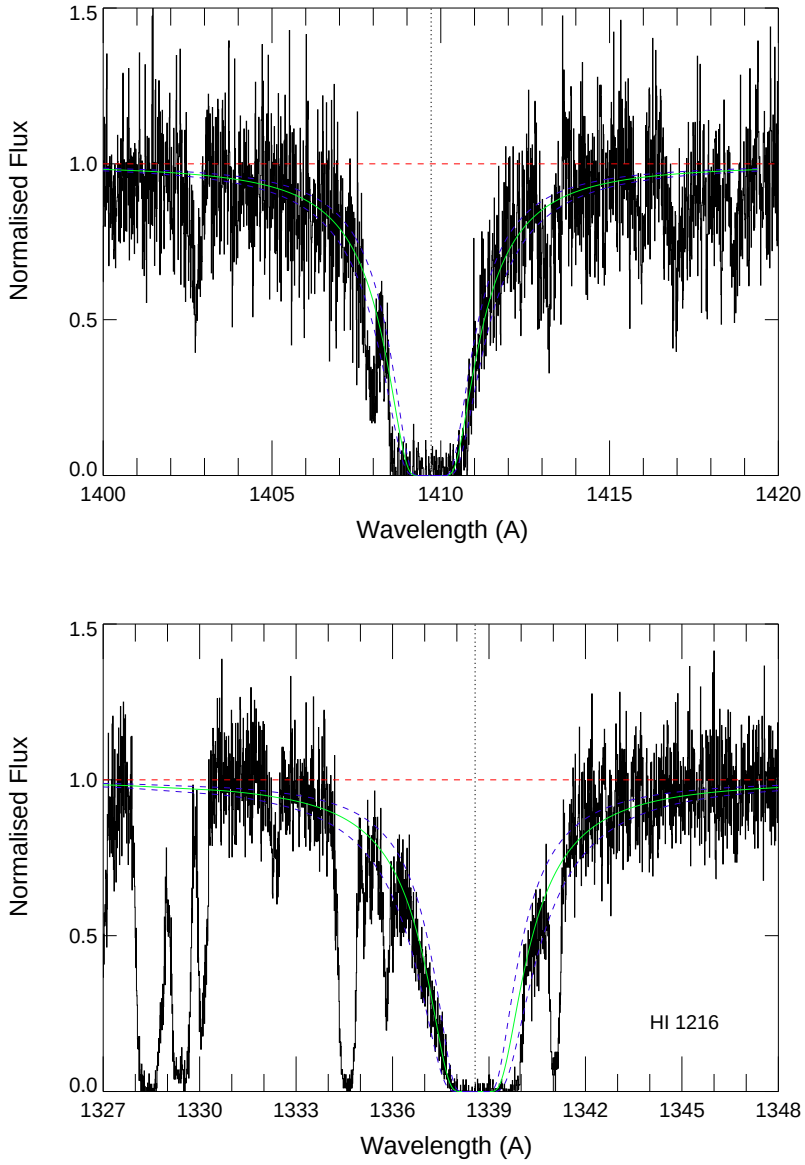

Figure 3.3 **Upper panel**: The Lyman-α line in the $z_{abs} = 0.1602$ system towards Q0154+0448. The solid green curve shows the Voigt profile for log $N_{HI} = 19.48$ while the blue dotted-dashed curves represent an uncertainty of 0.10. **Lower panel:** The Lyman-α line in the $z_{abs} = 0.1012$ system towards Q0441-4313. The solid green curve shows the Voigt profile for log $N_{HI} = 19.63$ while the blue dotted-dashed curves represent an uncertainty of 0.15.

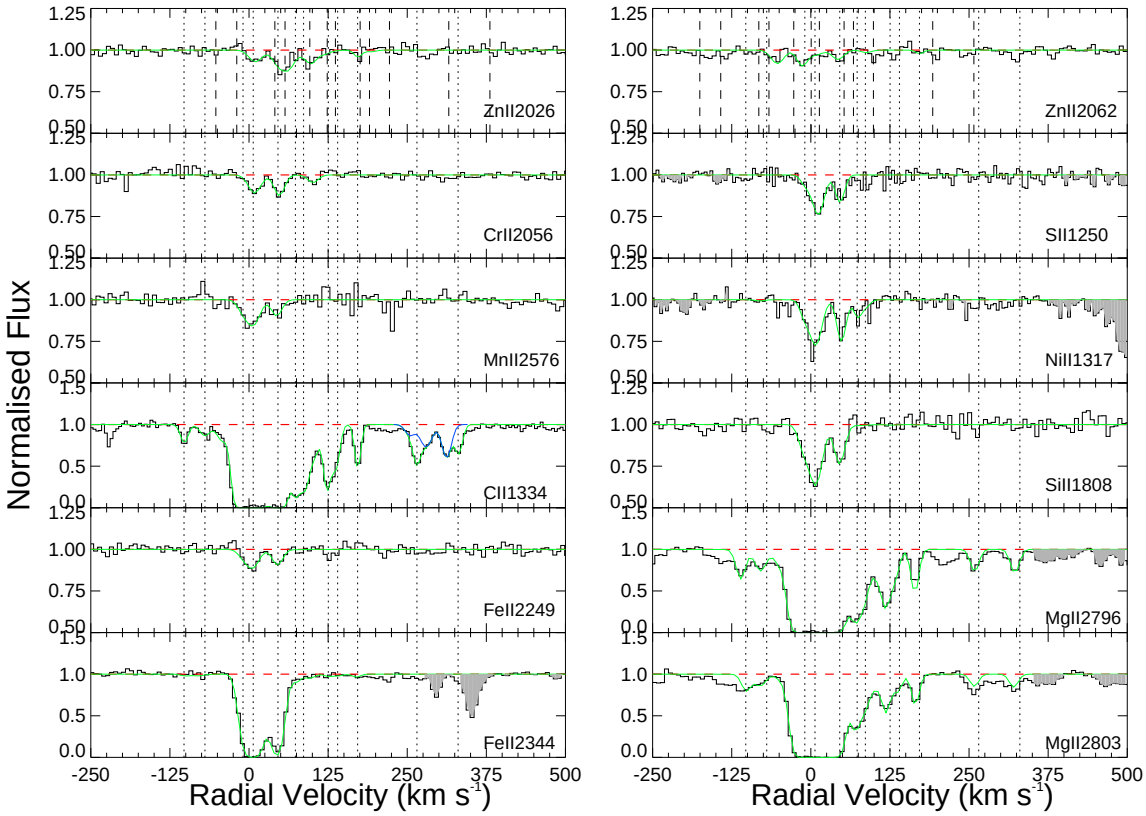

Figure 3.4 Velocity plots for several lines of interest in the z =2.139 system in the spectrum of Q1039-2719. The solid green line indicates the theoretical profile fit to the spectrum, and the dashed red line is the continuum level. The vertical dotted lines indicate the positions of the components that were used in the fit. In the cases of the Zn II $\lambda\lambda$ 2026,2062 lines, which have other lines nearby, the long dashed vertical lines indicate the positions of the components for Mg I (former case), and Cr II (latter case). The regions shaded in gray in some of the panels represent features unrelated to the absorption systems presented here. In the "CII 1334" panel, the solid green line represents the blend between C II λ 1334.5 and C II* λ 1335.7 lines while the solid blue line represents the contribution from C II* λ 1335.7 to this blend.

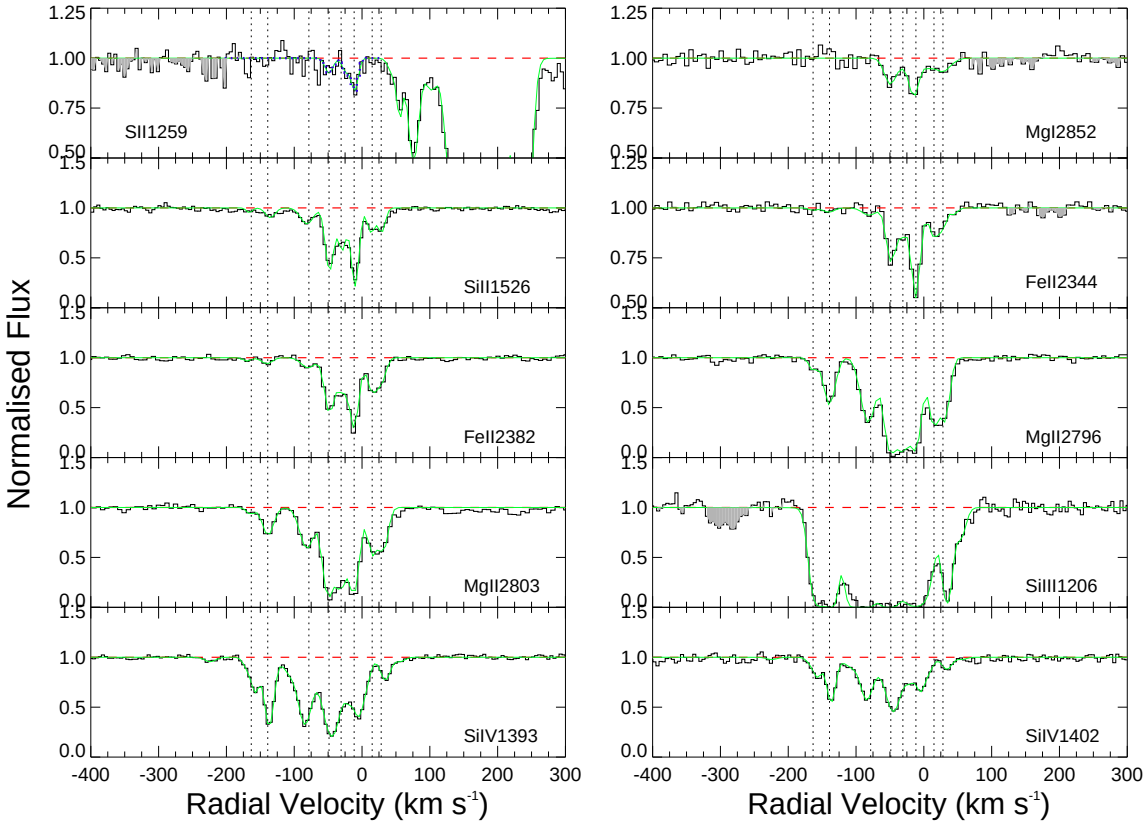

Figure 3.5 Same as Fig. 3.4, but for the z_{abs}=1.839 system in the spectrum of Q1103-2654. In the "SII 1259" panel, the solid green line represents the total contribution from the S II λ 1259.5 and the Si II λ 1260.4 lines. The contribution from S II λ 1259.5 alone is shown with the blue dotted line.

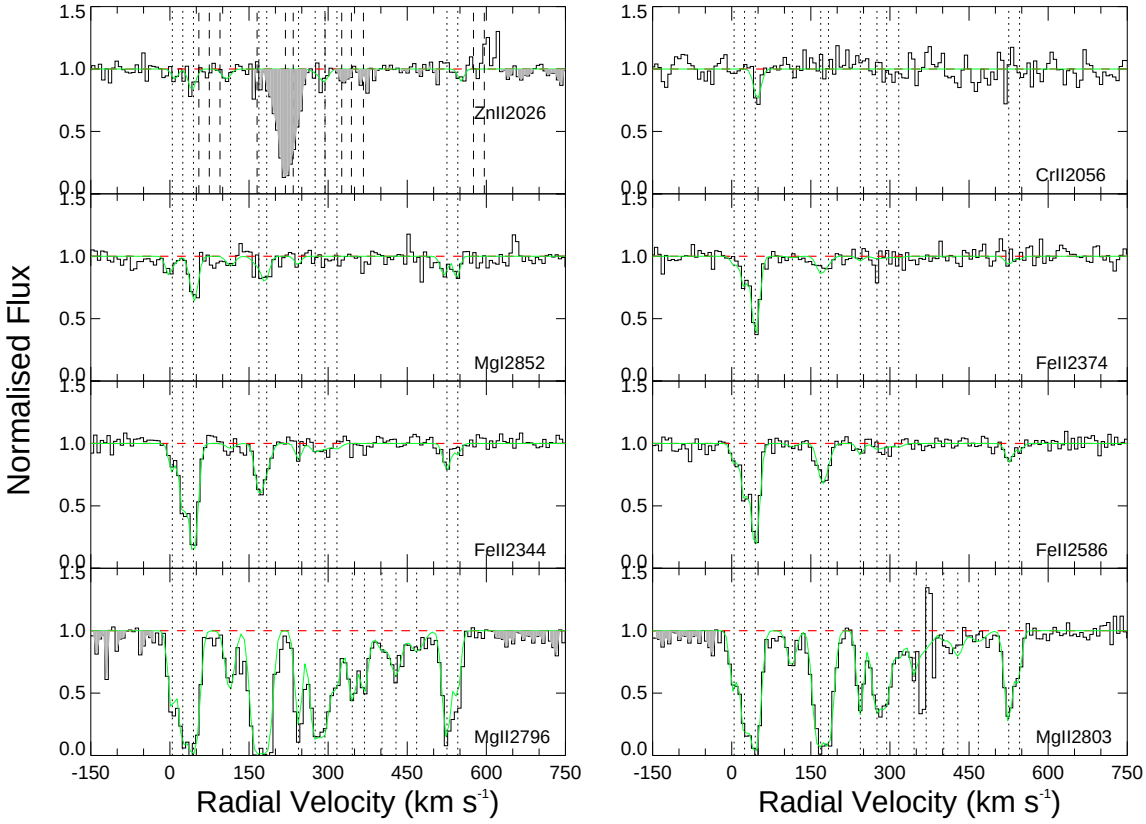

Figure 3.6 Same as Fig. 3.4, but for the z_{abs}=1.762 system in the spectrum of Q1311-0120.

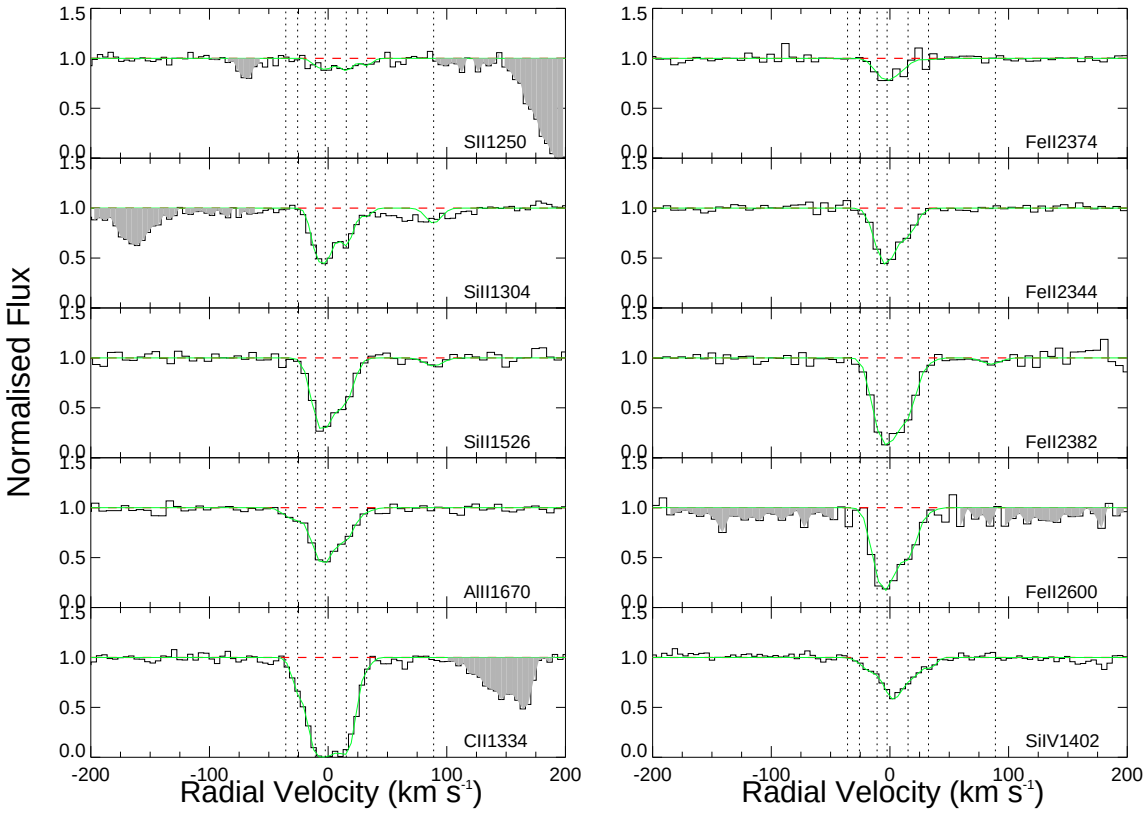

Figure 3.7 Same as Fig. 3.4, but for the z_{abs}= 2.320 system in the spectrum of Q1551+0908.

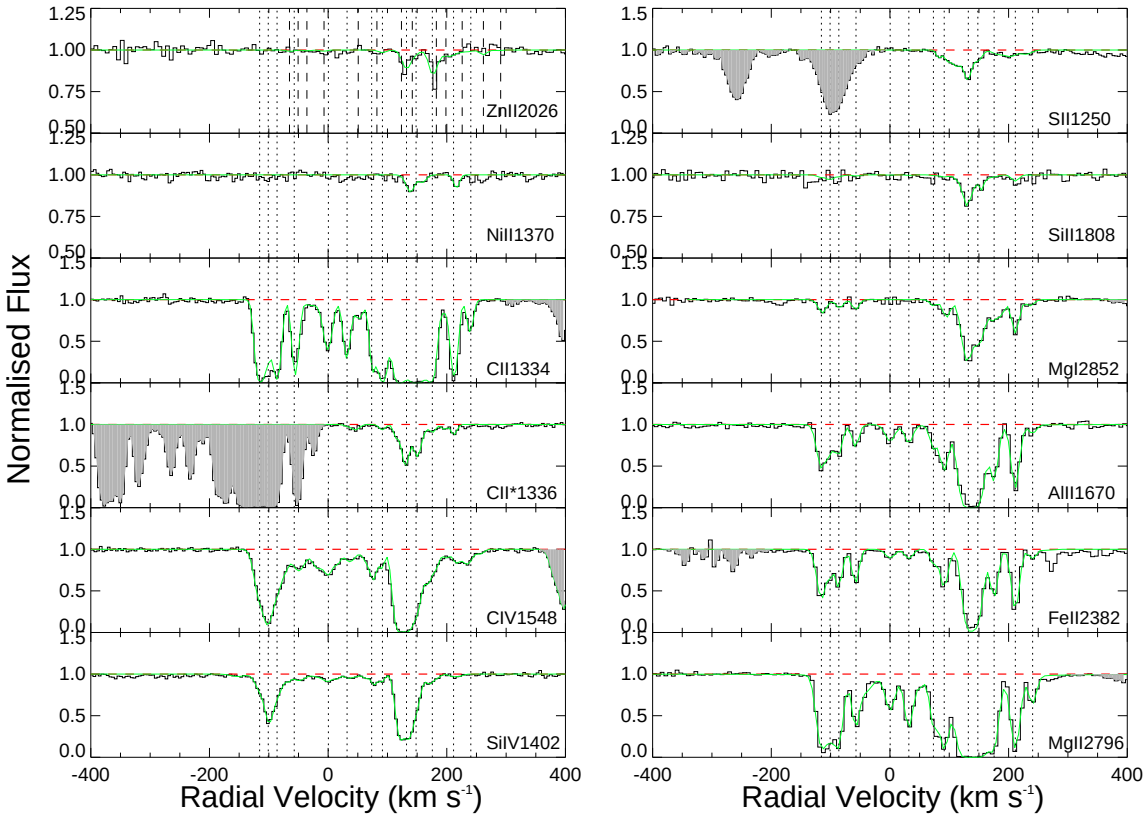

Figure 3.8 Same as Fig. 3.4, but for the z_{abs}=2.058 system in the spectrum of Q2123-0050. In the "CII*1336" panel, the shaded region represents absorption from the C II λ 1334.5 line.

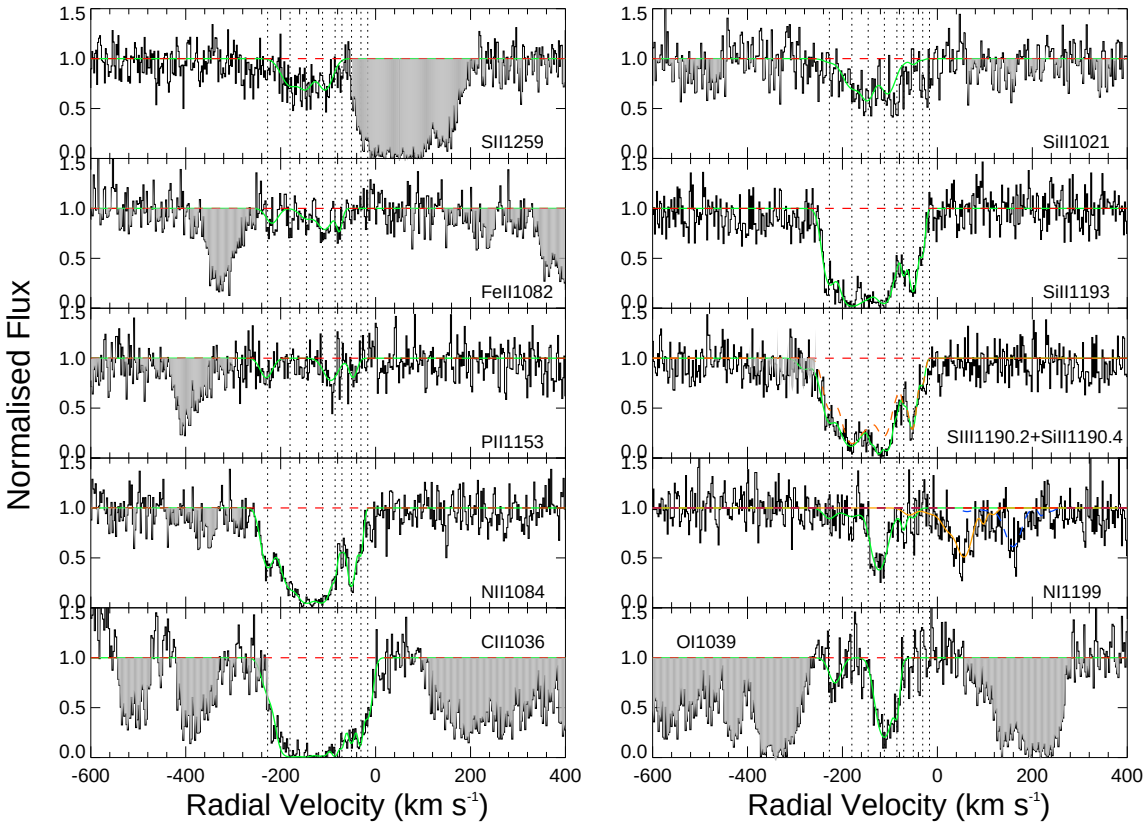

Figure 3.9 Same as Fig. 3.4, but for the z_{abs}=0.1602 system in the spectrum of Q0154+0448. In the S III 1190.2 + Si II 1190.4 panel (with velocity scale shown for Si II λ1190.4), the solid green curve represents the combined contributions from S III λ 1190.2 and Si II λ 1190.4 lines while the contribution from Si II λ 1190.4 alone to this blend, as determined from the Si II λ 1193.3 line, is represented by the dashed orange curve. We obtained an upper limit on the column density of S III by fitting the rest of the blend. The simultaneous fits to the N I $\lambda\lambda$ 1199.6, 1200.2, 1200.7 lines are shown in the N I 1199 panel using solid green, solid orange and dashed blue curves, respectively, and the velocity scale is shown for N I λ 1199.6.

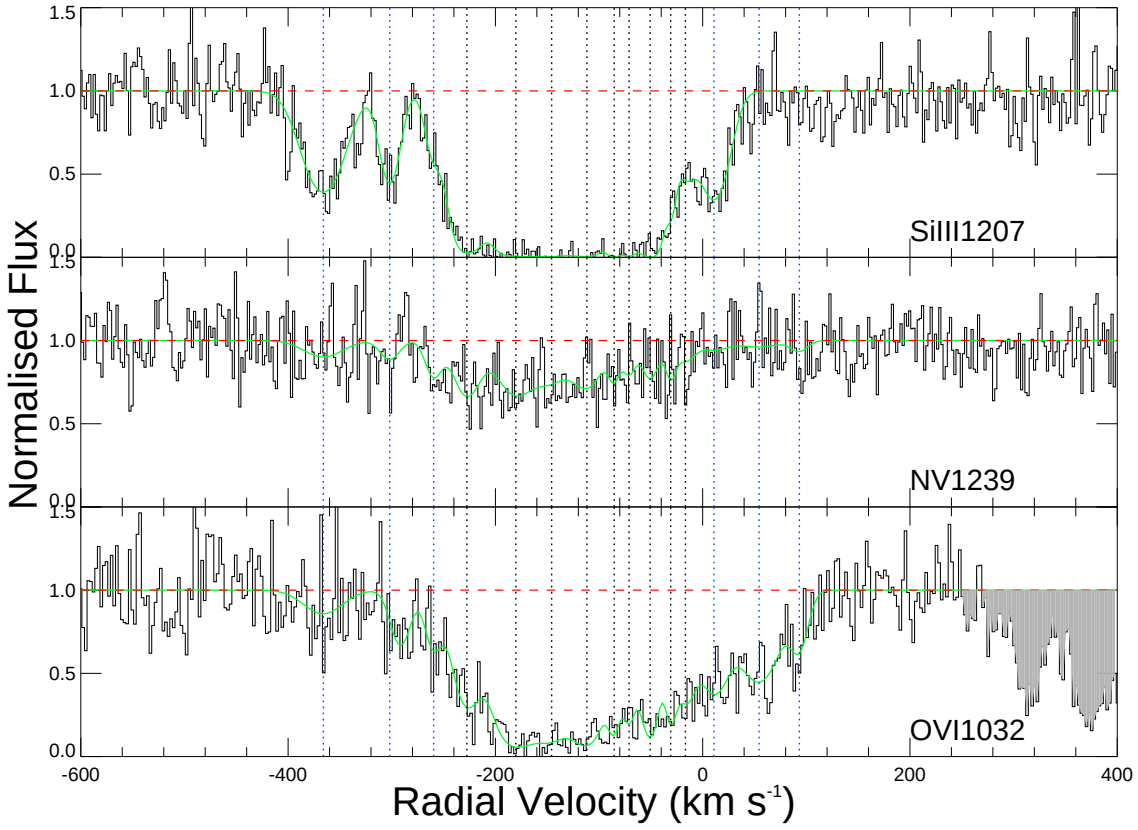

Figure 3.10 Same as Fig 3.9, but for Si III, N V and O VI absorption from the z_{abs}=0.1602 system in the spectrum of Q0154+0448. The absorption components common to these ions and lower ions are indicated by the dotted vertical lines in black, while the components seen in the higher ions only are indicated by the blue vertical dotted lines.

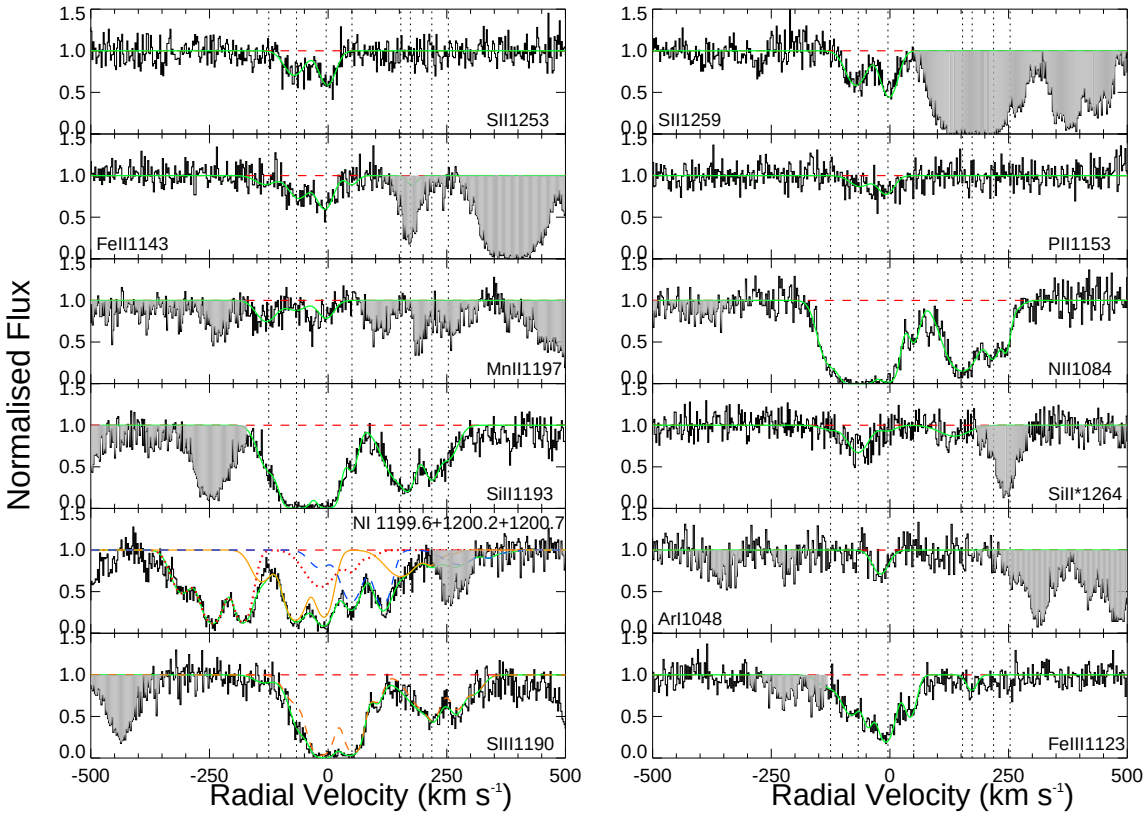

Figure 3.11 Same as Fig. 3.4, but for the z_{abs}=0.1012 system in the spectrum of Q0441-4313. In the N I 1199.6+1200.2+1200.7 panel, the solid green curve represents the total contribution from the N I $\lambda\lambda$ 1199.6, 1200.2, 1200.7 lines. The individual fits to N I λ 1199.6, N I λ 1200.2 and N I λ 1200.7 are shown using the dotted red, solid orange, and dashed blue curves, respectively, and the velocity scale is shown for N I λ 1200.2. The solid green curve in the S III 1190 panel (with velocity scale shown for S III λ1190.2) represents the combined contributions from S III λ 1190.2 and Si II λ 1190.4 lines while the contribution from Si II λ 1190.4 alone to this blend, as determined from the Si II λ 1193.3 line, is represented by the dashed orange curve. We obtained an upper limit on the column density of S III by fitting the rest of the blend.

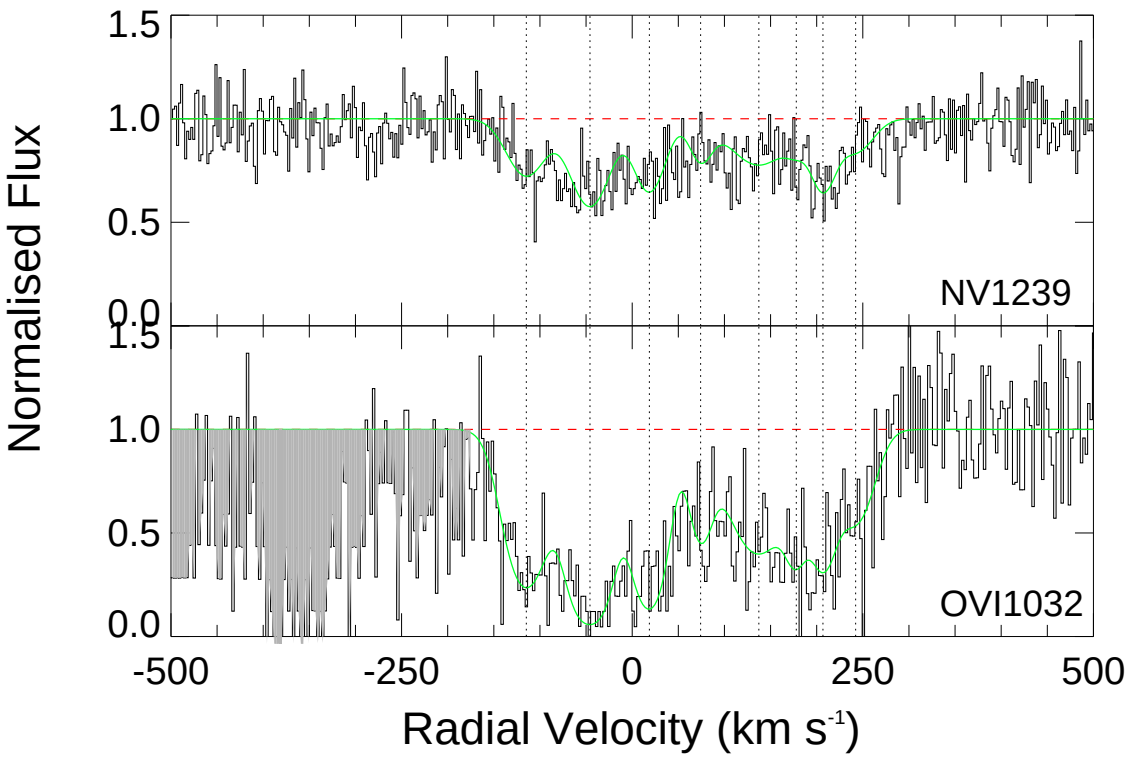

Figure 3.12 Same as Fig. 3.11 but for N V and O VI absorption in the $z = 0.1012$ system in the spectrum of Q0441-4313.

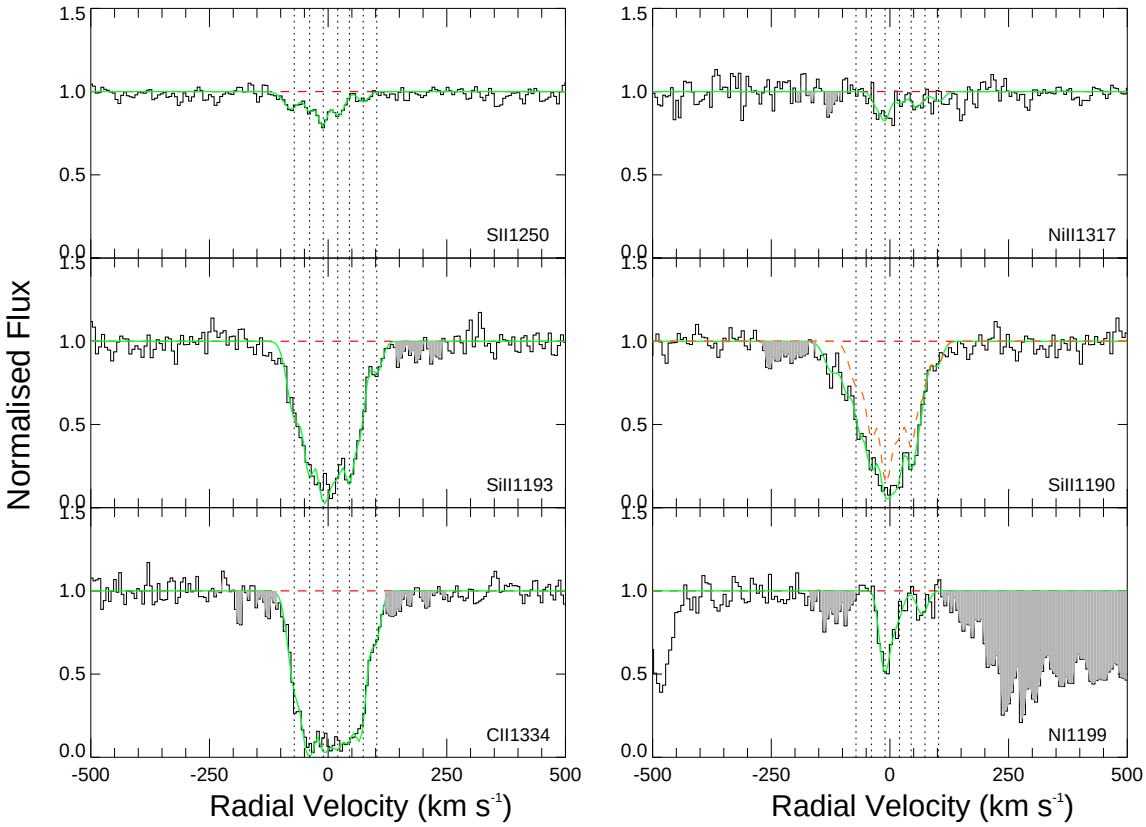

Figure 3.13 Same as Fig. 3.4 but for the absorption in the $z = 0.4744$ system in the spectrum of Q0456-2159.

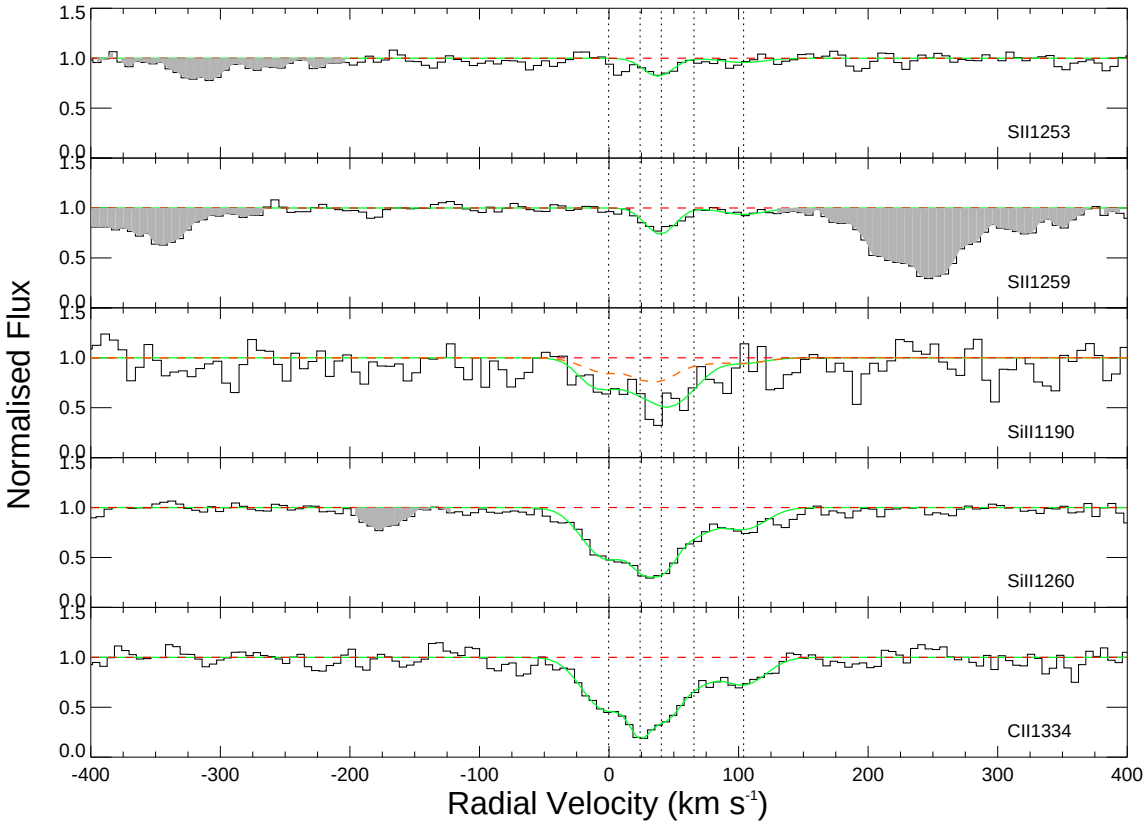

Figure 3.14 Same as Fig. 3.4 but for the absorption in the $z = 0.4297$ system in the spectrum of Q2131-1207. The solid green curve in the Si II 1190 panel (with velocity scale shown for Si II λ1190.4) represents the combined contributions from S III λ 1190.2 and Si II λ 1190.4, while the contribution from Si II λ 1190.4 alone to this blend, as determined from Si II λ 1260.4, is represented by the dashed orange curve. We obtained an upper limit on the column density of S III by fitting the rest of the blend.

Table 3.1 Summary of Observations.

QSO J2000	RA	Dec	Mag	z_{em}	z_{abs}	log N_{HI} cm^{-2}	N_{HI} Reference
Q1039-2719	10:39:21.83	-27:19:16.0	17.4 (m_V)	2.193	2.139	19.55±0.15	1
Q1103-2645	11:03:25.29	-26:45:15.7	16.0 (m_V)	2.145	1.839	19.52±0.04	1
Q1311-0120	13:11:19.26	-01:20:30.9	17.5 (m_V)	2.585	1.762	20.00±0.08	2
Q1551+0908	15:51:03.39	+09:08:49.3	17.9 (m_V)	2.739	2.320	19.70±0.05	1
Q2123-0050	21:23:29.47	-00:50:53.0	16.7 (m_V)	2.262	2.058	19.35±0.10	1
Q0154+0448	01:54:28.00	+04:48:18.3	18.27 (FUV)	0.404	0.1602	19.48±0.10	1
Q0441+4313	04:41:17.30	-43:13:43.00	18.34 (FUV)	0.593	0.1012	19.63±0.15	1
Q0456-2159	04:56:08.90	-21:59:09.00	15.71 (NUV)	0.534	0.4744	19.45±0.02	3
Q2131-1207	21:31:35.30	-12:07:04.80	15.70 (NUV)	0.501	0.4297	19.18±0.03	3

QSO J2000	Instrument	Setup	$\lambda_c/\lambda_{range}$ Å	Exposure Time sec	Epoch
Q1039-2719	MIKE-Magellan	Standard	λ_{range}=3340-9400	7100	2008 March 16
Q1103-2645	MIKE-Magellan	Standard	λ_{range}=3340-9400	3600	2008 March 16
Q1311-0120	MIKE-Magellan	Standard	λ_{range}=3340-9400	8100	2008 March 16
Q1551+0908	MIKE-Magellan	Standard	λ_{range}=3340-9400	6300	2010 May 06
Q2123-0050	MIKE-Magellan	Standard	λ_{range}=3340-9400	4800	2010 May 06
Q0154+0448	COS-HST	G130M	λ_c=1327	13128	2013
Q0441+4313	COS-HST	G130M	λ_c=1291	13680	2013
Q0456-2159	COS-HST	G185M	λ_c=1850	24800	2013
Q2131-1207	COS-HST	G160M	λ_c=1786	23362	2013

N_{HI} References. – (1) This Work, (2) Wolfe et al. (1995), (3) Rao, Turnshek, & Nestor (2006)

Table 3.2 Column densities in individual velocity components for the z=2.139 absorber with log N_{HI}=19.55 in Q1039-2719. Velocities and b_{eff} values are given in units of km s^{-1}. Column densities are in units of cm^{-2} and 1σ errors in column densities are given.

Vel	b_{eff}	Mg I	Mg II	Fe II	Zn II	Ni II	C II*
-103	6.6	-	(1.79±0.57)E+12	(5.28±3.04)E+11	-	-	-
-70	9.5	-	(1.42±0.50)E+12	(6.10±3.21)E+11	-	-	-
-42	10.4	(7.23±2.83)E+11	(1.05±0.65)E+12	-	-	-	-
-9	8.7	(9.03±4.13)E+11	>6.59E+14	(7.37±0.51)E+13	-	(7.22±2.36)E+12	-[a]
10	11.5	(4.90±1.69)E+12	(2.02±0.64)E+15	(2.59±0.35)E+14	(5.31±1.32)E+11	(2.61±0.38)E+13	(1.89±0.27)E+13
46	8.5	(2.47±0.87)E+12	>4.06E+14	(1.85±0.31)E+14	(4.42±1.26)E+11	(1.89±0.33)E+13	(2.02±0.26)E+13
73	6.2	(3.28±2.56)E+11	>8.77E+12	(2.46±0.25)E+12	-	(5.63±1.92)E+12	-
86	8.0	-	>4.60E+12	(1.38±0.25)E+12	(2.23±1.17)E+11	(3.00±1.96)E+12	-
104	9.0	(3.86±2.77)E+11	(1.78±0.61)E+12	-	-	-	-
125	4.4	-	(4.71±1.09)E+12	(6.12±1.66E+11	-	-	-
140	6.4	(3.06±2.04)E+11	(1.91±0.59)E+12	(5.06±1.68)E+11	-	-	-
172	3.6	-	(3.80±0.99)E+12	(7.94±1.55)E+11	(2.46±1.04)E+11	-	-
265	5.6	-	(1.19±0.49)E+12	(4.40±1.41)E+11	-	-	-
330	6.1	-	(1.31±0.50)E=12	(3.4±1.41)E+11	-	-	-

[a]This component is blended with the C II λ 1334.5 line.

Table 3.3 Same as Table 3.2, but for the z_{abs}=1.839 absorber with log N_{HI}=19.52 in Q1103-2645.

Vel	b_{eff}	Mg I	Mg II	Fe II	C II	S II
-163	2.7	-	(4.54±6.74)E+11	(2.48±7.14)E+11	(3.46±2.05)E+12	-
-139	8.2	-	(2.92±0.22)E+12	(6.08±8.34)E+11	(2.12±0.33)E+13	-
-78	11.7	-	(5.86±0.28)E+12	(1.31±0.16)E+12	(4.17±0.34)E+13	-
-67	2.2	-	-	-	(1.19±0.21)E+13	-
-49	5.9	(2.07±0.33)E+11	>3.09E+13	(7.77±0.48)E+12	>3.44E+14	(2.02±1.72)E+13
-31	6.1	(4.46±3.07)E+10	>1.60E+13	(3.52±0.40)E+12	>1.89E+14	(1.82±1.78)E+13
-12	4.5	(2.79±0.34)E+11	>5.45E+13	(1.56±0.08)E+13	>3.34E+14	(3.97±1.88)E+13
4	5.6	(6.67±3.01)E+10	-	-	(1.73±0.11)E+13	-
15	5.8	-	>5.27E+12	(3.60±0.21)E+12	>2.68E+13	-
28	4.7	(1.12±0.37)E+11	(4.33±0.33)E+12	(2.22±0.18)E+12	(2.19±0.13)E+13	-
39	6.0	-	-	-	(1.36±0.09)E+13	-

Table 3.4 Same as Table 3.2, but for the z_{abs}=1.762 absorber with N_{HI}=20.00 in Q1311-0120.

Vel	b_{eff}	Mg I	Mg II	Fe II	Zn II	Cr II
-5	3.8	(1.80±0.63)E+11	>5.93E+012	(6.07±1.40)E+12	-	-
24	3.8	(5.01±5.24)E+10	>4.71E+013	(2.40±0.32)E+13	-	-
45	6.1	(6.25±0.86)E+11	>1.80E+014	(1.04±0.13)E+14	(1.22±0.91)E+012	(8.72±2.44)E+12
115	8.6	(1.16±0.63)E+10	(3.06±0.68)E+12	(1.16±0.29)E+12	(6.28±0.86)E+011	-
169	8.0	(8.87±6.03)E+10	>2.97E+013	(1.44±0.15)E+13	-[a]	-
184	7.3	(3.07±0.70)E+11	>2.72E+013	(4.92±1.09)E+12	-[a]	-
244	3.9	(7.91±5.26)E+10	>1.55E+013	(3.09±0.41)E+12	-[a]	-
275	7.9	-	>9.13E+012	(1.89±0.32)E+12	-	-
294	8.4	-	>8.57E+012	(1.33±0.32)E+12	(7.86±0.93)E+011	-
317	8.5	-	(2.23±0.62)E+12	(1.30±0.31)E+12	-	-
525	6.0	(2.06±0.61)E+11	>1.32E+013	(6.01±1.30)E+12	-	-
546	2.9	(2.28±0.70)E+11	>4.40E+012	(2.01±0.37)E+12	(5.76±0.82)E+011	-

[a]This component is blended with an unidentified feature.

Table 3.5 Same as Table 3.2 but for the z_{abs}=2.320 absorber with log N_{HI}=19.70 in Q1551+0908.

Vel	b_{eff}	Fe II	Si II	C II	Al II	S II
-11	3.1	(4.54±0.94)E+012	(1.46±0.49)E+13	(3.49±2.20)E+14	(6.00±1.13)E+11	-
-2	7.0	(1.99±0.28)E+013	(3.93±0.48)E+13	>2.37E+14	(1.73±0.13)E+12	(9.72±3.28)E+13
15	5.8	(1.10±0.24)E+013	(2.20±0.31)E+13	>1.45E+14	(8.33±0.71)E+11	(1.02±0.28)E+14
32	3.0	(3.21±2.26)E+011	(3.14±1.85)E+12	(2.49±1.04)E+12	(6.56±4.15)E+10	(4.72±2.38)E+13
85	7.2	(6.04±2.57)E+011	(2.95±1.28)E+12	-	-	-

Table 3.6 Same as Table 3.2, but for the z_{abs}=2.058 absorber with log N_{HI}=19.35 in Q2123-0050.

Vel	b_{eff}	Mg I	Fe II	Si II	S II	Zn II	Mn II
-116	5.8	(2.20±0.29)E+11	(8.84±0.45)E+12	(2.69±1.10)E+13	-	-	-
-101	1.4	-	(2.38±0.42)E+12	(4.04±8.30)E+13	-	-	-
-86	5.1	(1.22±0.26)E+11	(5.16±0.38)E+12	(1.87±0.88)E+13	-	-	-
-57	3.3	(1.71±0.43)E+11	(5.11±0.40)E+12	(1.07±0.73)E+13	-	-	-
0	8.2	-	(1.08±0.26)E+12	(3.06±0.56)E+12	-	-	-
32	5.6	-	(1.28±0.24)E+12	(4.87±0.56)E+12	-	-	-
74	2.3	(8.35±2.6)E+10	(2.77±0.45)E+12	(6.76±0.73)E+12	(5.64±1.50)E+13	-	-
91	5.1	(2.94±0.32)E+11	(7.65±0.53)E+12	(2.17±0.11)E+13	(1.19±0.17)E+14	(9.56±9.00)E+010	-
128	6.6	(2.12±0.1E)+12	(3.35±0.30)E+13	(3.71±0.35)E+14	(3.87±0.22)E+14	(7.88±1.11)E+011	(4.17±1.40)E+011
148	7.3	(1.11±0.06)E+12	(1.99±0.09)E+13	(8.51±4.10)E+13	(1.24±0.17)E+14	-	(5.16±1.44)E+011
175	4.4	(3.21±0.35)E+11	(7.71±0.55)E+12	(2.06±0.12)E+13	(5.77±1.90)E+13	(6.48±1.08)E+011	(3.44±1.28)E+011
212	4.1	(7.19±0.59)E+11	(2.69±0.17)E+13	(5.96±0.47)E+13	(1.12±0.10)E+14	-	-
240	4.9	(9.43±2.6)E+10	(9.82±2.50)E+11	(2.36±0.49)E+12	(6.08±1.80)E+13	-	-

Table 3.7 Same as Table 3.2, but for the z_{abs}=0.1602 absorber with log N_{HI}=19.48 in Q0154+0448.

Vel	b_{eff}	N_{SII}	N_{SiII}	N_{SiII^*}	N_{FeII}
-227.6	17.0	...	$2.24 \pm 0.28 \times 10^{13}$	...	$1.36 \pm 1.16 \times 10^{14}$
-180.2	24.7	$2.47 \pm 1.04 \times 10^{14}$	$3.31 \pm 0.73 \times 10^{14}$	...	...
-145.7	19.1	$1.96 \pm 0.98 \times 10^{14}$	$3.70 \pm 0.76 \times 10^{14}$	...	$1.01 \pm 1.21 \times 10^{14}$
-111.7	20.6	$2.47 \pm 0.95 \times 10^{14}$	$3.49 \pm 0.74 \times 10^{14}$	...	$2.40 \pm 1.40 \times 10^{14}$
-85.4	7.0	...	$2.32 \pm 1.78 \times 10^{12}$	$2.64 \pm 0.95 \times 10^{12}$	...
-71.0	7.8	...	$7.94 \pm 1.72 \times 10^{12}$	...	$9.82 \pm 8.99 \times 10^{13}$
-50.7	11.0	...	$2.72 \pm 0.79 \times 10^{13}$	...	...
-30.8	6.5	...	$3.85 \pm 0.97 \times 10^{12}$	...	...

Vel	b_{eff}	N_{CII}	N_{PII}	N_{NII}	N_{NI}	N_{OI}
-227.6	17.0	$> 3.48 \times 10^{13}$	$8.88 \pm 5.37 \times 10^{12}$	$8.35 \pm 2.31 \times 10^{13}$	$8.02 \pm 4.83 \times 10^{12}$	$3.57 \pm 2.50 \times 10^{14}$
-180.2	24.7	$> 6.40 \times 10^{14}$	...	$2.17 \pm 0.59 \times 10^{14}$	$9.40 \pm 8.53 \times 10^{12}$	...
-145.7	19.1	$> 4.14 \times 10^{14}$	...	$2.89 \pm 0.99 \times 10^{14}$	$4.17 \pm 1.85 \times 10^{13}$	...
-111.7	20.6	$> 4.61 \times 10^{14}$	$1.24 \pm 0.61 \times 10^{13}$	$3.35 \pm 1.23 \times 10^{14}$	$1.12 \pm 0.24 \times 10^{14}$	$> 2.35 \times 10^{15}$
-85.4	7.0	$> 1.50 \times 10^{14}$	...	$2.83 \pm 2.22 \times 10^{13}$	...	$3.48 \pm 3.14 \times 10^{14}$
-71.0	7.8	$> 9.81 \times 10^{13}$	...	$2.08 \pm 0.94 \times 10^{13}$	$8.41 \pm 4.04 \times 10^{12}$	...
-50.7	11.0	$> 1.23 \times 10^{14}$	$5.76 \pm 4.38 \times 10^{12}$	$9.79 \pm 3.05 \times 10^{13}$	$5.02 \pm 4.18 \times 10^{12}$	...
-30.8	6.5	$7.07 \pm 6.74 \times 10^{13}$	...	$2.27 \pm 0.82 \times 10^{13}$	...	...
-16.6	12.3	$6.50 \pm 3.43 \times 10^{13}$	..	...	...	...

Table 3.8 Same as Table 3.7, but for higher ions in the z_{abs}=0.1602 absorber with log N_{HI}=19.48 toward Q0154+0448.

Vel	b_{eff}	N_{SIII}	N_{SiIII}	N_{NV}	N_{OVI}
-366.0	25.7	...	$8.25 \pm 0.75 \times 10^{12}$	$9.30 \pm 3.37 \times 10^{12}$	$1.93 \pm 1.06 \times 10^{13}$
-301.9	12.6	...	$3.51 \pm 0.49 \times 10^{12}$	$5.37 \pm 2.41 \times 10^{12}$	$2.55 \pm 0.93 \times 10^{13}$
-259.6	10.7	...	$1.76 \pm 0.40 \times 10^{12}$	$9.13 \pm 2.48 \times 10^{12}$	$2.27 \pm 0.93 \times 10^{13}$
-227.6	17.0	$< 4.51 \times 10^{13}$	$> 2.05 \times 10^{13}$	$2.39 \pm 0.35 \times 10^{13}$	$9.68 \pm 2.24 \times 10^{13}$
-180.2	24.7	$< 1.68 \times 10^{14}$	$> 4.38 \times 10^{13}$	$3.38 \pm 0.44 \times 10^{13}$	$> 3.40 \times 10^{14}$
-145.7	19.1	$< 1.94 \times 10^{14}$	$> 2.86 \times 10^{13}$	$1.52 \pm 0.38 \times 10^{13}$	$> 1.79 \times 10^{14}$
-111.7	20.6	$< 3.46 \times 10^{13}$	$> 3.57 \times 10^{13}$	$2.36 \pm 0.38 \times 10^{13}$	$> 2.66 \times 10^{14}$
-85.4	7.0	$< 1.38 \times 10^{14}$	$> 1.19 \times 10^{13}$	$5.72 \pm 2.23 \times 10^{12}$	$> 5.47 \times 10^{13}$
-71.0	7.8	$< 3.65 \times 10^{14}$	$> 1.27 \times 10^{13}$	$6.04 \pm 2.20 \times 10^{12}$	$5.91 \pm 2.62 \times 10^{13}$
-50.7	11.0	$< 3.36 \times 10^{14}$	$> 2.35 \times 10^{13}$	$1.01 \pm 0.26 \times 10^{13}$	$1.20 \pm 0.38 \times 10^{14}$
-30.8	6.5	$< 4.97 \times 10^{13}$	$> 2.52 \times 10^{12}$	$5.38 \pm 2.15 \times 10^{12}$	$4.35 \pm 2.42 \times 10^{13}$
-16.6	12.3	...	$2.75 \pm 0.58 \times 10^{12}$	$5.51 \pm 2.68 \times 10^{12}$	$6.42 \pm 2.20 \times 10^{13}$
10.9	18.0	...	$6.56 \pm 0.75 \times 10^{12}$	$3.61 \pm 2.86 \times 10^{12}$	$8.29 \pm 2.03 \times 10^{13}$
54.4	26.1	...	...	$3.57 \pm 3.31 \times 10^{12}$	$1.03 \pm 0.19 \times 10^{14}$
93.3	11.0	...	...	$2.52 \pm 2.19 \times 10^{12}$	$2.17 \pm 0.96 \times 10^{13}$

Table 3.9 Same as Table 3.2, but for the z_{abs}=0.1012 absorber with log N_{HI}=19.63 toward Q0441+4313.

Vel	b_{eff}	N_{SII}	N_{SiII}	N_{SiII*}	N_{FeII}
-125.1	28.1	...	$2.02 \pm 0.38 \times 10^{13}$	$8.07 \pm 4.93 \times 10^{11}$	$9.81 \pm 2.11 \times 10^{13}$
-66.7	27.9	$4.81 \pm 0.57 \times 10^{14}$	$> 1.81 \times 10^{14}$	$5.62 \pm 0.64 \times 10^{12}$	$2.73 \pm 0.43 \times 10^{14}$
-4.1	22.4	$5.87 \pm 0.59 \times 10^{14}$	$> 1.22 \times 10^{14}$	$7.99 \pm 4.38 \times 10^{11}$	$3.55 \pm 0.45 \times 10^{14}$
50.2	16.4	...	$1.21 \pm 0.26 \times 10^{13}$	...	$5.84 \pm 0.88 \times 10^{13}$
153.1	42.5	...	$4.70 \pm 0.72 \times 10^{13}$	$2.99 \pm 0.63 \times 10^{12}$	...
173.2	14.8	...	$8.52 \pm 6.18 \times 10^{12}$	...	$5.28 \pm 0.84 \times 10^{13}$
218.4	18.0	...	$1.57 \pm 0.38 \times 10^{13}$	...	...
253.2	25.4	...	$1.27 \pm 0.28 \times 10^{13}$	...	...

v^1	b^1_{eff}	N_{PII}	N_{NII}	N_{ArI}	N_{NI}	N_{MnII}
-125.1	28.1	...	$2.30 \pm 0.22 \times 10^{14}$	...	$8.68 \pm 1.14 \times 10^{13}$	$2.13 \pm 0.94 \times 10^{13}$
-66.7	27.9	$9.33 \pm 2.42 \times 10^{12}$	$1.79 \pm 0.66 \times 10^{15}$	...	$3.53 \pm 0.47 \times 10^{14}$	$9.13 \pm 8.25 \times 10^{12}$
-4.1	22.4	$1.36 \pm 0.24 \times 10^{13}$	$5.04 \pm 0.70 \times 10^{14}$	$1.86 \pm 0.64 \times 10^{13}$	$3.23 \pm 0.52 \times 10^{14}$	$1.41 \pm 0.80 \times 10^{13}$
50.2	16.4	...	$6.38 \pm 0.77 \times 10^{13}$	...	...	...
153.1	42.5	...	$4.45 \pm 0.28 \times 10^{14}$	...	$1.05 \pm 0.16 \times 10^{14}$	...
173.2	14.8	...	$4.33 \pm 1.06 \times 10^{13}$	...	...	...
218.4	18.0	...	$1.04 \pm 0.14 \times 10^{14}$	...	$1.83 \pm 1.47 \times 10^{13}$	$1.55 \pm 0.87 \times 10^{13}$
253.2	25.4	...	$2.31 \pm 1.07 \times 10^{13}$	...	$1.01 \pm 1.18 \times 10^{13}$	$3.02 \pm 1.09 \times 10^{13}$

Table 3.10 Same as Table 3.9, but for higher ions in the z_{abs}=0.1012 absorber with log N_{HI}=19.63 toward Q0441+4313.

Vel	b_{eff}	N_{SIII}	N_{FeIII}	N_{NV}	N_{OVI}
-125.1	28.1	$< 6.64 \times 10^{13}$	$4.47 \pm 1.77 \times 10^{13}$	$3.17 \pm 0.40 \times 10^{13}$	$1.99 \pm 0.44 \times 10^{14}$
-66.7	27.9	$< 3.13 \times 10^{14}$	$2.02 \pm 0.20 \times 10^{14}$	...	...
-45.4	12.8	...	$1.09 \pm 0.20 \times 10^{14}$	$5.34 \pm 0.48 \times 10^{13}$	$3.92 \pm 1.06 \times 10^{14}$
-4.1	22.4	$< 1.23 \times 10^{15}$	$4.09 \pm 0.36 \times 10^{14}$	...	...
18.6	22.4	...	...	$3.40 \pm 0.39 \times 10^{13}$	$2.23 \pm 0.58 \times 10^{14}$
50.2	16.4	$< 5.99 \times 10^{14}$	$1.29 \pm 0.15 \times 10^{14}$	...	...
74.2	16.4	...	...	$1.22 \pm 0.29 \times 10^{13}$	$5.64 \pm 2.14 \times 10^{13}$
137.3	42.5	...	...	$3.73 \pm 0.51 \times 10^{13}$	$1.92 \pm 0.41 \times 10^{14}$
153.1	42.5	$< 1.10 \times 10^{14}$	...	...	...
173.2	14.8	...	$3.41 \pm 0.96 \times 10^{13}$	$4.68 \pm 3.09 \times 10^{12}$	$5.00 \pm 3.17 \times 10^{13}$
218.4	18.0	...	...	$2.49 \pm 0.38 \times 10^{13}$	$8.97 \pm 3.42 \times 10^{13}$
253.2	25.4	$< 9.95 \times 10^{13}$	...	$1.55 \pm 0.36 \times 10^{13}$	$7.54 \pm 2.41 \times 10^{13}$

Table 3.11 Same as Table 3.2, but for the $z = 0.4744$ sub-DLA toward Q0456-2159.

Vel	b_{eff}	N_{SII}	N_{SiII}	N_{CII}
-71.5	20.8	$2.41 \pm 0.35 \times 10^{14}$	$> 1.41 \times 10^{13}$	$> 8.98 \times 10^{13}$
-39.0	10.9	$1.59 \pm 0.28 \times 10^{14}$	$> 2.08 \times 10^{13}$	$> 2.73 \times 10^{14}$
-10.3	11.8	$3.14 \pm 0.32 \times 10^{14}$	$> 5.21 \times 10^{13}$	$> 1.83 \times 10^{14}$
20.2	16.0	$2.75 \pm 0.34 \times 10^{14}$	$> 2.92 \times 10^{13}$	$> 2.09 \times 10^{14}$
44.8	8.2	...	$> 1.86 \times 10^{13}$	$> 7.58 \times 10^{13}$
73.9	13.8	$9.77 \pm 2.82 \times 10^{13}$	$> 1.34 \times 10^{13}$	$> 1.41 \times 10^{14}$
102.5	14.3	...	$> 3.35 \times 10^{12}$	$> 2.37 \times 10^{13}$

Vel	b_{eff}	N_{NI}	N_{NiII}	N_{SIII}
-71.5	20.8	...	...	$< 1.10 \times 10^{14}$
-39.0	10.9	...	$6.51 \pm 3.44 \times 10^{12}$	$< 7.46 \times 10^{13}$
-10.3	11.8	$3.92 \pm 2.02 \times 10^{13}$	$1.63 \pm 0.39 \times 10^{13}$	$< 1.42 \times 10^{14}$
20.2	16.0	$1.64 \pm 1.56 \times 10^{13}$	$8.53 \pm 3.71 \times 10^{12}$	$< 2.74 \times 10^{14}$
44.8	8.2	...	$4.46 \pm 3.64 \times 10^{12}$	$< 2.01 \times 10^{14}$
73.9	13.8	...	$6.24 \pm 4.29 \times 10^{12}$	$< 5.15 \times 10^{14}$
102.5	14.3	...	$6.48 \pm 3.45 \times 10^{12}$	$< 1.96 \times 10^{14}$

Table 3.12 Same as Table 3.2, but for the $z = 0.4297$ sub-DLA toward Q2131-1207.

Vel	b_{eff}	N_{SII}	N_{SiII}	N_{CII}	N_{SIII}
-0.3	23.6	...	$8.26 \pm 0.58 \times 10^{12}$	$7.47 \pm 0.73 \times 10^{13}$	...
24.0	8.2	...	$2.29 \pm 0.65 \times 10^{12}$	$5.23 \pm 1.30 \times 10^{13}$	...
40.4	13.7	$1.52 \pm 0.28 \times 10^{14}$	$7.02 \pm 0.77 \times 10^{12}$	$5.33 \pm 0.85 \times 10^{13}$	$< 6.86 \times 10^{13}$
65.5	17.7	...	$2.57 \pm 0.40 \times 10^{12}$	$2.26 \pm 0.52 \times 10^{13}$	$< 7.68 \times 10^{13}$
103.9	22.1	$4.98 \pm 2.95 \times 10^{13}$	$2.59 \pm 0.37 \times 10^{12}$	$2.91 \pm 0.45 \times 10^{13}$	$< 2.55 \times 10^{14}$

Table 3.13 Total column densities for the absorbers in the MIKE sample. Cells with "..." entries represent undetermined column densities.

QSO	z_{abs}	log N_{HI} cm^{-2}	log N_{MgI} cm^{-2}	log N_{MgII} cm^{-2}	log N_{AlII} cm^{-2}	log N_{AlIII} cm^{-2}	log N_{CII} cm^{-2}	log N_{CII*} cm^{-2}	log N_{CIV} cm^{-2}	log N_{SII} cm^{-2}
Q1039-2719	2.139	19.55±0.15	13.02±0.09	>15.49	>13.88	13.53±0.02	>15.78	>13.35	...	14.76±0.03
AOD			12.98±0.01	>15.16	>13.66	13.52±0.01	>15.08			14.75±0.04
Q1103-2645	1.839	19.52±0.04	11.86±0.05	>14.08	...	12.74±0.07	>15.01	>12.93	...	13.89±0.17
AOD			11.84±0.05	>13.79		12.64±0.06	>14.69	>12.30		13.73±0.14
Q1311-0120	1.762	20.00±0.08	12.27±0.04	>14.55	>13.03	<11.85	...	...	...	...
AOD			12.25±0.14	>14.15	>12.90					
Q1551+0908	2.320	19.70±0.05	...	...	12.55±0.02	12.05±0.08	>14.87	<12.17	13.81±0.02	14.43±0.09
AOD					12.53±0.01	12.14±0.13	>14.51		13.77±0.03	14.47±0.07
Q2123-0050	2.058	19.35±0.10	12.74±0.01	>14.50	>15.24	13.45±0.07	>15.99	>13.82	>14.62	15.05±0.02
AOD			12.72±0.01	>14.27	>13.47	13.14±0.02	>15.16	>13.80	>14.57	15.01±0.04

QSO	z_{abs}	log N_{HI} cm^{-2}	log N_{SiII} cm^{-2}	log N_{SiIII} cm^{-2}	log N_{SiIV} cm^{-2}	log N_{CrII} cm^{-2}	log N_{MnII} cm^{-2}	log N_{NiII} cm^{-2}	log N_{FeII} cm^{-2}	log N_{ZnII} cm^{-2}
Q1039-2719	2.139	19.55±0.15	15.30±0.03	>14.48	>14.50	13.07±0.04	12.48±0.06	13.79±0.04	14.72±0.04	12.16±0.07
AOD			15.31±0.05	>14.30	>14.50	12.99±0.07	12.54±0.06	13.75±0.07	14.74±0.02	12.40±0.08
Q1103-2645	1.839	19.52±0.04	14.07±0.02	>14.64	13.84±0.01	<11.91	<12.46	<12.34	13.54±0.02	<11.33
AOD			14.00±0.01	>14.12	13.82±0.01		<12.37		13.52±0.04	
Q1311-0120	1.762	20.00±0.08	>14.38	...	...	12.94±0.12	<11.65	...	14.23±0.35	>12.57
AOD			>14.26			12.87±0.09			14.09±0.06	>12.75
Q1551+0908	2.320	19.70±0.05	13.91±0.04		13.34±0.01	<12.15	<11.40	13.01±0.32	13.56±0.05	<11.38
AOD			13.97±0.02	>13.69	13.31±0.02			13.11±0.04	13.57±0.07	
Q2123-0050	2.058	19.35±0.10	14.89±0.06	>14.72	>13.99	<11.90	12.11±0.08	13.12±0.08	14.09±0.01	12.23±0.06
AOD			14.85±0.06	>14.15	>13.95		12.04±0.06	13.01±0.10	14.01±0.01	12.44±0.06

Table 3.14 Total Column Densities for the $z = 0.1602$ absorber toward Q0154+0448.

Ion	log N^{fit}	log N^{AOD}
H I	19.48 ± 0.10	...
S II	14.84 ± 0.11	14.81 ± 0.07
S III	< 15.12	...
Si II	15.05 ± 0.05	15.13 ± 0.07
Si II*	12.42 ± 0.16	12.41 ± 0.14
Si III	> 14.31	> 14.27
Fe II	14.76 ± 0.18	14.77 ± 0.15
Mn II	< 12.58	...
C II	> 15.31	> 15.28
P II	13.43 ± 0.15	13.60 ± 0.16
N I	14.27 ± 0.08	...
N II	15.04 ± 0.07	15.04 ± 0.01
N V	14.21 ± 0.03	14.25 ± 0.13
O I	> 15.48	> 15.51
O VI	> 15.18	> 15.20

Table 3.15 Total Column Densities for the $z = 0.1012$ absorber toward Q0441+4313.

Ion	log N^{fit}	log N^{AOD}
H I	19.63 ± 0.15	...
S II	15.03 ± 0.03	15.02 ± 0.06
S III	< 15.38	...
Si II	> 14.62	> 14.54
Si II*	13.01 ± 0.05	13.04 ± 0.12
Fe II	14.92 ± 0.03	14.83 ± 0.06
Fe III	14.97 ± 0.02	15.05 ± 0.04
Mn II	13.65 ± 0.15	13.75 ± 0.11
P II	13.36 ± 0.06	13.43 ± 0.14
Ar I	13.27 ± 0.15	13.19 ± 0.13
N I	14.95 ± 0.04	...
N II	> 15.51	> 15.41
N V	14.33 ± 0.02	14.34 ± 0.06
O VI	15.11 ± 0.05	15.14 ± 0.03

Table 3.16 Total Column Densities for the $z = 0.4744$ absorber toward Q0456-2159.

Ion	log N^{fit}	log N^{AOD}
H I	19.45 ± 0.02	...
S II	15.04 ± 0.03	14.98 ± 0.05
S III	< 15.18	...
Si II	> 14.18	> 14.13
Si II*	< 11.86	
C II	> 15.00	> 14.92
C II*	< 12.57	
N I	13.75 ± 0.20	13.75 ± 0.04
Ni II	13.69 ± 0.08	13.63 ± 0.07

Table 3.17 Total Column Densities for the $z = 0.4297$ Absorber toward Q2131-1207.

Ion	log N^{fit}	log N^{AOD}
H I	19.18 ± 0.03	...
S II	14.31 ± 0.09	14.34 ± 0.10
S III	< 14.60	...
Si II	13.36 ± 0.02	13.35 ± 0.01
C II	14.37 ± 0.03	14.36 ± 0.02
C II*	< 12.85	...

Table 3.18 Rest-frame equivalent widths of key metal lines from the MIKE sample. Measured values and 1σ errors are in mÅ units.

QSO	z_{abs}	Mg I 2852	Mg II 2796	Mg II 2803	Al II 1670	Al III 1854	Al III 1862	S II 1250	S II 1253	S II 1259	Si II 1526	Si II 1808
Q1039-2719	2.139	749±11	1527±54	1365±66	572±14	<933[b]	212±8	39±4	<111[b]	103±3	529±16	108±12
Q1103-2645	1.839	86±10	1034±10	768±12	...	67±10	...	6±3	<42[b]	12±4	213±5	<5
Q1311-0120	1.762	213±73	2230±53	1601±53	...	<12	<12	...	...	...	>306[a]	...
Q1551+0908	2.320	...	...	...	114±3	23±7	...	21±3	...	...	120±10	5±2
Q2123-0050	2.058	527±16	1946±6	1655±6	654±10	197±12	103±13	70±6	196±10	...	546±9	40±6

QSO	z_{abs}	Cr II 2056	Mn II 2576	Mn II 2594	Mn II 2606	Fe II 2344	Fe II 2374	Fe II 2382	Fe II 2586	Fe II 2600	Zn II[c] 2026	Zn II[d] 2062
Q1039-2719	2.139	36±6	70±9	...	<113[b]	568±5	414±15	747±15	575±13	1478±244	48±12	23±4
Q1103-2645	1.839	<3	<46[b]	<21[b]	<6	139±6	56±12	327±9	124±10	303±7	<4	<3
Q1311-0120	1.762	25±5	<10	<93[b]	...	384±49	154±25	766±53	305±53	<1281[b]	>94	>26
Q1551+0908	2.320	<6	<5	...	...	129±5	44±4	250±10	193±9	273±7	<4	<4
Q2123-0050	2.058	<3	23±3	<4	15±6	445±8	221±72	862±216	328±20	772±16	47±6	21±18

[a]This line is partially blended with Lyα forest lines. [b]This line is blended with another feature. [c]This line is blended with Mg I λ 2026. Therefore, the measured value represents the total equivalent width of the blend. However, the Mg I contribution is judged to be insignificant in all cases. [d]Since this line is blended with the Cr II λ 2062 line, the measured value represents the total equivalent width of the blended feature.

Table 3.19 Rest-frame equivalent widths of key metal lines from the HST COS sample. Measured values and 1σ errors are in mÅ units.

QSO	z_{abs}	C II 1036	C II 1334	N I 1199	N II 1084	N V 1239	N V 1243	O I 1039	O VI 1032	Ar I 1048
Q0154+0448	0.1602	677 ± 36	...	...	569 ± 14	301 ± 98	174 ± 87	171 ± 57	929 ± 128	...
Q0441+4313	0.1012	...	...	...	1094 ± 23	388 ± 55	...	...	888 ± 52	33 ± 10
Q0456-2159	0.4744	...	727 ± 13	78 ± 8	...	...	...	...	...	...
Q2131-1207	0.4297	...	310 ± 13	...	...	...	...	...	...	...

QSO	z_{abs}	Si II 1021	Si II 1193	Si II 1260	Si II* 1265	Si III 1207	P II 1153	S II 1250	S II 1253	S II 1259
Q0154+0448	0.1602	162 ± 24	690 ± 12	838 ± 15	30 ± 11	1192 ± 28	97 ± 38	...	...	122 ± 19
Q0441+4313	0.1012	...	1039 ± 30	1279 ± 22	136 ± 42	...	67 ± 22	77 ± 18	131 ± 16	177 ± 15
Q0456-2159	0.4744	...	534 ± 14	747 ± 7	...	...	...	68 ± 8	...	111 ± 4
Q2131-1207	0.4297	...	...	266 ± 6	...	...	...	...	32 ± 7	36 ± 6

QSO	z_{abs}	Mn II 1197	Fe II 1082	Fe II 1097	Fe II 1112	Fe II 1125	Fe II 1143	Fe II 1145	Fe III 1123	Ni II 1317
Q0154+0448	0.1602	< 10	65 ± 23	...	137 ± 13	...	...	...	...	
Q0441+4313	0.1012	127 ± 35	...	...	...	136 ± 30	124 ± 15	713 ± 23	490 ± 51	...
Q0456-2159	0.4744	...	...	...	...	...	...	...	...	47 ± 8
Q2131-1207	0.4297	...	...	...	...	...	...	...	...	...

Table 3.20 Observed element abundances relative to Solar and abundance ratios for the systems in the MIKE sample. Abundance estimates are based on the dominant metal ionization state and H I. The solar value of the ratios are given in the first row.

QSO	z_{abs}	log N_{HI}	[Zn/H]	[S/H]	[Fe/H]	[S/Zn]	[Zn/Fe]	[Si/Fe]	[Cr/Fe]
log $(X/Y)_\odot$			−7.44	−4.88	−4.50	+2.56	−2.94	+0.01	−1.86
Q1039-2719	2.139	19.55±0.15	−0.02±0.17	+0.02±0.15	−0.30±0.16	+0.04±0.08	+0.28±0.08	+0.51±0.05	+0.17±0.05
Q1103-2645	1.839	19.52±0.04	<−0.82	−0.82±0.19	−1.45±0.04	>+0.01	<+0.62	+0.46±0.03	<+0.19
Q1311-0120	1.762	20.00±0.08	>−0.06	...	−1.24±0.09	...	>+1.18	>+0.08	+0.53±0.13
Q1551+0908	2.320	19.70±0.05	<−0.95	−0.46±0.10	−1.61±0.07	>+0.49	<+0.66	+0.28±0.06	<+0.41
Q2123-0050	2.058	19.35±0.10	+0.25±0.12	+0.51±0.10	−0.73±0.10	+0.26±0.06	+0.98±0.06	+0.73±0.06	<−0.38

QSO	z_{abs}	log N_{HI}	[Mn/Fe]	Al III/Al II[a]	Fe II/Al III[a]	Mg II/Al III[a]	Mg II/Mg I[a]	Si III/Si II[a]	Si IV/Si II[a]
log $(X/Y)_\odot$			−2.07						
Q1039-2719	2.139	19.55±0.15	−0.27±0.07	<−0.35	+1.20±0.04	>+1.97	>+2.48	>−1.01	>−0.81
Q1103-2645	1.839	19.52±0.04	<+0.89	...	+0.90±0.06	>+1.44	>+2.22	>+0.05	−0.23±0.02
Q1311-0120	1.762	20.00±0.08	<−0.61	<−1.05	>+2.38	>+2.70	>+2.28	...	...
Q1551+0908	2.320	19.70±0.05	<−0.19	−0.41±0.14	+1.42±0.14	...	...	>−0.23	−0.58±0.04
Q2123-0050	2.058	19.35±0.10	−0.01±0.08	<−0.01	+0.64±0.07	>+0.82	>+1.53	>−0.73	>−0.89

[a]Ratio of column densities.

Table 3.21 Observed element abundances relative to Solar for the systems in the HST COS sample. Abundance estimates are based on the dominant metal ionization state and H I.

QSO	z_{abs}	log N_{HI} (cm^{-2})	Element	[X/H]
Q0154+0448	0.1602	19.48 ± 0.10	S	0.22 ± 0.15
			Si	0.06 ± 0.11
			Fe	-0.17 ± 0.21
			P	0.59 ± 0.18
			C	> -0.56
			N	-0.99 ± 0.13
			O	> -0.66
Q0441+4313	0.1012	19.63 ± 0.15	S	0.26 ± 0.15
			Si	> -0.52
			Fe	-0.16 ± 0.15
			Mn	0.63 ± 0.21
			P	0.37 ± 0.16
			Ar	-0.54 ± 0.21
			N	-0.46 ± 0.16
Q0456-2159	0.4744	19.45 ± 0.03	S	0.45 ± 0.04
			Si	> -0.78
			C	> -0.84
			N	-1.48 ± 0.20
			Ni	0.01 ± 0.08
Q2131-1207	0.4297	19.18 ± 0.03	S	-0.01 ± 0.09
			Si	-1.33 ± 0.04
			C	-1.20 ± 0.04

CHAPTER 4

Discussion

The results from our observations presented in Chapter 3 are discussed here in the context of sub-DLA properties in general. Combining our data with those from the literature, we shall explore the nature of sub-DLAs in contrast with the DLAs, and discuss the implications of the observed trends for understanding the chemical and kinematic properties of the galaxies traced by these systems.

4.1 Abundance Patterns

As shown in Tables 3.20 and 3.21, for most of the sub-DLAs in our observed sample, the measured abundance of the primary metallicity indicator Zn or S was found to be near-solar or super-solar. Zn was detected in three of the sub-DLA absorbers in our high-z sample, and for the rest of the systems we place 3σ upper limits on the Zn abundance. All of the absorbers, for which Zn was detected, were found to be metal-rich ([Zn/H] $= -0.02$ for Q1039-2719 at $z_{abs} = 2.139$; > -0.06 for Q1311-0120 at $z_{abs} = 1.762$ and $+0.25$ for Q2123-0050 at $z_{abs} = 2.058$). These absorbers are among the most metal-rich sub-DLAs at $z \gtrsim 1$ and are the only near-solar or super-solar metallicity sub-DLA QSO absorbers at $z \gtrsim 2$. The Zn abundance upper limits for Q1103-2645 ($z_{abs} = 1.839$) and Q1551+0908 ($z_{abs} = 2.320$) place their metallicities

at < -0.82 and < -0.95, respectively. Sulphur was detected in these two systems and their metallicities based on S abundances are -0.82 (for Q1103-2645) and -0.46 (for Q1551+0908). All of the absorbers in our low-z sample were found to be metal-rich based on their S abundances. With [S/H] = 0.45, the sub-DLA at $z = 0.4744$ towards Q0456-2159 is the highest metallicity quasar absorption line system discovered so far at $z < 0.6$. The systems towards Q0441+4313, Q0154+0448 and Q2131-1207 (at $z =$ 0.1012, 0.1602, 0.4297; with [S/H] = 0.26, 0.22, -0.01, respectively), along with the one towards Q0456-2159 are the only near-solar or super-solar metallicity sub-DLAs in this redshift regime.

In addition to the metallicities, abundance ratios such as [Fe/Zn], [Mn/Fe], [S/Zn], [N/S] have been determined from the column densities of various elements detected in these absorbers. Abundance ratios in the interstellar gas are affected by dust depletion and nucleosynthetic differences, and therefore, provide important clues regarding dust content, nucleosynthetic processes and star formation history in the ISM of the absorber galaxies. The remainder of this section discusses various abundance ratios derived from our data and compares them with the overall trends seen previously in DLAs and sub-DLAs.

4.1.1 Dust Depletion

Depletion of refractory elements into dust grains affects the abundances of these elements relative to non-refractory elements, and the amount of dust depletion can be estimated from the abundance ratio between a pair of refractory and non-refractory elements provided there is no difference between their nucleosynthetic yields. The abundances of the iron peak elements (Cr, Fe, Ni, Zn) are found to match each other closely over a wide range of metallicities ($-2 < Z < 0$) in Milky Way stars (Chen et al., 2000; Reddy, Lambert & Prieto, 2006), suggesting that they have little or no nucleosynthetic differences among them. Therefore, in absence of dust

grains, abundance ratios of these elements should be very close to the solar level, i.e., [Zn/Cr]∼[Fe/Zn]∼[Ni/Fe]∼0. However, Fe and Cr have much higher condensation temperatures compared to Zn, and in the typical ISM environment, are much more likely to condense out of the gas phase and into dust grains. Observational evidence for the depletion of Fe and Cr can be found in Milky Way's ISM (see Figure 2.5) where Fe and Cr are found to be less abundant compared to Zn by $\sim 1-2$ dex. This suggests that only $\sim 1-10\%$ of these elements may remain in gas phase while the rest gets locked in dust grains. Therefore, the ratios [Fe/Zn] and [Cr/Zn] can be used to estimate the depletion level in the ISM of absorber galaxies.

An anti-correlation between [Cr/Zn] and [Zn/H] in DLAs has been reported in previous studies (Pettini et al., 1997; Prochaska et al., 2002; Akerman et al., 2005) suggesting that the level of depletion increases with rising metallicity in the absorbing gas. This is expected given that dust grains are composed of the atoms and ions of metals. We have explored the variation of [Fe/Zn] with [Zn/H] by combining data from our high-z sample with measurements for DLAs and sub-DLAs from the literature and the results are plotted on Figure 4.1. Only measurements based on Fe and Zn detections were considered for clarity. Our results show that, similar to the [Cr/Zn] vs. [Zn/H] trend, an anti-correlation exists between [Fe/Zn] and [Zn/H] as well. A Spearman rank-order correlation test on the data reveals the Spearman rank-order coefficient ρ_s to be -0.57 while the probability that this coefficient can be obtained by chance is $\mathrm{P}(r_S) < 0.001$. Kendall's τ for our data was found to be $\tau = -0.81$ with the probability of no correlation being < 0.001. Our findings are found to be consistent with a similar trend reported by Meiring et al. (2009b).

In the absence of Zn in the low-z sub-DLAs, we estimated depletion based on the abundance ratios between S and other detected elements since S, like Zn, is also nearly undepleted in typical ISM environments. However, unlike [Fe/Zn], [Fe/S] alone can not be used to determine depletion as this ratio can also be affected by α/Fe

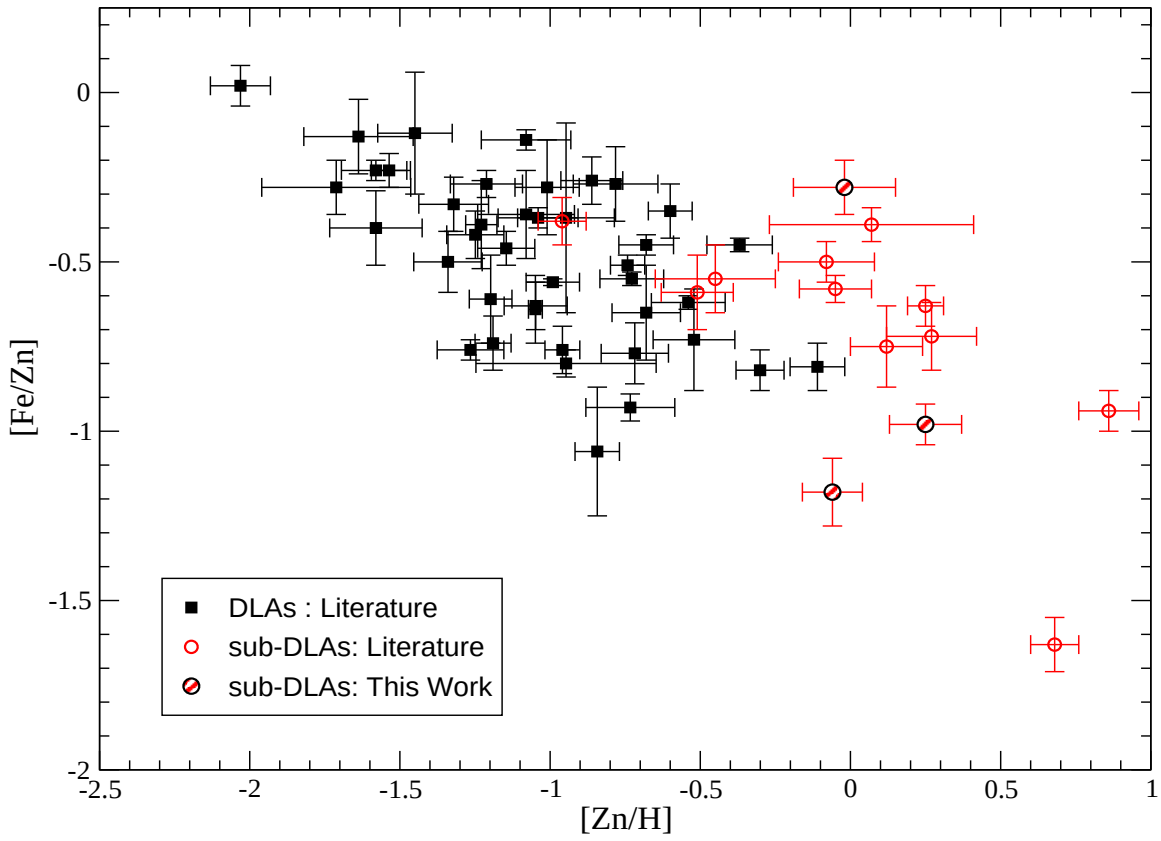

Figure 4.1 [Fe/Zn] vs. [Zn/H] for DLAs and sub-DLAs.

enhancement. Instead, we used ratios such as [C/S] or [Si/S] to estimated depletion in these systems. In the absorber toward Q2131-1207, the abundances of both C and Si are considerably sub-solar compared to S. This does not appear to be an ionization or saturation effect, and may suggest significant dust depletion in this absorber. In the absorbers toward Q0154+0448 and Q0441+4313, Fe is mildly under-abundant with respect to S, suggestive of modest dust depletion or α/Fe enhancement. In the absorber toward Q0456-2159, combining our results with Mg and Fe abundances from the literature suggests that dust depletion is not important, and that there may be nucleosynthetic α/Fe enhancement. We have detected P in two of the low-z sub-DLAs and P being weakly depleted, the abundance ratio between S and P should be free from depletion effects. This allows us an opportunity to investigate nucleosynthetic

differences between S and P. We measured [S/P] $= -0.23 \pm 0.23$ in the absorber toward Q0154+0448 and -0.03 ± 0.22 in the absorber toward Q0441+4313. The S and P abundances are thus consistent with being in the solar ratio. This is roughly similar to the finding of Battisti et al. (2012), who reported [S/P] $= 0.19 \pm 0.16$ and 0.19 ± 0.21 for two other sub-DLAs at $z < 0.3$. Thus, our values do not suggest a profound odd-even effect between these two elements.

4.1.2 Manganese to Iron Ratio

With the condensation temperatures of Mn and Fe being similar, the abundance ratio between these two elements is expected to be primarily governed by differences in their nucleosynthesis. The Mn abundance shows a strong metallicity dependence in Milky Way stars. [Mn/Fe] is found to be correlated with [Fe/H] in the sense that [Mn/Fe] increases with increasing [Fe/H] (e.g., Nissen et al. 2000; McWilliam et al. 2003; Gratton et al. 2004). This may suggest that Mn is produced primarily in Type Ia supernovae and the nucleosynthetic yield of Mn is higher than that of Fe in these explosions. As much as $\sim$ 75% of Mn could be produced in Type 1a supernovae explosions (Samland, 1998). We note that an opposite trend is seen between [α/Fe] and [Fe/H] in Milky way stars in the sense that [α/Fe] decreases with increasing [Fe/H]. As discussed in section 1.2, this α-enhancement in metal-poor gas suggests that Type II supernovae are the primary producers of α-elements while the majority of Fe is produced in Type Ia explosions. Since the abundance ratio between Mn and Fe is much less affected by differential depletion than [Si/H], the most widely used [α/Fe] indicator, [Mn/Fe] vs. [Fe/H] can be used as a proxy for [α/Fe] vs. [Fe/H] to understand the star formation history of the ISM.

A trend (similar to the one seen between [Mn/Fe] and [Fe/H] in Milky Way's stars) between [Mn/Fe] and [Zn/H] was reported to be present in DLAs and sub-DLAs by previous studies (e.g., Meiring et al. 2009b). To explore this further, we

have combined the [Mn/Fe] versus [Zn/H] data for the high-z absorbers observed by us with the data for DLAs and sub-DLAs taken from the literature, and plotted the combined sample in Figure 4.2. Data from Reddy, Lambert & Prieto (2006) for Milky Way stars and the interstellar abundance data for the Small Magellanic Cloud (SMC) from Welty et al. (2001) are also shown overlayed on the same plot. The trend of increasing [Mn/Fe] with increasing [Zn/H], seen in the Milky Way stars, is clearly present in the absorber galaxies as well. Kendall's τ for the complete absorber sample (DLA + Sub-DLA) was determined to be $\tau = 0.724$ with the probability of no correlation being 0.002. A Spearman rank correlation test gave the correlation coefficient $\rho_s = 0.521$ with the probability of no correlation of 0.006. Although the absorber sample shows a general correlation, the dispersion in the absorber data is larger compared to the stellar sample from Reddy, Lambert & Prieto (2006). The fact that galaxies detected through absorption represent various morphological types is likely to cause this dispersion with additional contribution from differential depletion onto dust grains between Mn and Fe. To explore this further, Kendall's τ for the DLA sample alone was determined to be $\tau = 0.917$ (with a probability of no correlation being 0.006), while $\tau = 0.872$ for the sub-DLAs with a probability of obtaining this value by chance being 0.026. There seems to be evidence for different [Mn/Fe] versus [Zn/H] trends between DLAs and sub-DLAs. While the DLA measurements are similar to the interstellar abundance data from the SMC, the sub-DLA data bear resemblance with the Mn and Fe abundance pattern seen in the Galactic bulge stars (see e.g, McWilliam et al. 2003). The linear regression slopes for the [Mn/Fe] vs. [Zn/H] data, being 0.12 ± 0.04 and 0.27 ± 0.03 for DLAs and sub-DLAs, respectively, differ at $\sim 3\,\sigma$ level. However, larger samples are needed to confirm this difference. A difference in the [Mn/Fe] vs. [Zn/H] relations for DLAs and sub-DLAs may suggest a difference in the stellar populations in these two classes of absorbers.

For the $z = 0.1012$ absorber toward Q0441+4313, [Mn/H] appears to be super-

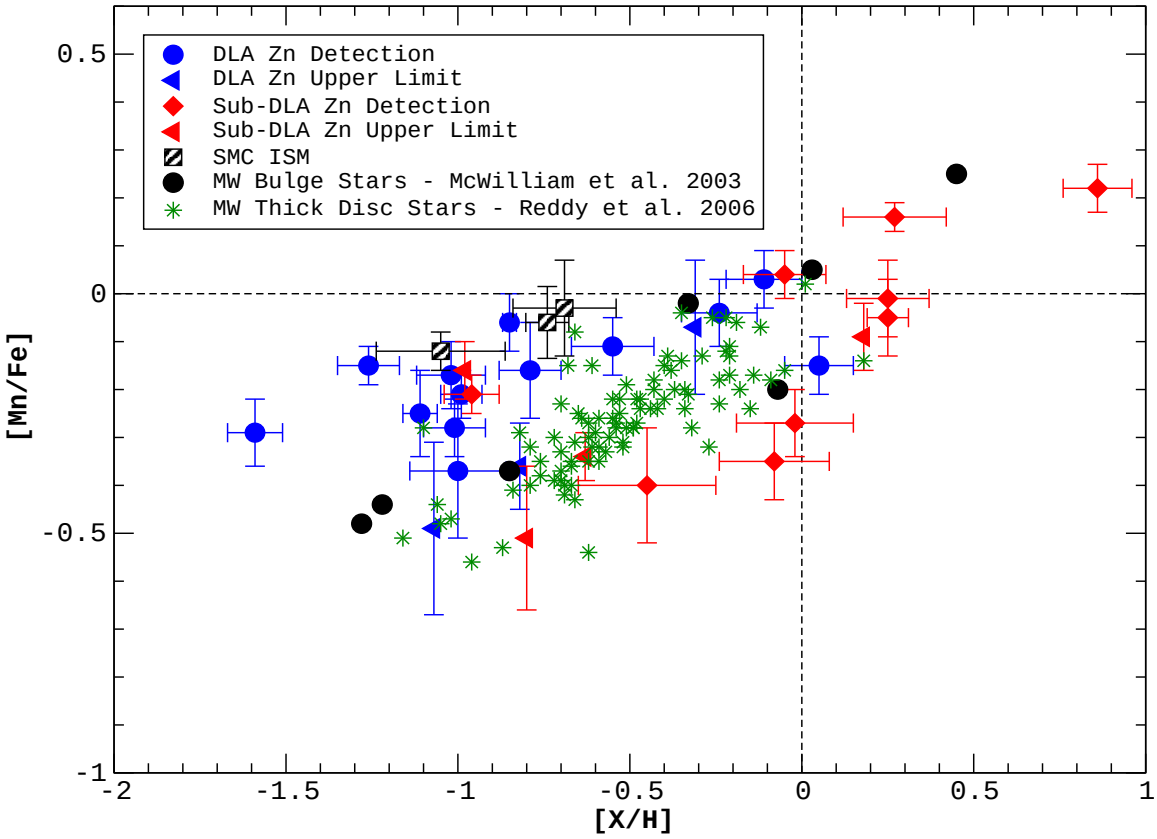

Figure 4.2 [Mn/Fe] vs. [Zn/H] for the sub-DLAs from this sample, as well as for sub-DLAs and DLAs from the literature. Milky Way stellar abundance data from Reddy, Lambert & Prieto (2006) are shown overplotted. Also shown are the interstellar abundance data for SMC from Welty et al. (2001).

solar and this system shows [Mn/Fe] $= 0.79 \pm 0.15$. Although we did not include this measurement in the analysis described above as the metallicity is based on S, it resembles the high [Mn/Fe] values seen in higher redshift metal-rich sub-DLAs and is consistent with the [Mn/Fe] vs. metallicity trend for sub-DLAs that is steeper than that for DLAs.

4.1.3 Nitrogen Abundances

The abundance of N relative to O or other α-elements in DLAs/sub-DLAs is of great interest because it can provide insights into the nucleosynthetic production of N. It is

believed that N is produced through both a primary process from C synthesized in the star itself, and a secondary process involving C and O from previous star formation (i.e., from C and O inherited by the star from the interstellar medium that it formed out of). Primary N is believed to be produced in mainly intermediate-mass stars, while secondary N production can occur in stars of all masses. The α-elements are believed to be produced predominantly in high-mass stars. The primary component is expected to dominate at low metallicities, while the secondary component is expected to dominate at high metallicities. Indeed, the ratio [N/α] observed in H II regions can be accounted for by primary N production in nearby low-luminosity galaxies (e.g., Van Zee & Haynes 2006) or blue compact dwarf galaxies (Izotov & Thuan, 2004), and by secondary N production in the more metal-rich nearby spiral galaxies (e.g., Van Zee et al. 1998).

In all three sub-DLAs where our data covered lines of N (see Table 3.21), the measured abundance of N is found to be much lower than that of S, with [N/S] ranging between -1.94 and -0.72 dex. This finding is similar to, but even more extreme than, that of Battisti et al. (2012), who found [N/S] between -1.12 and -0.58 dex for the sub-DLAs in their sample. For these high-metallicity absorbers, the observed [N/S] values lie much below the level expected from secondary N production. Part of this deficit in [N/α] could, in principle, arise from ionization effects but photoionization modelling for these absorbers (see section 4.2) find the ionization corrections to be insufficient to explain the observed low abundances. In general, the [N/α] vs. [α/H] data for sub-DLAs at $z < 0.5$ (from our work and Battisti et al. 2012) appear distinct from those for sub-DLAs at $z > 2$ (from Zafar et al. 2014). Our findings may suggest a different nucleosynthetic origin for N in these low redshift absorbers. Indeed, a tertiary N production mechanism has been suggested (e.g, Henry et al. 2000). Alternately, the low [N/α] values may simply represent the lower end of the scatter around the mean trend expected for secondary N production, possibly arising due to a delay in the

release of the secondary N (e.g., Vila-Costas & Edmunds 1993).

4.2 Ionization Corrections

The gas in the high H I column density absorbers is usually expected to be largely neutral due to the self-shielding of photons with $h\nu > 13.6$ eV. Zn and S in these systems are expected to be predominantly singly ionized. Consequently, the metallicities reported for such high N_{HI} absorbers are estimated from N_{ZnII}/N_{HI} or N_{SII}/N_{HI} ratios.[1] For absorbers with lower N_{HI}, such estimates may not be correct if they have non-negligible contributions from higher ionization stages. Several studies investigating the effect of ionization in DLAs (e.g., Howk & Sembach 1999; Vladilo et al. 2001; Prochaska et al. 2002) have found that in most cases the ionization correction factor, defined here as

$$\epsilon = [X/H]_{total} - [X^+/H^0], \tag{4.1}$$

where $[X/H]_{total}$ include contributions from all ionization stages, is $\lesssim 0.2$ dex for most elements. Sub-DLA systems, by virtue of lower H I in them, might be expected to show higher level of ionization. However, it has previously been shown that the ionization corrections are, in general, small for the sub-DLA systems as well (e.g., Dessauges-Zavadsky et al. 2003; Meiring et al. 2007, 2008).

To estimate the effect of ionization on the sub-DLA abundances presented here, we carried out photoionization modelling of these systems using version 13.01 of the CLOUDY photoionization code (Ferland et al., 2013). The models were generated assuming that the ionizing radiation incident on the gas cloud is a combination of extragalactic UV background and a radiation field produced by O/B type stars. The

[1]For an element X, X II is the spectroscopic convention for representing X^+, while H I represents H^0.

extragalactic UV background is adopted from Haardt & Madau (1996) and Madau, Haardt, & Rees (1999), evaluated at the redshift of the absorber. The O/B type stellar radiation field is based on a Kurucz model stellar spectrum for a temperature of 30,000 K. These radiation fields were mixed in equal parts to generate the incident radiation field. It has been suggested that the contribution from local sources to the ionization of DLA systems may not be negligible in comparison with the background ionizing radiation (Schaye 2006). In addition, we also include the cosmic microwave background at the appropriate redshift of the absorber, and the cosmic ray background in our simulation. We note however, that radiation from local shocks originating from white dwarfs compact binary systems or supernovae was not included in our models. For each of our absorbers, grids of photoionization models were produced by varying the ionization parameter, defined as

$$U = \frac{n_\gamma}{n_H} = \frac{\Phi_{912}}{cn_H} \tag{4.2}$$

(where n_H is the density of hydrogen, n_γ is the density photons capable of ionizing hydrogen, and Φ_{912} is the flux of radiation with hν > 13.6 eV), from 10^{-6} to 1. The models assumed the solar abundance pattern for the absorbers and were tailored to match the observed N_{HI} and the observed metallicity based on N_{ZnII} or N_{SII}. Column density ratios between various ions resulting from these grids of simulation were then compared with the observed values (determined from the column densities of various ions in several ionization stages listed in Tables 3.13 - 3.17) to constrain the ionization parameter and derive the ionization correction values. We note, however, that ionization in the gas depends strongly on the shape of the ionizing spectrum and our assumption for the incident spectrum is one among many possibilities. Given the assumptions described above, we can only arrive at some general conclusions regarding the strength of ionization in the gas. However, as we note in section 4.3, the model results appear to be consistent with the observational constraint on electron

density from a Si II fine structure line in at least one absorber where we have a robust measurement of Si II* and Si II. An example of the determination of ionization correction for the sub-DLAs in our sample is given in Figure 4.3 which describes the results for Q2123-0050.

4.2.1 Q2123-0050, $z_{abs} = 2.058$

With log N_{HI} = 19.35, this sub-DLA is one of the lowest N_{HI} systems in our sample. The observed ratios of column densities in higher ionization stages to those in the lower ionization stages are relatively high in this system, suggesting significant ionization in the absorbing gas. Column density ratios of the adjacent ions of the same element are more reliable observational constraints than the ratios involving different elements as the latter may be affected by differential depletion or intrinsic nucleosynthetic differences. Al and Si were the elements detected in this system with multiple ionization stages. We used the observed lower limit of the $N_{Si^{++}}$ to $N_{Si^{+}}$ ratio to obtain a lower limit on the ionization parameter at log U > -2.6. Furthermore, the observed upper limit on $N_{Al^{++}}/N_{Al^{+}}$ implies log U < -2.1. These results suggest that the observations underestimate the metallicity significantly as the ionization correction for [Zn/H] ranges between +0.54 dex to +0.63 dex. We adopt the correction to metallicity to be +0.59 dex derived for log U = -2.35, the mean value of the ionization parameter range described above. The corrections for [Fe/H] and [Mn/H] are derived to be -0.28 dex and -0.18 dex, respectively, suggesting a corrected value of +0.09 dex for [Mn/Fe]. The suggestion that the true depletion is much higher than observed (based on Zn II and Fe II) in a significantly ionized system (Meiring et al. 2008) seems to be true for this system as the corrected [Zn/Fe] is $\sim$ +0.9 dex higher than the observed [Zn/Fe] = +0.98 dex.

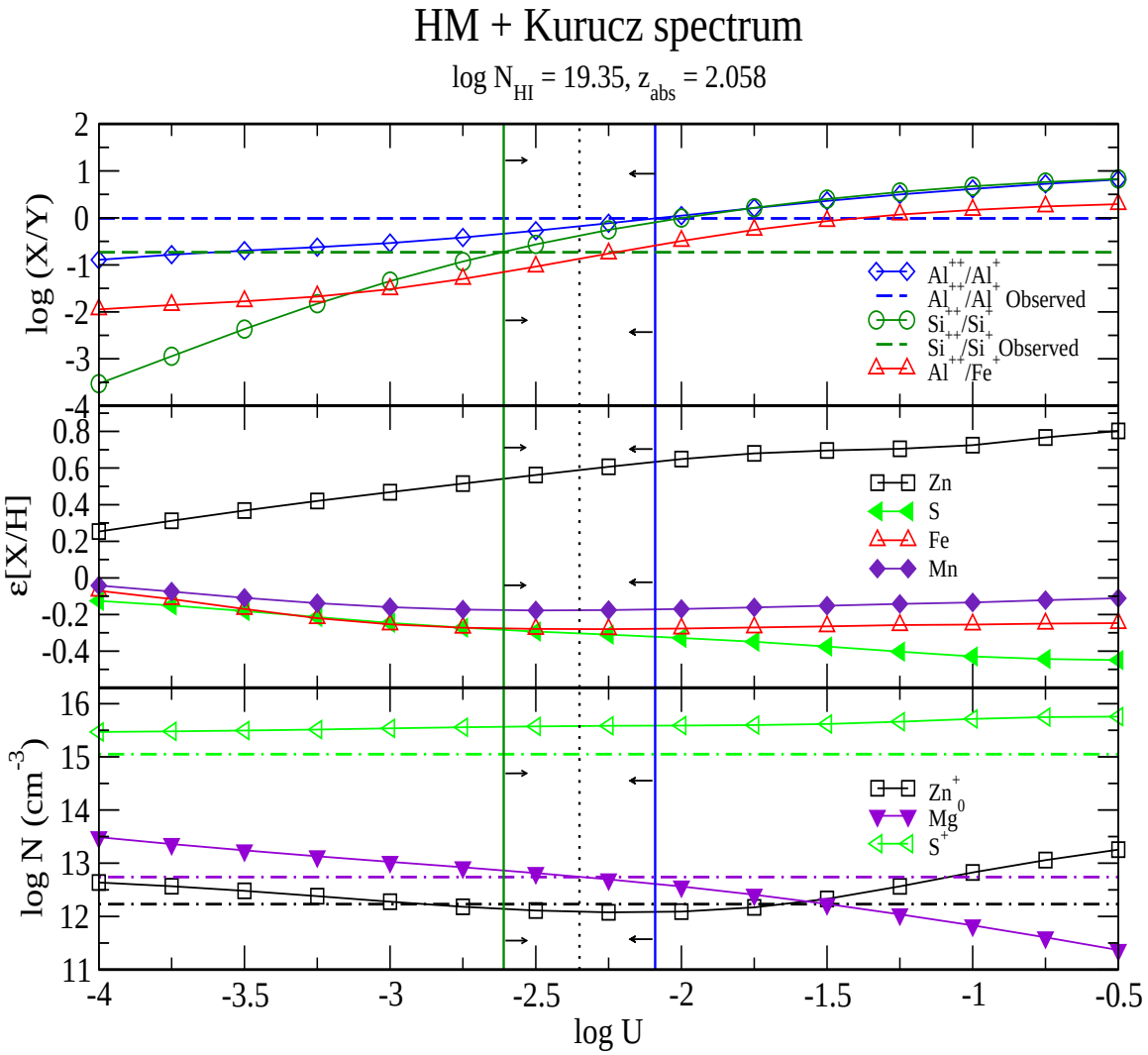

Figure 4.3 Results of the photoionization simulations for the sub-DLA toward Q2123-0050. The top panel shows the simulated logarithmic column density ratios of Al^{++}/Al^{+}, Si^{++}/Si^{+} and Al^{++}/Fe^{+}, plotted vs. the ionization parameter. The observed upper limit for Al^{++}/Al^{+} and the lower limit for Si^{++}/Si^{+} are also plotted in the same panel. The lower and upper limits on log U, determined by comparing the simulated and observed data, are represented by the vertical solid green and blue lines, respectively. The vertical dotted line represents the mean of these limits. The panel in the middle shows the ionization correction factors for Zn, S, Mn and Fe abundances in dex. The bottom panel shows column density predictions from a grid of models with the corrected metallicity incorporated in them. The comparison of the predictions with the observed column densities of Zn^{+} and Mg^{0}, also shown in the bottom panel using horizontal dot-dashed black and purple lines, respectively, suggests that the adopted ionization correction to metallicity is fairly reasonable.

4.2.2 Q1039-2719, $z_{abs} = 2.139$

The observed limits on $N_{Al^{++}}/N_{Al^{+}}$ and $N_{Si^{++}}/N_{Si^{+}}$ in this log $N_{HI} = 19.55$ absorber suggest -3.1 < log U < -2.7. This implies a correction for [Zn/H] between +0.45 dex and +0.51 dex. The ionization corrections for [Zn/H], [S/H], [Mn/Fe] and [Zn/Fe], derived at the mean log U = -2.9, are +0.48 dex, -0.20 dex, +0.08 dex and +0.67 dex, respectively.

4.2.3 Q1103-2645, $z_{abs} = 1.839$

Adjacent-ion column density ratios in the log $N_{HI} = 19.52$ absorber toward Q1103-2645 also suggest moderate ionization correction to the observed abundances. The observed lower limit on the $N_{Si^{++}}$ to $N_{Si^{+}}$ ratio allowed us to place a lower limit on the ionization parameter at log U > -3. As the Al II line was not detected in this system, we used the $N_{Al^{++}}/N_{Fe^{+}}$ ratio to further constrain the ionization parameter at log U = -2.6. The predicted correction for [S/H] was found to be -0.31 dex. Mn and Fe abundances were only mildly affected by ionization as shown by the estimated correction factors of -0.10 dex and -0.13 dex for [Mn/H] and [Fe/H], respectively. We note that using the Al^{++}/Fe^{+} ratio to estimate the ionization parameter may introduce uncertainties due to differential depletion or nucleosynthetic differences between the elements (see Meiring et al. 2007 for a more detailed discussion on the use of adjacent ion ratios in photoionization modelling).

4.2.4 Q1511+0908, $z_{abs} = 2.230$

The models for this log $N_{HI} = 19.70$ sub-DLA suggest little effect of ionization on the observed abundances. The observed value of $N_{Al^{++}}/N_{Al^{+}} = -0.41$ suggests corrections of only -0.16 dex and -0.10 dex for [S/H] and [Fe/H], respectively.

4.2.5 Q1311-0120, $z_{abs} = 1.762$

With log N_{HI} = 20.00, the sub-DLA toward Q1311-0120 is the highest N_{HI} sub-DLA in our sample and is found to be the least ionized. The limits on the column density ratios between Al^{++}/Al^{+} and Si^{++}/Si^{+} constrain the ionization parameter between -4.7 dex and -4.3 dex, limiting the correction for [Zn/H] between +0.10 dex and +0.18 dex (+0.14 dex at the mean ionization parameter of log U = -4.5). The ionization corrections for [Mn/H] and [Fe/H] were found to be negligibly small.

4.2.6 Q0154+0448, $z_{abs} = 0.1602$

For this system with log N_{HI} = 19.48, we used the observed lower limit on the N_{SiIII} to N_{SiII} ratio to obtain a lower limit on the ionization parameter of log U > -2.75. Furthermore, the observed upper limit on N_{SIII}/N_{SII} implies log U < -2.45. These results suggest that the ionization correction for [S/H] ranges between -0.24 dex to -0.29 dex. We adopt the correction to metallicity to be -0.26 dex derived for log $U = -2.60$ (the mean value of the ionization parameter range), which implies an ionization-corrected value of [S/H] = -0.04. The corresponding ionization correction for the N abundance derived from N I/ H I is +0.05 dex. For C, the ionization correction for the abundance derived from C II/ H I is -0.40 dex, i.e., the ionization-corrected [C/H] is > -0.96 dex.

4.2.7 Q0441+4313, $z_{abs} = 0.1012$

The observed ratio of N_{FeIII}/N_{FeII} in this log N_{HI} = 19.63 absorber suggests log $U = -2.3$. This implies a correction of -0.18 dex for [S/H], i.e. an ionization-corrected [S/H] of 0.08 dex. The corresponding corrections for Ar and N are +0.91 dex and +0.05 dex. After making the large Ar ionization correction, [Ar/H] is 0.37 dex, consistent within $\sim 1\sigma$ with [S/H]. In other words, the observed low value for

Ar I/H I in this system can be explained as an ionization effect.

4.2.8 Q0456-2159, $z_{abs} = 0.4744$

For this system with log N_{HI} = 19.45, S is the only element available in multiple ionization stages. The upper limit on N_{SIII}/ N_{SII} allowed us to place an upper limit on the ionization parameter of log $U <$ -2.6. This implies that the ionization-corrected [S/H] could be lower by at most 0.20 dex, i.e., [S/H] $>$ 0.25 dex. For N, the correction is $\lesssim$ 0.06 dex. For C, the ionization-corrected [C/H] could be lower by $\lesssim$ 0.24 dex.

4.2.9 Q2131-1207, $z_{abs} = 0.4297$

With log N_{HI} = 19.18, this sub-DLA has the lowest N_{HI} value in our sample. The observed upper limit on the N_{SIII} to N_{SII} ratio allowed us to place an upper limit on the ionization parameter of log $U <$ -2.8, which, in turn, suggests that the observed [S II/ H I] could overestimate the true [S/H] by $<$ 0.46 dex. We note, however, that the true ionization correction is likely to be much smaller. This is because the S III λ1190.2 line in this absorber is very noisy, and may be blended with not only Si II λ1190.4, but possibly also with Ly-α forest lines and/or noise. Thus, N_{SIII} and hence the S ionization correction are likely to be smaller. The corresponding estimate of the C ionization correction implies that the C abundance could be lower than that estimated from C II/H I by at most 0.5 dex. This means that the much lower observed abundance of C compared to S cannot be explained as an ionization effect.

Our photoionization models reveal that the ionization corrections to Zn based metallicity are positive in most cases while the observed S based metallicities may overestimate the true values. However, for most of the absorbers studied here, the ionization corrections to metallicity are found to be modest $\lesssim \pm$0.2 dex. Our simulations also suggest that the corrections towards Mn and Fe abundances are generally

small and do not have any significant effect on the [Mn/Fe] vs. [Zn/H] trend discussed in section 4.1.2. In addition, the estimated corrections to N abundances prove insufficient to explain the low [N/S] ratios seen in some of the absorbers studies here.

4.3 Si II* Absorption And Electron Density

The electron density of the absorbing gas can be estimated using fine structure absorption lines, for an assumed gas temperature. This is because the Si II upper level is expected to be populated predominantly by collisional excitation, and depopulated predominantly by radiative de-excitation. Si II* absorption has been detected in gamma-ray burst afterglows (e.g., Savaglio et al. 2012 and references therein), but is rare in quasar absorbers. Kulkarni et al. (2012) reported the first Si II* absorption in an intervening quasar DLA. Here we detect Si II* λ1264.7 absorption in the two low-z sub-DLAs toward Q0154+0448 and Q0441+4313. The corresponding Si II * λ 1194.5 lines are, unfortunately, hard to deblend from the red components of the Si II λ1193.3 lines. The Si II * λ1197.4 lines in these absorbers are located in noisy regions; but we have checked that these noisy regions are consistent with the expected Si II* λ1197.4 absorption based on the column density of Si II* derived from the λ1264.7 line.

In the sub-DLA at $z = 0.1602$ toward Q0154+0448, we find $N_{SiII^*}/N_{SiII} = 2.3 \times 10^{-3}$. In the sub-DLA at $z = 0.1012$ toward Q0441+4313, the Si II* λ1265 line is well-detected, but the Si II λ1260 line is saturated, allowing only an upper limit $N_{SiII^*}/N_{SiII} < 2.4 \times 10^{-2}$.

In order to estimate the electron density, we assume equilibrium between collisional excitation and spontaneous radiative de-excitation. In terms of the collisional excitation rate C_{12} and spontaneous radiative de-excitation rate A_{21}, the electron density is then given by

$$n_e = (N_{SiII^*}/N_{SiII})A_{21}/C_{12}. \quad (4.3)$$

We use the collisional excitation rate for Si II, $C_{12} = 3.32\times10^{-7}\,(T/10,000)^{-0.5}exp(\frac{-413.4}{T})$ cm^3 s^{-1}, and the spontaneous radiative de-excitation rate for Si II*, $A_{21} = 2.13\times10^{-4}$ s^{-1} (Srianand & Petitjean, 2000). Given the temperature dependence of C_{12}, we consider two illustrative cases of $T = 500$ K and $T = 7000$ K.

For the $z = 0.1602$ absorber toward Q0154+0448, we estimate the electron density to be $n_e = 0.77^{+0.48}_{-0.30}$ cm^{-3} for $T = 500$ K or $1.33^{+0.83}_{-0.51}$ cm^{-3} for $T = 7000$ K. We compare this electron density to the density of H^+ found by our photoionization model for this absorber. Based on the fraction of ionized H corresponding to the ionization parameter range suggested by our model, the ionized H density n_{H+} is estimated to be in the range 0.73 to 0.86 cm^{-3} with the value of 0.79 cm^{-3} at the mean log U of the range. This value is in good agreement with the electron density $n_e = 0.77^{+0.48}_{-0.30}$ cm^{-3} estimated above. It thus appears that despite the various simplifying assumptions in our photoionization model, it describes several observational constraints reasonably well. It is also interesting to note that the electron density in the sub-DLA toward Q0154+0448 is comparable to that in the $z = 2.2$ DLA with log $N_{HI} = 22.05$ toward J11350-0010 (0.53-0.91 cm^{-3}, Kulkarni et al. 2012).

For the absorber toward Q0441+4313, using the upper limit on Si II*/ Si II, we obtain only a weak upper limit on the electron density, i.e., $n_e < 8.0$ cm^{-3} for $T = 500$ K or $n_e < 13.9$ cm^{-3} for $T = 7000$ K. We note that the electron density in this absorber is likely to be much lower than this limit. This is because the Si II lines in this latter absorber are heavily saturated; therefore the Si II column density is likely to be much higher, and the N_{SiII^*}/N_{SiII} ratio is likely to be much lower.

For the absorber toward Q0456-2159, we place a 3σ upper limit on the Si II* column density of log $N_{SiII^*} < 11.86$ from the non-detection of the Si II* λ 1194.5 line. Combining this with the lower limit on the Si II column density of log $N_{SiII} > 14.18$,

we obtain an upper limit on the electron density of $n_e < 1.6$ cm^{-3} for T=500 K or $n_e < 2.7$ cm^{-3} for T=7000 K.

4.4 Metallicity Evolution

One of the main goals of this dissertation has been the study of sub-DLA metallicities at $z < 0.6$ and $z > 1.5$ to provide better constraints on the metallicity evolution of sub-DLAs and to compare that with DLA metallicity evolution. Here, we examine metallicity evolution in sub-DLAs and DLAs, by combining our data with sub-DLA and DLA metallicity measurements from the literature (Akerman et al. 2005; Battisti et al. 2012; Boissé et al. 1998; Centurión et al. 2003; de la Varga et al. 2000; Dessauges-Zavadsky et al. 2003, 2009; Ellison & Lopez 2001; Fynbo et al. 2011; Ge et al. 2001; Khare et al. 2004; Kulkarni et al. 1999, 2005; Ledoux et al. 2006; Lopez et al. 1999, 2002; Lopez & Ellison 2003; Lu et al. 1995, 1996; Meiring et al. 2006, 2007, 2008, 2009a; Meyer & York 1992; Meyer et al. 1995; Molaro et al. 2000; Nestor et al. 2008; Noterdaeme et al. 2008; Péroux et al. 2002, 2006a,b, 2008; Petitjean et al. 2000; Pettini et al. 1994, 1997, 1999, 2000; Prochaska & Wolfe 1998, 1999; Prochaska et al. 2001, 2002, 2003a,c; Rafelski et al. 2012; Rao et al. 2005; Srianand & Petitjean 2001). We note that, Rafelski et al. (2012) presented metallicity vs. redshift relation for a larger DLA sample (242 systems) but many of their metallicity measurements come from Si and Fe, elements prone to depletion. As discussed previously in section 2.2, Si and Fe are not preferred as metallicity indicators owing to the ambiguity in estimating dust depletion corrections. Therefore, the analysis presented here does not include Si or Fe measurements and is restricted to metallicities based on Zn or S (in cases where Zn was not detected or could not be covered by the spectra due to observational constraints) only. To the best of our knowledge, the metallicity evolution in sub-DLAs and DLAs presented here is based on the most comprehensive sample of depletion-free

metallicities for these systems consisting of 72 sub-DLAs and 195 DLAs. In addition to metallicities measured from Zn or S lines, this sample includes systems for which Zn and/or S lines could not be detected in their spectra but 3σ upper limits on Zn or S abundances could be obtained. Figure 4.4 shows the metallicity evolution for the DLA and sub-DLAs samples. The data have been binned in redshift, with 11-13 systems per sub-DLA bin and 16-17 systems per DLA bin. For each redshift bin, the combination of metallicity measurements and limits was treated with survival analysis using the non-parametric Kaplan-Meier estimator (Kaplan & Meier, 1958) and the N_{HI}-weighted mean metallicity along with its 1σ uncertainty (including both sampling and measurement uncertainties) were calculated following the procedures described in Kulkarni & Fall (2002).

We performed linear regression fits to the binned N_{HI}-weighted mean metallicity vs. median redshift relations for both DLAs and sub-DLAs. The slope of this fit gives a measure of the rate of the global mean metallicity evolution, while the intercept is the predicted mean metallicity at zero redshift. For DLAs, the best-fitting relation has a slope of -0.192 ± 0.047 and an intercept of -0.701 ± 0.114. For sub-DLAs, the best-fitting relation has a slope of -0.311 ± 0.095 and an intercept of 0.047 ± 0.159. This suggests that DLAs and sub-DLAs show metallicity evolution at the 4.1σ and 3.3σ levels, respectively. We note, however, that the lower significance of the presence of evolution in sub-DLAs is most likely to result from larger uncertainties in the slope owing to the smaller sample size. It is interesting to note that the mean metallicities of DLAs and sub-DLAs appear to evolve at similar rates, differing only at the 1.1σ level. However, the mean metallicity of sub-DLAs at zero redshift is clearly higher than that for DLAs, since the intercepts of the two relations differ at the 3.8σ level. We emphasize that, despite the small size of our HST sample of low-z sub-DLAs, the addition of these data has increased the previously existing extremely sparse sample of metallicity measurements at $z \lesssim 0.6$ by factor of ~ 4.

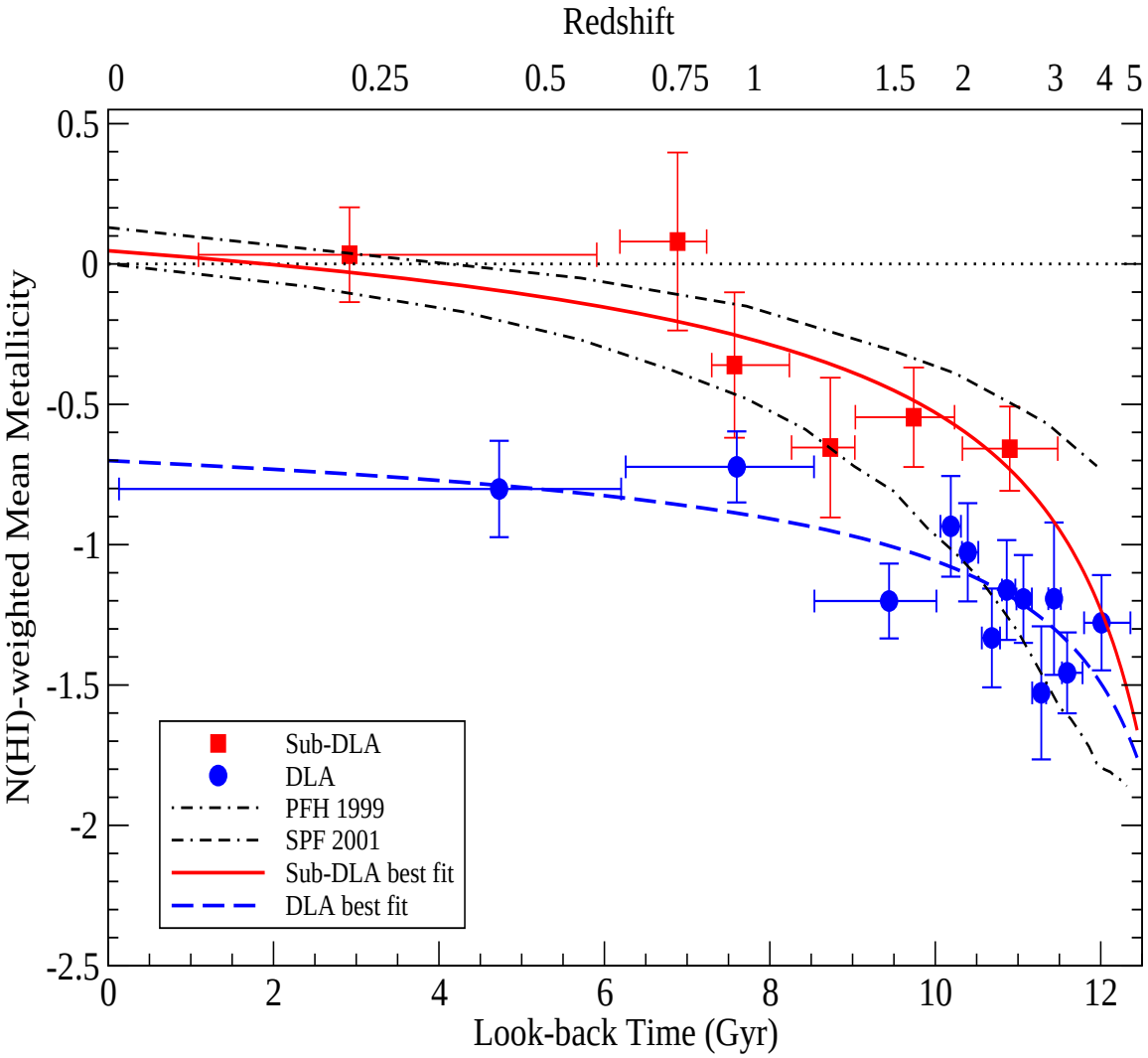

Figure 4.4 $N(HI)$-weighted mean metallicity vs. look-back time relation for 195 DLAs and 72 sub-DLAs with Zn or S measurements. The corresponding redshift scale is shown along the top axis of the figure. Filled circles show 12 bins with 16 or 17 DLAs each. Filled squares denote 6 bins with 11 - 13 sub-DLAs each. Horizontal bars denote ranges in look-back times covered by each bin. Vertical errorbars denote 1σ uncertainties. The bold solid and dashed curves show the best fits obtained from linear regression of the metallicity vs. redshift data for sub-DLAs and DLAs, respectively. The light dot-dashed and dot-double-dashed curves show, respectively, the mean metallicity in the models of Pei et al. (1999) and Somerville et al. (2001). Sub-DLAs appear to be more metal-rich and marginally faster-evolving than DLAs, at all redshifts where both DLA and sub-DLA metallicity data exist ($z \lesssim 3$).

Our observations put firm constraints on the metallicity evolution of sub-DLAs at low redshifts which could otherwise be estimated only by extrapolation form higher redshift studies (e.g, Kulkarni et al. 2007; Meiring et al. 2009b; Som et al. 2013). Our observed sample has improved the accuracy of the sub-DLA intercept determination by $\sim 45\%$. On the other hand, our observations of sub-DLAs at $z > 1.5$ have increased the previously existing sample at this redshift regime by $\sim 50\%$ providing better constraints on the metallicity evolution of sub-DLAs at high redshifts, especially at $z > 2$. Earlier studies had suggested that the trend of higher mean-metallicity in sub-DLAs compared to DLAs, seen at $0.6 < z < 1.5$, might disappear at $z > 2$ (Kulkarni et al., 2007; Meiring et al., 2009b). In contrast, as shown in Fig. 4.4, the mean metallicity of the sub-DLA bin between $2 \lesssim z \lesssim 3$ is found to be significantly higher than the mean metallicities of all the DLA bins in this redshift range. This suggests that sub-DLAs, on average, continues to be more metal rich than DLAs at $z \lesssim 3$. Our observations of the low and high redshift sub-DLAs have also improved the accuracy of the global mean metallicity evolution rate in sub-DLAs by $\sim 45\%$.

Figure 4.4 also shows the comparison of the observations with theoretical model predictions for evolution of global interstellar metallicity. The mean interstellar metallicity from the chemical evolution model of Pei et al. (1999) is shown using the light dot-dashed curve (PFH 1999). This model calculates the coupled global evolution of stellar, gaseous, and metal contents of galaxies by incorporating the optimum fit for the cosmic infrared background intensity and observational constraints derived from optical galaxy surveys and the comoving H I density inferred from DLA data. The light dot-double-dashed curve (SPF 2001) represents the mean metallicity evolution of interstellar cold gas predicted by a semi-analytic model of galaxy formation in the cold dark matter merging hierarchy by Somerville et al. (2001). This model assumes a constant-efficiency quiescent star formation in addition to starbursts triggered by galaxy mergers. It is evident from Fig. 4.4, that the metallicity evolution in

sub-DLAs is consistent with the chemical evolution models over most of the redshift range probed so far, and especially at low redshifts, reaching solar level at $z = 0$. The sub-DLA trend bears a closer resemblance with the merger driven 'collisional starburst model' by Somerville et al. (2001). On the other hand, the DLA data are in poor agreement with the model predictions and DLA metallicity reaches only $\sim$ 1/5th of the solar value at $z = 0$. The DLA trend becomes consistent with PFH 1999 only at $z \gtrsim 2$. Some recent studies (e.g., Davé & Oppenheimer 2007) predict a low DLA metallicity at $z = 0$, but do not correctly predict the higher redshift DLA metallicities. The difference in the metallicity evolution trends in DLAs and sub-DLAs may suggest that the galaxies traced by these absorbers follow separate evolutionary tracks established as early as $\sim$2 Gyrs after the Big Bang. However, given the small difference between the slopes of the trends, the observed difference can extend further back in time. Sub-DLA data at redshifts higher than 3 are essential to provide further constraints on the epoch of establishment of these distinct evolutionary tracks.

Comparing the metallicities for DLAs and sub-DLAs with those for galaxies detected in emission can provide clues to the understanding of the nature of the absorbing galaxies. It is well-known that galaxies detected in emission show a correlation between their stellar mass and the gas metallicity (e.g., Tremonti et al. 2004; Erb et al. 2006). Furthermore, the mass-metallicity relation is found to evolve with redshift. Maiolino et al. (2008) found that for star forming galaxies at $M_* \sim 10^{10}\,M_\odot$, the metallicity at $z \sim 2.2$ is lower by a factor of about 2.5 with respect to that at $z \sim 0$. The drop is less steep for more massive galaxies, indicating that the latter got enriched at earlier epochs, consistent with the mass-downsizing scenario. Interestingly, the sub-DLA metallicity evolution shown in Fig. 4.4 seems to resemble the trend found by Maiolino et al. (2008) for star forming galaxies with $M_* \sim 10^{10}\,M_\odot$. The metallicity evolution in DLAs, however, does not resemble any of the trends found by

Maiolino et al. (2008) for star forming galaxies with $9 < logM_*/M_\odot < 11$, suggesting that DLA host galaxies have not undergone much star formation and chemical enrichment even by the current epoch. This is consistent with the observed agreement of DLA metallicity distribution with that for the Milky Way halo stars, suggesting that most DLAs are not representative of the disks of Milky Way-type galaxies (e.g., Pettini 2004).

We note here that the ionization corrections described in section 4.2 were not considered while calculating the metallicity-redshift relation since the majority of values from the literature do not include ionization corrections. Moreover, it is not possible to obtain homogeneously ionization-corrected measurements by just compiling values from multiple studies, given the various uncertainties associated with the radiation field, depletion pattern, etc. The only way to obtain such a homogeneous dataset would be to run ionization models in a consistent manner on all systems in the literature. This would be a much broader study that is beyond the scope of the present work. However, we note that the ionization corrections are found to be modest ($\lesssim 0.2$ dex) in most sub-DLAs studied here and in other studies (e.g., Meiring et al. 2007, 2009b; Battisti et al. 2012). We also emphasize that even if the metallicities are adjusted for ionization corrections in the few cases where these corrections are available, the mean sub-DLA metallicity trend is not expected to be lower than that shown in Fig. 4.4. This is because, while the S metallicities may be lower by at most ~ 0.2 dex on average, the Zn metallicities (which constitute the majority of the sample) are expected to offset this effect, since the ionization corrections for Zn are generally found to be positive (see section 4.2). Thus, the large difference between the intercepts of the best-fitting metallicity-redshift relations derived above for DLAs and sub-DLAs is expected to still persist, or perhaps even increase, after incorporating ionization corrections for all the absorbers in the sample.

4.5 Investigation of Selection Bias

As discussed in Section 3.1, the systems selected for our observations were confirmed sub-DLAs based on their measured N_{HI} values. The availability of N_{HI} was the primary selection criterion for our observed sample. This is true also for most of the earlier studies of sub-DLAs (e.g., Meiring et al. 2009b and references therein). However, majority of the H I column density measurements for the absorbers at $z \lesssim 1.5$ came from HST STIS/FOS spectra of DLAs and sub-DLAs (Rao, Turnshek, & Nestor 2006) that were selected for observation based on the presence of strong Mg II λ2796 and Fe II λ2599 lines ($W_{2796} > 0.5$ Å; $W_{2599} > 0.5$ Å) in their optical spectra. This could potentially introduce a bias toward more metal-rich systems in the sub-DLAs based on the argument that a system with large W_{2796} and W_{2599} would have large N_{MgII} and N_{FeII} (hence a large N_{ZnII}), and therefore a higher metallicity for low N_{HI}. However, Kulkarni et al. (2010) showed that the selection of systems with strong Mg II lines does not introduce any such bias. Here, we explore the possibility of a bias due to the selection based on strong Fe II lines. Upon considering the observed metallicity vs. W_{2599} data for sub-DLAs and DLAs, we find a correlation between the observed metallicity and the strength of Fe II λ2599 line for DLAs (Kendall's τ value of 0.744, $P(\tau) = 0.0005$), but not for sub-DLAs ($\tau = 0.171$, $P(\tau) = 0.302$). This suggests that the sub-DLA data have no systematic bias toward high metallicity systems.

To investigate this issue further, we explored the variation of W_{2599} with metallicity by simulating Fe II λ2599 line profiles in DLAs and sub-DLAs considering a variety of physical conditions of the absorbing gas. In our simulations, the H I column density values were chosen to resemble the observed ranges in the DLA and sub-DLA samples: randomly in the range 20.3-22.0 for DLAs, and for sub-DLAs, 75% of all the N_{HI} values were randomly selected from the range 19.7-20.3 while the rest

were selected from range 19.0-19.7. For each value of N_{HI}, the metallicity [X/H] was chosen randomly to be between -2.5 and +1.0, and the depletion factor for Fe was selected randomly within a range of -0.6 to -1.2 dex. This Fe depletion range is fairly conservative considering the observed range of -0.1 to -1.6 dex for [Fe/Zn] in low-z sub-DLAs with Zn detections (e.g., Meiring et al. 2009b). The number of velocity components in each artificial profile was chosen randomly between 3 and 15 having random velocity values within a range constrained by the selected number of components (the maximum range being -375 to 375 km s^{-1} for 15 components). Each velocity component was assigned a Doppler b parameter value selected randomly from a range of 3-20 km s^{-1}. Finally, the equivalent width of the resulting Fe II λ2599 line profile was measured. The measurements from 30,000 artificial line profiles generated in this way were then binned over metallicity into 0.25 dex bins. Figure 4.5 shows the results from our simulations in comparison with the observed data.

Figure 4.5 suggests that a trend of gradually increasing W_{2599} with increasing metallicity is expected to be observed. The observed DLAs do show a correlation resembling the median simulated trend, except that no significantly super-solar DLAs are seen. In contrast, although most sub-DLA detections lie within the $\pm 1\sigma$ range of the simulated trend, they do not seem to follow the median simulated trend. It is clear from the upper panel of Figure 4.5 that an observed sample with $W_{2599} > 0.5$ Å can have sub-DLAs with [X/H] as low as -1.1 dex even for the relatively large depletion factors assumed above. All of the observed metallicities for sub-DLAs (with detections) appear to be considerably higher than that. Our simulations show that Fe II selection can not explain the observed super-solar metallicities in sub-DLAs and the lack of that in DLAs. We, therefore, conclude that the higher mean sub-DLA metallicities compared to DLAs do not appear to be due to an Fe II selection bias. We note that our conclusion is consistent with the lack of Mg II selection bias suggested by Kulkarni et al. (2010), since Fe II λ 2599 is close in strength to Mg II λ 2796

(log λf = 2.793 for Fe II λ 2599 and 3.236 for Mg II λ 2796). We also note that, the chemical evolution of DLAs and sub-DLAs described in section 4.4 show that sub-DLAs are, on average, more metal rich than DLAs even at $z > 1.5$, where the observed samples are selected based only on the absorption cross-section of neutral gas, without any prior knowledge of the strengths of metal lines.

4.6 H I Column Density vs. Metallicity Trend

Our work has shown that the lower N_{HI} sub-DLAs, on average, are more metal rich that the higher N_{HI} DLAs over $0 < z \lesssim 3$. Naturally the question arises whether this is a manifestation of an underlying relation between H I column density and metallicity, or, in other words, whether an anti-correlation between N_{HI} and metallicity exists in quasar absorber galaxies. Moreover, Lehner et al. (2013) suggested that the metallicity distribution of Lyman-limit systems at $z < 1$ is bimodal, with a metal-rich branch tracing outflows and a metal-poor branch tracing inflowing cold accretion streams. If sub-DLAs and DLAs also arise in inflows and outflows, as indeed suggested by some hydrodynamical simulation models of structure formation, they should exhibit a similar bimodality and an anti-correlation between N_{HI} and metallicity should not exist for these systems. York et al. (2006) reported an anti-correlation between H I column density and metallicity based on a sample of ∼800 QSO absorbers observed in the SDSS. Similar trends were suggested by Khare et al. (2007) and Meiring et al. (2009b) using only Zn based metallicities (both measurements and upper limits) for DLAs and sub-DLAs primarily at $z > 0.6$.

Here, we explore the N_{HI} -metallicity relation using the Zn or S metallicity sample introduced in section 4.4. We emphasize that, in comparison with the earlier studies, the DLA and sub-DLA sample used in this analysis is both larger and and represents a wider redshift baseline. As shown in Figure 4.6, the data for the entire sample

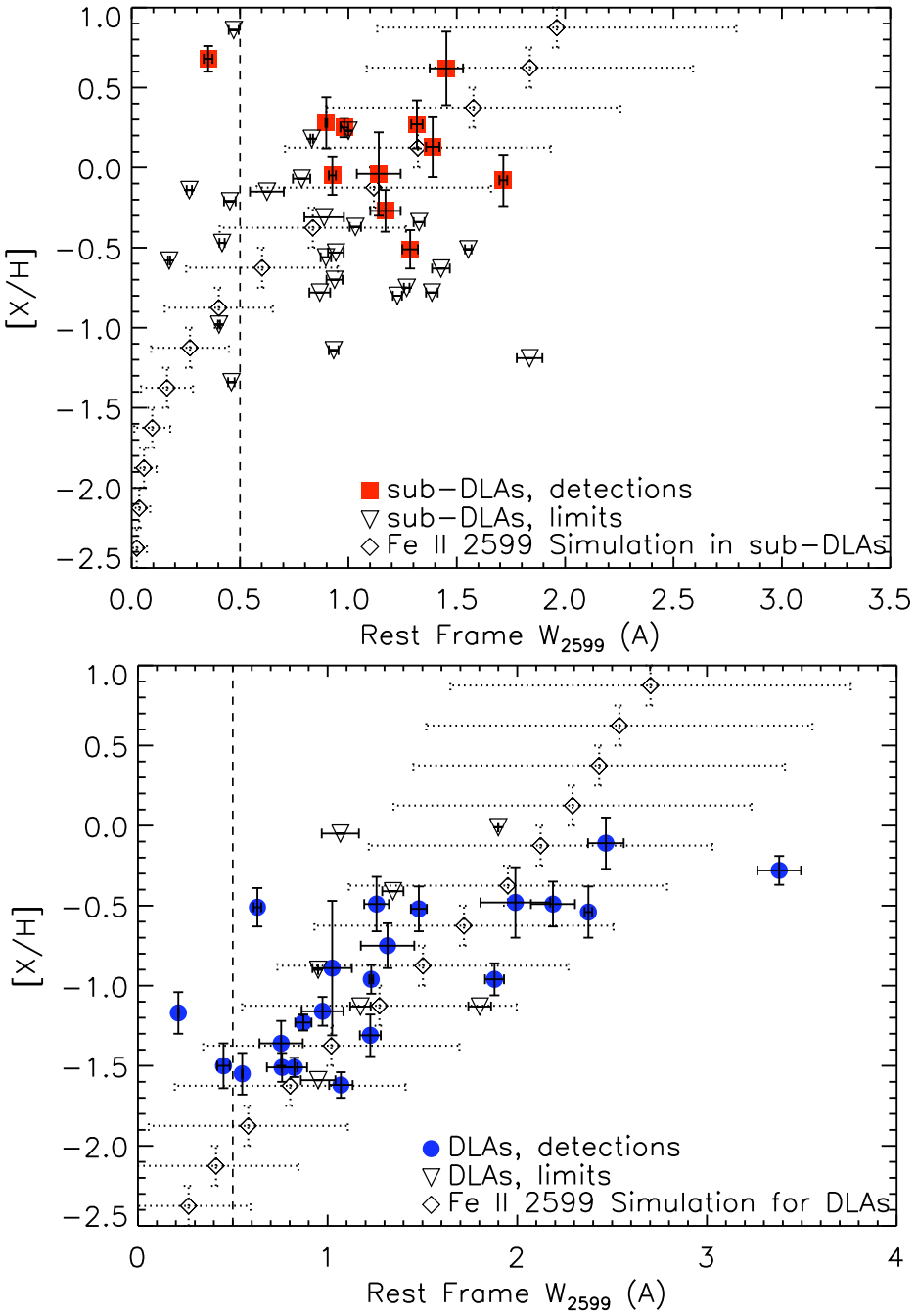

Figure 4.5 Simulated and observed data for metallicity vs. rest-frame equivalent width of Fe II λ2599, for sub-DLAs (*upper panel*), and DLAs (*lower panel*). Squares, triangles, and circles represent the observed data while the diamonds show median W_{2599} values from 30,000 simulations, in bins of 0.25 dex in [X/H], plotted as a function of metallicity. The dashed horizontal error bars on the diamonds show the $\pm 1\,\sigma$ ranges in the W_{2599} values generated in the simulations. The DLA data follow the simulated trend and show a correlation between the metallicity and W_{2599}, but the sub-DLA data do not show a correlation.

(including upper limits which account for ~ 40 % and ~ 50 % of DLA and sub-DLA metallicities, respectively) appear to be moderately anti-correlated (Spearman rank-order correlation coefficient $\rho_s = -0.292$ with a < 0.001 probability of no correlation) while the trend is stronger ($\rho_s = -0.512$ with a < 0.001 probability of no correlation) for the data containing metallicity measurements based on Zn or S detections only. However, the existence of a bimodal metallicity distribution for DLAs and sub-DLAs can not be ruled out by an analysis which includes the upper limits or simply omits them. If a bimodality truly existed and the systems with non-detections of Zn or S in fact belonged to a metal-poor branch, with metallicities much lower than suggested by the Zn or S upper limits, the anti-correlations seen in Fig. 4.6 would not represent the true nature of the sample.

To account for this possibility, we revised our sample by including metallicity measurements based on Si or Fe (in the absence of Si), where available, for those sub-DLAs that have non-detections of both Zn and S. The Si or Fe based metallicity measurements replace ~ 75 % of the Zn or S upper limits in the original sample. The revised sample thus produced consists of 245 metallicity measurements in the range from ~ -2.7 dex to ~ 0.8 dex while the log N_{HI} values range from 19.04 dex to 21.85 dex. The revised log N_{HI} vs. [X/H] data are shown in Figure 4.7.

As seen in Figure 4.7, the anti-correlation in the N_{HI}-metallicity data persists even after including the Si or Fe measurements in lieu of the the Zn or S upper limits. Spearman's ρ_s for the data is found to be -0.459 with the probability that such an anti-correlation can be found by chance being < 0.001 while Kendall's $\tau = -0.619$ (with $P(\tau) < 0.001$). To test the accuracy of these statistics, we created an artificial sample for the N_{HI}-metallicity data which had the same H I column density distribution as the observed sample but the metallicity assigned to each N_{HI} value was chosen randomly from the range of metallicities mentioned above. The statistical tests, as expected, suggest no correlation for the artificial sample ($\rho_s =$

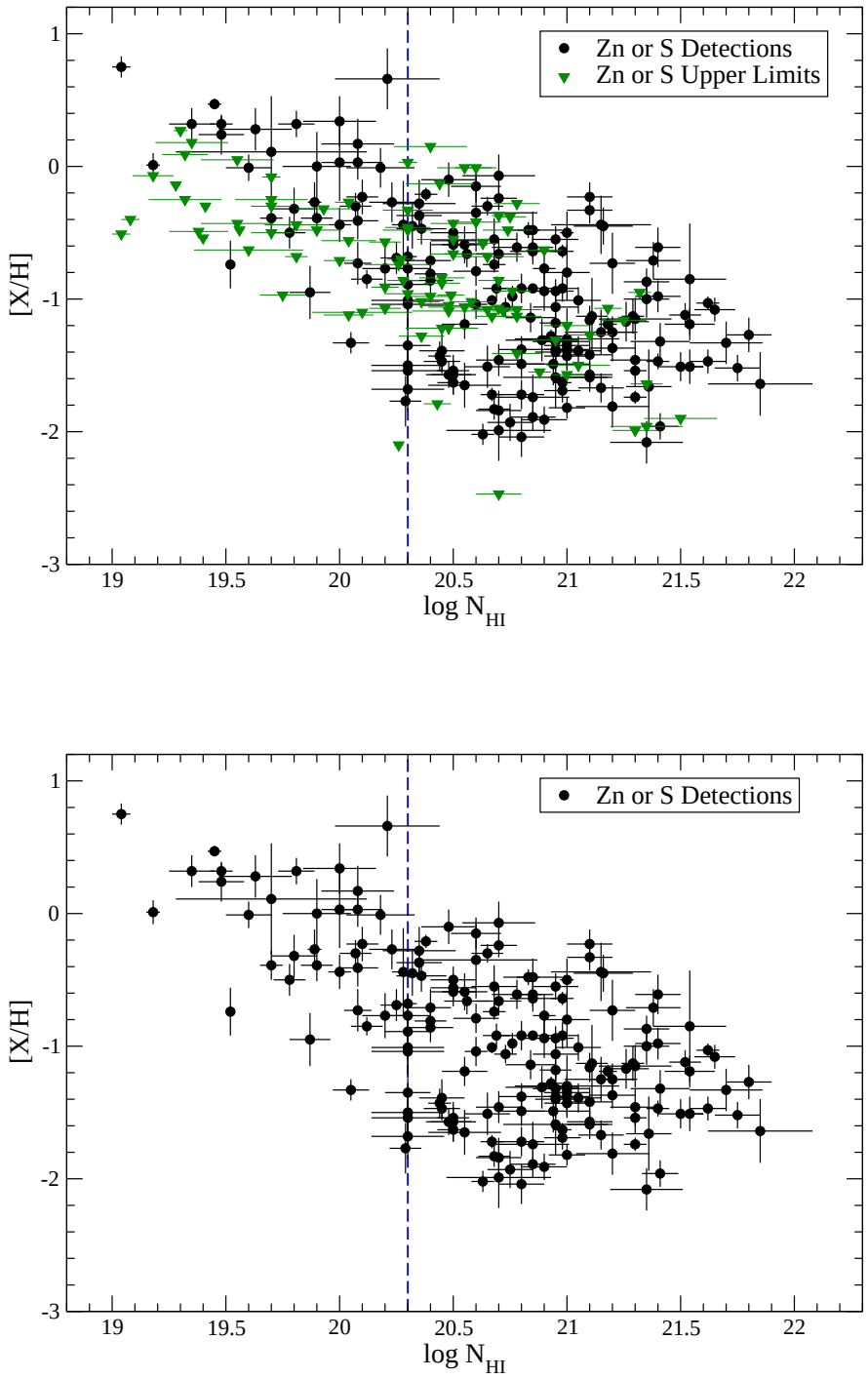

Figure 4.6 **Upper panel:** log N_{HI} vs. [X/H] data for our entire Zn or S based sample (including Zn or S upper limits). **Lower panel:** log N_{HI} vs. [X/H] data based on Zn or S detections only. The vertical blue dashed line represents the threshold between DLAs and sub-DLAs.

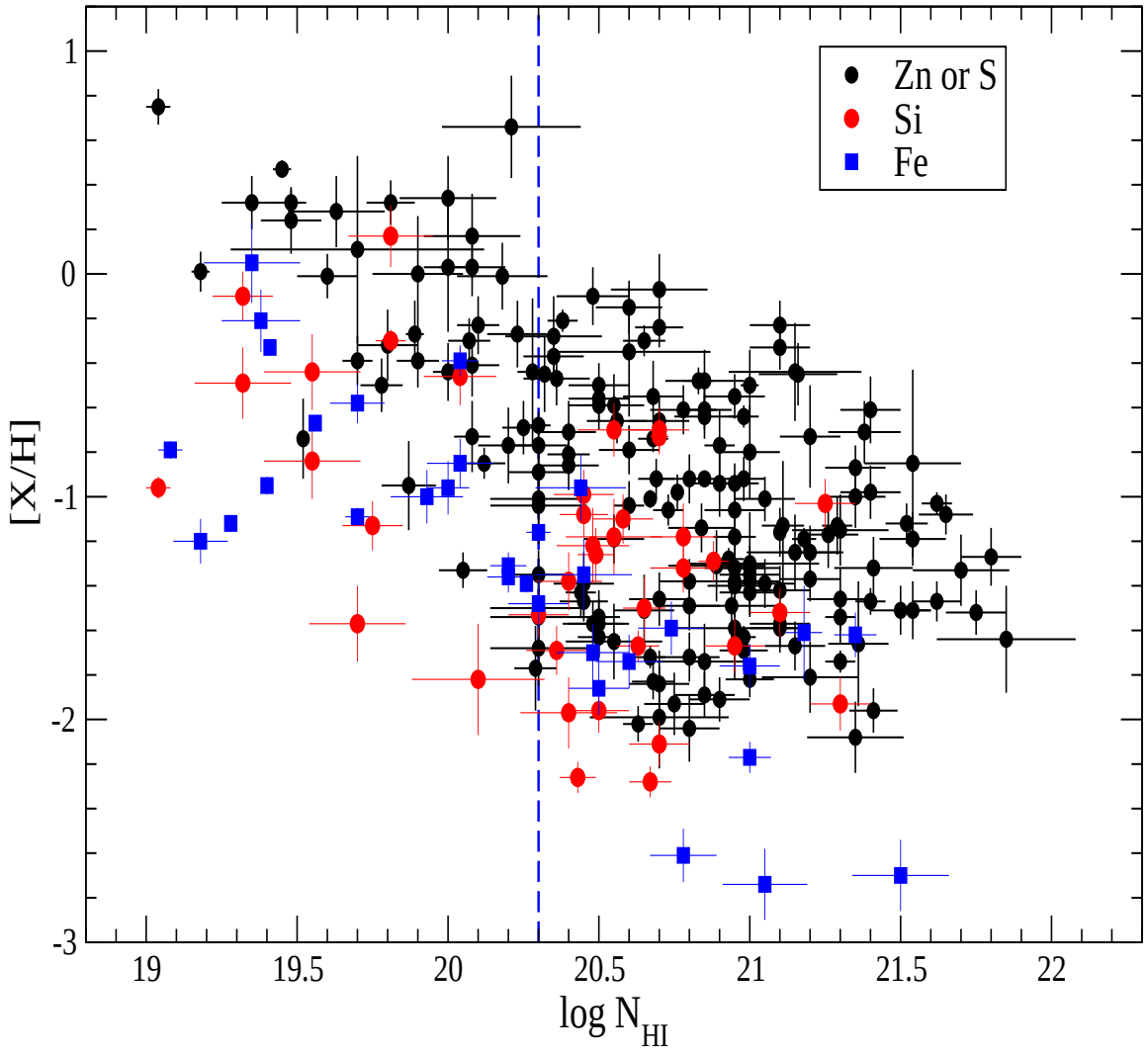

Figure 4.7 log N_{HI} vs. [X/H] data for the revised sample.

0.001, $P(\rho_s) = 0.983$; $\tau = 0.011$, $P(\tau) = 0.895$). We note that the scatter in the observed trend in largely due to the mixing of "depletion-free" metallicities (from Zn or S) with metallicities affected by depletion (from Si or Fe). In fact, N_{HI}-metallicity data from the smaller sub-sample of Si or Fe based metallicities alone appear to show a strong anti-correlation ($\rho_s = -0.637$, $P(\rho_s) < 0.001$; $\tau = -0.901$, $P(\tau) < 0.001$) and follows a trend very similar to the one shown by the depletion-free metallicities but shifted down the metallicity axis due to depletion.

Our results strongly suggest the existence of a log N_{HI}-metallicity anti-correlation

even when using non-uniform metallicity indicators and not correcting for depletion. We thus believe that the anti-correlation is not an artifact of insufficient detection sensitivity. The higher incidence of metal-rich sub-DLAs could be partly explained as a stronger dust obscuration bias for DLAs than for sub-DLAs, if dust extinction depends strongly on the metal column density (Vladilo & Péroux, 2005). In other words, while metal-rich, dusty DLAs could obscure their background quasars more, leading to a deficit of such systems in the observed samples, such a selection effect would be weaker for sub-DLAs. Another possibility is that the deficit of high-N_{HI}, high-metallicity DLAs may arise from H I becoming predominantly H_2 above an N_{HI} threshold that decreases with increasing metallicity (Schaye, 2001; Krumholz et al., 2009), but that such an effect is not as relevant at the smaller N_{HI} of the sub-DLAs. Alternatively, the gas-poor, metal-rich sub-DLAs may arise in more massive galaxies than the gas-rich but metal-poor DLAs, or in other words, the observed N_{HI}-metallicity anti-correlation may suggest that the more massive absorber galaxies undergo star formation earlier than the their less massive counterparts.

4.7 Kinematics of Absorber Galaxies

Based on a sample of star-forming galaxies at z$\sim$0.1, Tremonti et al. (2004) found a correlation between stellar mass and gas-phase metallicity for these galaxies. Similar mass-metallicity relations have been suggested by Savaglio et al. (2005) for $0.4 < z < 1.0$ galaxies selected from the Gemini Deep Deep Survey and the Canada-France Redshift Survey and by Erb et al. (2006) for UV-selected star forming galaxies at $z \sim 2.3$. Nestor et al. (2003) and Turnshek et al. (2005) noticed a correlation between the Mg II λ 2796 equivalent width and the metallicity for strong Mg II absorbers at $1 \lesssim z \lesssim 2$. The possible existence of a mass metallicity relationship for DLA absorbers, assuming the velocity width of optically thin lines to be proportional to

the mass, has been put into evidence recently (Péroux et al., 2003a; Ledoux et al., 2006). As the velocity width of the low-ionization absorption lines potentially probes the depth of the underlying gravitational potential well of the DLA systems, this quantity can be used as a proxy for the stellar mass of these systems, which has been difficult to measure. Bouché et al. (2006), however, find an anti-correlation between the Mg II equivalent width and the estimated halo mass based upon an indirect mass indicator. Also, Zwaan et al. (2008) show that the velocity width and mass do not correlate well in local analogues of DLAs.

To investigate the velocity width-metallicity relation in sub-DLAs, we measured the velocity width values for the systems in our sample following the analysis of Wolfe & Prochaska (1998). The velocity width for a system was measured using an absorption profile (in velocity space) from a low-ion transition seen in the system. High-ionization lines are not suitable for this analysis as their velocity widths are likely to be dominated by large scale thermal motions in the gas. The measurement method involved the conversion of the low-ion transition profile, $\mathrm{I}_{obs}(v)$, into the corresponding apparent optical depth profile, $\tau(v)_a$, through the following relation

$$\tau(v)_a = ln[I_0(v)/I_{obs}(v)], \tag{4.4}$$

where $\mathrm{I}_0(v)$ represents the continuum level, and $\mathrm{I}_{obs}(v)$ is the observed intensity of the normalized transition profile in velocity space. The apparent optical depth was then integrated over the entire line profile to yield τ_{int}, the total optical depth within the absorption profile. Finally, the velocity width was determined as $\Delta v_{90} = [v(95\%) - v(5\%)]$, where $v(95\%)$ and $v(5\%)$ define the velocity range within which 90% of τ_{int} was contained.

In the case of very strong line profiles, the optical depth can not be measured accurately and the velocity width determined using such a line can be overestimated. On the other hand, velocity width measured from a very weak line becomes highly

sensitive to the continuum noise and can be underestimated, as part of the absorbing gas can remain undetected. To select profiles which are neither strongly saturated nor too weak, we required the transitions profiles used to measure the velocity widths to satisfy $0.1 < I_{min}/I_c < 0.6$, where I_c is the continuum level intensity, and I_{min} is the intensity at the location of the strongest absorption in the line profile. After selecting a profile, we visually inspected the strongest low-ion transitions to ascertain the velocity range over which the selected profile should be integrated to determine Δv_{90}. Figure 4.8 shows an example of Δv_{90} determination. Table 4.1 lists the velocity width measurements from our systems along with the line profiles used.

Figure 4.9 shows the velocity dispersion versus metallicity data our sample as well as for DLAs and sub-DLAs from the literature. Only systems for which Zn or S was detected have been plotted. A general trend of increasing ΔV_{90} with higher metallicity can be seen considering the sub-DLAs and DLAs together. A Spearman rank-order correlation test on the entire sample containing 51 DLAs and 29 sub-DLAs reveal the correlation co-efficient to be $\rho_s = 0.59$ with very little probability (<0.001) of no correlation. The Kendall's τ for this sample is 0.84 (the probability of no correlation, $P(\tau) < 0.001$). This further strengthens the argument that velocity dispersion offers a good measure of the mass of the absorber galaxies provided an underlying mass-metallicity relation exists for them. The correlation for the DLA sample alone is much stronger ($\rho_s = 0.74$, $P(\rho_s) < 0.001$; $\tau = 1.1$, $P(\tau) < 0.001$) while the sub-DLA sample appears to be less correlated ($\rho_s = 0.28$, $P(\rho_s) = 0.14$; $\tau = 0.42$, $P(\tau) = 0.11$). An inherent scatter in the data is indeed to be expected as they represent a collection of random sightlines through galaxies at various inclinations and impact parameters. Moreover, the observed velocity width includes effects of local velocities and turbulent motion in the gas on top of the velocity dispersion due to the underlying gravitational potential well. Therefore, the large scatter in the sub-DLA data, although in part due to the relatively smaller sample size, could indicate higher levels of turbulence in

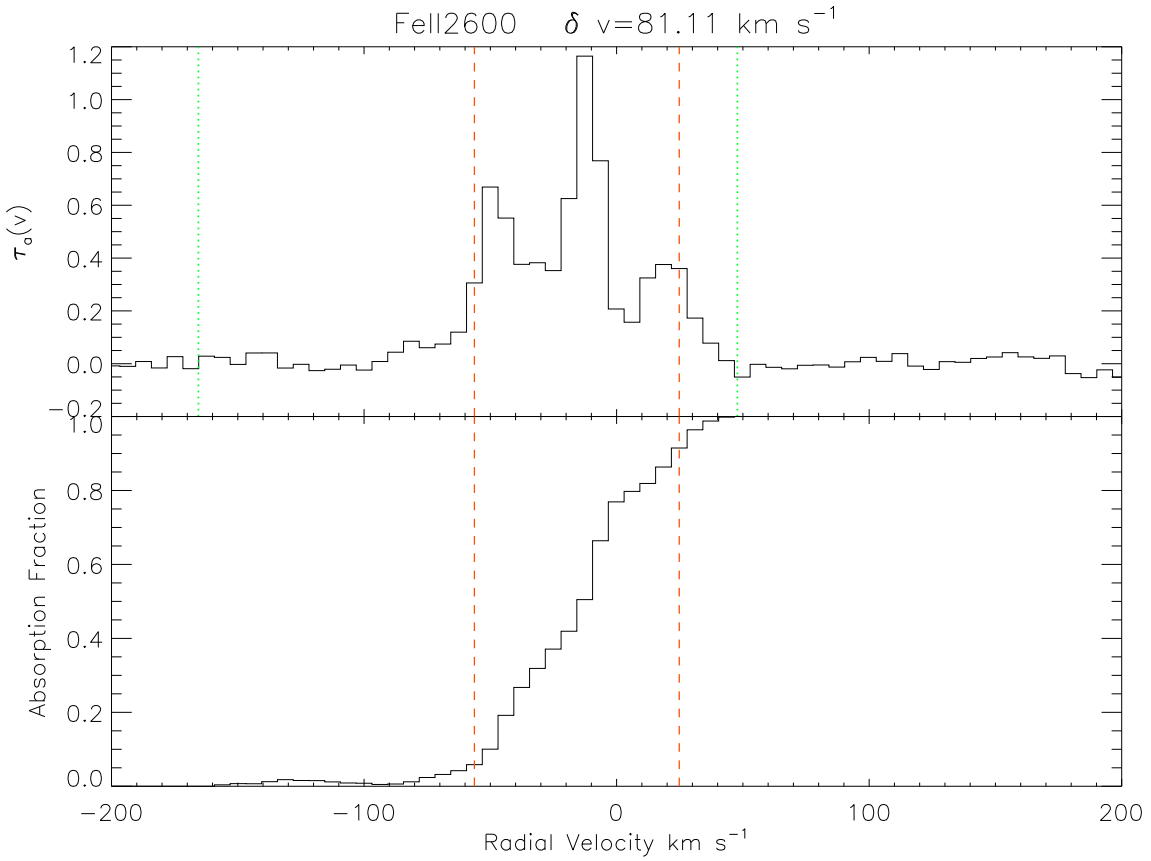

Figure 4.8 Determination of velocity dispersion for the $z = 1.839$ sub-DLA towards Q1311-0120. The upper panel shows the apparent optical depth profile for the Fe II λ 2600 line selected for the measurement of ΔV_{90}. The lower panel shows the corresponding integrated apparent optical depth. The dashed vertical green lines represent the limits of integration while the vertical dashed orange lines indicate the region in velocity where 90 % of the absorption takes place.

these systems compared to DLAs. A linear regression fit for the sub-DLAs gives

$$[X/H] = (0.70 \pm 0.07)\, log\, \Delta v_{90} - (1.54 \pm 0.14), \tag{4.5}$$

while a fit to the DLA data yields a slope of 1.11±0.03 and an intercept -3.40±0.06. The two slopes are different at $> 5\sigma$ level suggesting different mass-metallicity relations obeyed by the populations of galaxies traced by sub-DLAs and DLAs. If galaxies detected in absorption follow mass-metallicity relations similar to what seen for galaxies in emission, our results suggest that sub-DLAs and DLAs trace distinct

Table 4.1 Velocity width values for the absorbers in our sample.

QSO	z_{abs}	[Zn/H]/ [S/H]	Δv_{90} km s^{-1}	Selected transition line
Q1039-2719	2.1390	-0.02 ± 0.17	70	Fe II λ 2374
Q1103-2645	1.8390	<-0.82	81	Fe II λ 2600
Q1311-0120	1.7620	>-0.04	152	Fe II λ 2374
Q1551+0908	2.3200	<-0.95	32	Fe II λ 2344
Q2123-0050	2.0580	$+0.25\pm0.12$	321	Fe II λ 2344
Q0154+0448	0.1602	$+0.22\pm0.15$	152	Fe II λ 1082
Q0441+4313	0.1012	$+0.26\pm0.15$	275	P II λ 1153
Q0456-2159	0.4744	$+0.45\pm0.04$	155	S II λ 1250
Q2131-1207	0.4297	-0.01 ± 0.09	92	S II λ 1259

populations of galaxies and metal rich sub-DLAs are likely to trace more massive galaxies compared to DLAs.

4.8 C II* Absorption and Cooling Rate

Most of the cooling in the Milky Way's interstellar medium takes place through the fine-structure line emission of [C II] λ158 μm. This line arises from the $^2P_{3/2}$ to $^2P_{1/2}$ transition in the ground state $2s^2\,2p$ term of C II. Following Pottasch, Wesselius, & van Duinen (1979), the rate of cooling per H atom in gas detected in absorption can be expressed as:

$$l_c = \frac{N_{CII^*} h\nu_{ul} A_{ul}}{N_{HI}} \;\; ergs \;\; s^{-1}, \tag{4.6}$$

where N_{CII^*} is the column density of the C II ions in the $2P_{3/2}$ state, N_{HI} is the H I column density, while $h\nu_{ul}$ and A_{ul} are the energy of the $^2P_{3/2}$ to $^2P_{1/2}$ transition and coefficient for spontaneous photon decay, respectively. UV transitions of C II* λ1335.7 and Lyα λ1215.7 can be used to infer N_{CII^*} and N_{HI}, respectively, for the determination of l_c in the interstellar medium detected in absorption.

Our data shows the presence of C II* λ1335.7 in the sub-DLAs toward Q1039-2719, Q1103-2645 and Q2123-0050. However, this line is partially blended with C IIλ1334 in

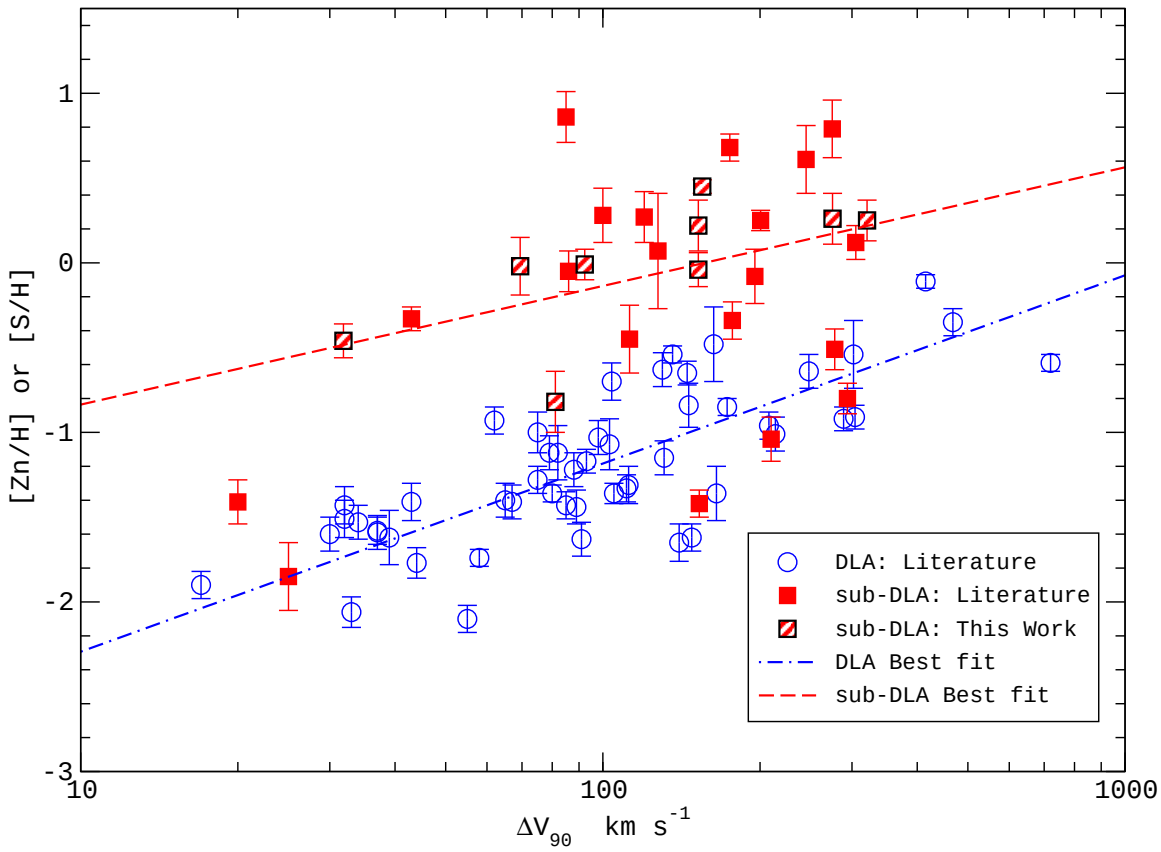

Figure 4.9 Velocity dispersion (ΔV_{90}) vs. Metallicity relations for sub-DLAs and DLAs. Linear regression fits to the sub-DLA and DLA data are shown as dashed and dashed-dotted lines respectively.

Q1039-2719 and Q2123-0050 (see Figures 3.4 and 3.8, respectively) while for Q1103-2645, it is partially blended with a Lyα forest feature. As a result, only a lower limit on N_{CII^*} could be placed for each of these absorbers. However, the absorption profile structures of these systems suggest that the true N_{CII^*} values are unlikely to be much higher than the corresponding lower limits. For the sub-DLAs toward Q1551+0908, Q0456-2159 and Q2131-1207, C II* λ1335.7 was not detected and we placed 3σ upper limits on N_{CII^*} based on the S/N near the line. Poor S/N in the region of the transition did not allow us an estimate of C II* abundance in the sub-DLA toward Q1311-0120. For Q0441+0448 and Q0441+4313, C II* was not covered in our spectra Table 4.2 lists the N_{CII^*} and the corresponding l_c values for the sub-DLAs in this

Table 4.2 Cooling rate values for the absorbers in this sample

QSO	log N_{HI} cm^{-2}	N_{CII^*} cm^{-2}	l_c ergs s^{-1} per H atom
Q1039-2719	19.55±0.15	$> 3.92 \times 10^{13}$	$> 3.33 \times 10^{-26}$
Q1103-2645	19.52±0.01	$> 8.53 \times 10^{12}$	$> 7.80 \times 10^{-27}$
Q1551+0908	19.70±0.05	$< 1.48 \times 10^{12}$	$< 8.93 \times 10^{-28}$
Q2123-0050	19.35±0.10	$> 6.60 \times 10^{13}$	$> 8.90 \times 10^{-26}$
Q0456-2159	19.45±0.02	$< 3.72 \times 10^{12}$	$< 3.98 \times 10^{-27}$
Q2131-1207	19.18±0.03	$< 7.08 \times 10^{12}$	$< 1.41 \times 10^{-26}$

sample.

The cooling rate versus H I column density data for these sub-DLAs are plotted in Figure 4.10, along with the corresponding measurements for DLAs from Wolfe et al. (2003) and for interstellar clouds in the Milky Way adopted from Lehner et al. (2004). The Milky Way's ISM measurements are shown separately for low, low+intermediate, intermediate, and high-velocity clouds. To the best of our knowledge, this work provides the first ever cooling rate estimates for sub-DLAs Although our measurements could only provide limits on the sub-DLA cooling rates, it can immediately be inferred from Figure 4.10 that, for some sub-DLAs, the interstellar cooling rate is higher than the entire DLA sample and similar to the values seen in Milky Way's interstellar clouds. Under the assumption of thermodynamic equilibrium in the absorbing gas, the interstellar cooling rate should equal the rate of energy production by star formation activity. Therefore, cooling rate can be used as an indicator for the star formation rate (SFR) in these absorbers. We also note that the sub-DLAs with high cooling rates are also near-solar or super-solar in metallicity. Unfortunately, for the two metal-rich sub-DLAs towards Q0456-2159 and Q2131-1207, we could not place sensitive upper limits on their cooling rates owing to the relatively low S/N in our HST spectra. It is also interesting to note that the sub-DLA towards Q1551+0908 seems to have the lowest cooling rate among the systems in our high S/N MIKE sample and it is also the most metal-poor absorber. Our results suggest that at least some metal-rich sub-DLAs may have higher SFRs compared to DLAs and that the

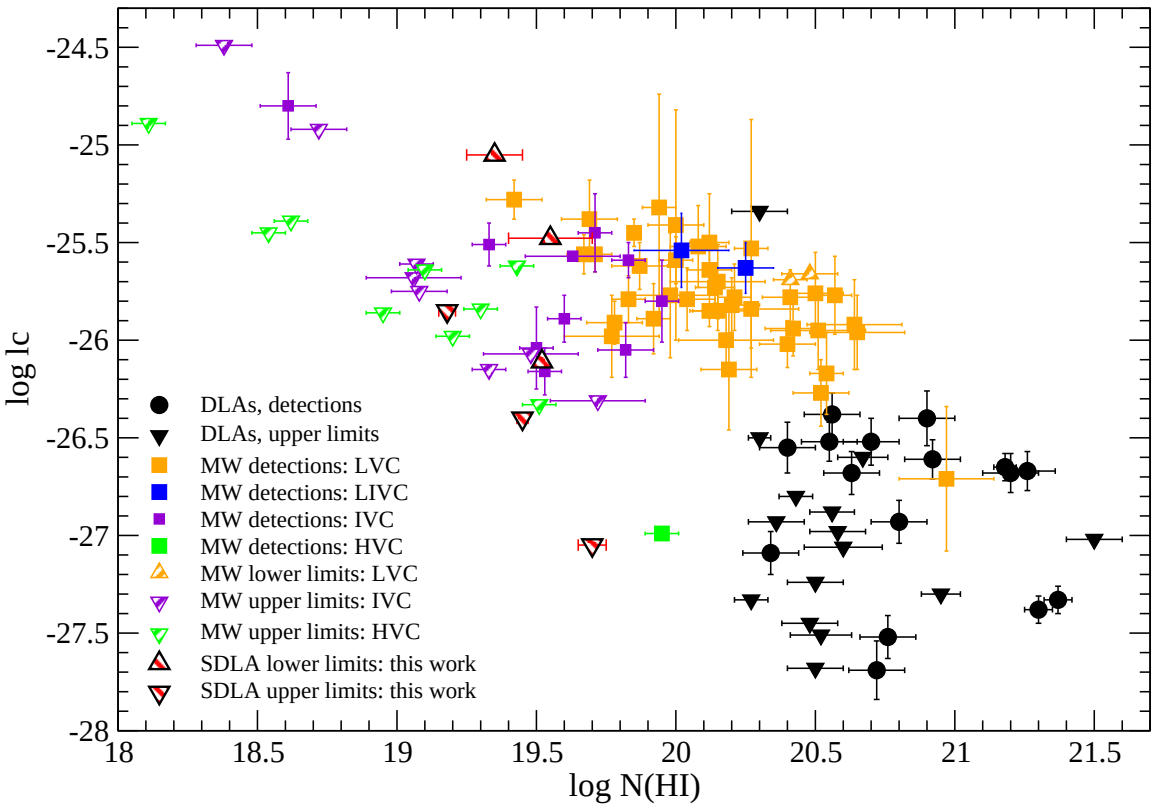

Figure 4.10 Cooling rate estimated from C II* absorption plotted vs. H I column density. The open red triangles represent the sub-DLAs from our sample. The filled black circles and triangles denote the sample of QSO DLAs in Wolfe et al. (2003). The filled squares and striped triangles represent the measurements for low, intermediate, low+intermediate, and high-velocity interstellar H I clouds in the Milky Way compiled in Lehner et al. (2004).

interstellar cooling rates in sub-DLAs may depend on metallicity. However, a detailed investigation of the metallicity dependence of cooling rate in sub-DLAs and the comparison of SFRs between DLAs and sub-DLAs warrant a much larger sample with precise column density determinations.

CHAPTER 5

Conclusions and Future Work

5.1 Conclusions

We studied sub-DLAs at $z < 0.6$ and $z > 1.5$ using spectra from HST-COS and Magellan-MIKE, respectively. Prior to this work, properties of sub-DLAs in these redshift regimes remained largely unexplored. Our observations have increased the sub-DLA metallicity sample at $z < 0.6$ by ~ 4 and added ~ 50 % more to the metallicity data at $z > 1.5$, providing improved constraints on the metallicity evolution of sub-DLAs at these redshift regimes. All of the low redshift sub-DLAs in our sample are found to be of near or super solar metallicity in agreement with the predictions from galactic chemical evolution models. Among the sub-DLAs observed at $z > 1.5$, one system at $z_{abs} = 1.76$ was found with [Zn/H]> -0.06 and, more surprisingly, two systems with [Zn/H]$= +0.25$ dex and [Zn/H]$= -0.02$ dex were found at $z_{abs} > 2$. These two systems are the most metal-rich sub-DLAs known so far at $z_{abs} \gtrsim 2$ and our observations suggest that metal-rich sub-DLAs appear at high redshifts as well. In addition to determining the S or Zn based metallicities for these absorbers, we measured abundances of various elements from our spectra. Combining our data with those for sub-DLAs from the literature, we studied various chemical and kine-

matic properties of the sub-DLA population as a whole and compared their behavior with that of DLAs. The main conclusions derived from this work are summarized as follows:

- DLAs and sub-DLAs show evolution in their N_{HI}-weighted mean metallicities over the redshift ranges for which their data are available ($0 < z \lesssim 5$ for DLAs and $0 < z \lesssim 3$ for sub-DLAs). At $0 < z \lesssim 3$, sub-DLAs, on average, have been found to be more metal-rich than DLAs and show metallicity evolution at a rate similar to that for DLAs. We also find that while metallicity evolution in DLAs does not resemble the expected mean trend for chemical enrichment in galaxies, the sub-DLA data are consistent with the chemical evolution models at all redshifts probed so far. We note that our study of the metallicity evolution in DLAs and sub-DLAs is based on the most comprehensive sample of depletion-free metallicity measurements.

- Simple photoionization calculations suggest that while there is a significant amount of ionized gas in some of our absorbers, the ionization corrections to the element abundances are relatively modest ($\lesssim$ 0.2 dex). Thus, ionization corrections cannot explain the high sub-DLA metallicities.

- The observed difference between the metallicities of DLAs and sub-DLAs can not be explain by the presence of a selection (based on strong metal lines) bias in the low-z samples. The high redshift samples are selected based on neutral gas absorption cross-section only, and therefore, should not have any effect of such a selection bias.

- For DLAs and sub-DLAs, the metallicity of the absorbing gas is anti-correlated with the H I column density. This anti-correlation is evident even for a non-homogeneous sample of metallicity measurements based on several different

heavy elements (Zn, S, Si, Fe). This provides evidence against the existence of a bimodal metallicity distribution in DLAs and sub-DLAs.

- DLA and sub-DLA absorbers show a correlation between metallicity (based on Zn) and depletion (estimated from the abundance ratio between Fe and Zn), suggesting that more metal-rich absorbers are also likely to have a higher dust-to-gas ratio. There could be a stronger dust obscuration bias for DLAs than for sub-DLAs if total dust content and therefore dust extinction depends strongly on metal column density.

- DLAs and sub-DLAs show different [Mn/Fe] vs. metallicity trends, suggesting different stellar populations in the galaxies traced by these two classes of absorbers.

- The velocity dispersion (Δv_{90}) vs. metallicity data for DLAs and sub-DLAs taken together appear to show a correlation suggesting that more massive absorber galaxies are likely to be more metal-rich as well. Furthermore, the Δv_{90} vs. metallicity relations for sub-DLAs and DLAs appear to be different from each other. If Δv_{90} is an indicator of the mass of the absorbing galaxy, then our finding suggests that the populations of galaxies traced by DLAs and sub-DLAs obey different mass-metallicity relations and that sub-DLAs are likely to trace more massive galaxies than DLAs.

- We present preliminary evidence that at least in the case of some metal-rich sub-DLAs, the interstellar cooling rate (and also possibly the SFR) can be higher than that seen in DLAs.

Thus, the DLA and sub-DLA quasar absorber line systems, in addition to the difference in their H I column densities, appear to be distinct from each other in various aspects such as metallicity, stellar populations and gas kinematics. It is very

likely that the gas-rich and metal-poor DLAs trace different populations of galaxies than the metal-rich but gas-poor sub-DLAs. It is possible that the sub-DLAs arise in more massive galaxies while DLAs represent gas-rich dwarf galaxies with low star formation rates. Continued study of the properties of DLA and sub-DLA quasar absorbers across cosmic time can thus give new insights into the processes driving galaxy evolution.

5.2 Future Work

Although significant progress has been made towards understanding the properties of DLA and sub-DLA absorbers, many questions remain open regarding their connection to galaxies at different epochs of cosmic evolution. The galaxies traced by DLAs and sub-DLAs seem to follow separate evolutionary tracks established as early as ~ 2 Gyrs after the Big Bang. However, given the similarities between their rates of metallicity evolution, the observed difference can extend further back in time. For a better understanding of early evolution in galaxies, it is essential to constrain the epoch when these different evolutionary tracks emerged. Although metallicity data for DLAs exist over $0 < z \lesssim 5$, sub-DLAs have not been explored at $z \gtrsim 3$. Therefore, one of the main priorities for our continuing study of quasar absorption line systems is to expand the redshift baseline for sub-DLA data much beyond $z \sim 3$. At the same time, samples of sub-DLAs and DLAs at $z < 0.6$ remain small. Observations of more sub-DLAs and DLAs at low redshifts are essential to shed further light on how these systems compare with their high-z analogs and with the Milky Way ISM, and how they evolve with time. The study of low redshift quasar absorbers is particularly interesting as it is easier to detect their host galaxies in emission, providing important clues to understand the galaxy-absorber relationship. Follow-up imaging and Integral Field Spectroscopy of DLAs and sub-DLAs have been actively

pursued in recent years but much more work is needed to arrive at a clear picture regarding the galaxy-absorber connection at low redshifts. Furthermore, such studies have the potential to be extended to higher redshifts in the upcoming exciting era of 30 meter class telescopes.

As discussed in section 4.2, the study of the effects of ionization on element abundances in sub-DLAs requires further attention. We plan to carry out photoionization modelling in a consistent manner on all systems in the literature. The aim for this study is to produce a homogeneous dataset of ionization-corrected abundances for sub-DLAs. This will help us to carry out a detailed investigation of ionization effects on the observed metallicity difference between DLAs and sub-DLAs. The uniform analysis will also help us to explore the redshift and H I column density variation of the ionization level in sub-DLAs.

Metallicity gradients within galaxies, if present, can also contribute towards metallicity variation along different sight lines. If the sub-DLA systems are sampled systematically by sightlines passing through more metal rich regions of galaxies compared to DLAs, metallicity difference between these two classes of quasar absorbers can exist even if they trace the same population of galaxies. This issue can be addressed with a study of the distribution of impact parameters (i.e., the projected distances of the sightline from the center of the galaxy hosting a DLA/sub-DLA) for DLAs and sub-DLAs. However, for two low-z sub-DLAs in our observed sample, our measurements of the absorption-line metallicities along the quasar sightlines are consistent with measurements (from the literature) of the emission-line metallicities near the centers of the foreground absorbing galaxies (Som et al., 2014). This suggests that metallicity gradients may not be significant in these galaxies. A study of impact parameter distribution, besides exploring possible metallicity gradients, can provide a statistical description of the structure of interstellar gas in absorber galaxies. This can be achieved through follow-up imaging for low redshift absorbers. A powerful

alternative is to study the detailed structure of individual galaxies using sightlines towards close quasar-pairs or gravitationally lensed quasars. Gravitationally lensed quasars (GLQ) or close quasar-pairs sample multiple sightlines at different impact parameters through foreground galaxies and observing these sightlines can provide information on the properties of interstellar gas in different regions of these galaxies. We have recently been awarded observing time with HST to study Lyman-α absorption properties along sightlines towards multiple low-z GLQs. For all of these GLQs, the lensing galaxy has been well detected in images and therefore, the impact parameters for each sightline is also known. For most of these GLQs, several metal absorption lines along each sightline have already been detected from ground based spectroscopy. The UV spectra from HST, once available, will be used in conjunction with the ground based data to provide detailed description of the properties of the lensing galaxies at multiple impact parameters.

Bibliography

Akerman C.J., Ellison S.L., Pettini M., Steidel C.C., 2005, A&A, 440, 449

Argast D., Samland M., Gerhard O.E., Thielemann F.-K., 2000, A&A, 356, 873

Asplund M., Grevesse N., Sauval A. J., Scott P., 2009, AR&A, 47, 481

Battisti A. J., Meiring J. D., Tripp T. M., Prochaska J. X., Werk J. K., Jenkins E. B., Lehner N., Tumlinson J., Thom C., 2012, ApJ, 744, 93

Bergeron J. 1986, A&A, 155, L8

Bergeron J., Boulade O., Kunth D., Tytler D., Boksenberg A., Vigroux L., 1988, A&A, 191, 1

Bernstein R., Schectman S. A., Gunnels S., Mochnacki S., Athey A., 2003 SPIE, 4841, 1694

Boissé P., Le Brun V., Bergeron J., Deharveng J. M., 1998, A&A, 333, 841

Bouche N., Murphy M. T., Pèroux C., Csabai I., Wild V., 2006, MNRAS, 371, 495

Bouché N., Lehnert M. D., Aguirre A., Péroux C., Bergeron J., 2007, MNRAS, 378, 525

Bouwens R. J., Illingworth G. D., Franx M., Ford H., 2007, ApJ, 670, 928

Cen R., Miralda-Escude J., Ostriker J.P., Rauch, M., 1994, ApJ, 437L,9

Cen R., Ostriker J.P., Prochaska J.X., Wolfe A.M., 2003, ApJ, 598, 741

Centurión M., Molaro P., Vladilo G., Péroux C., Levshakov S. A., D'Odorico V., 2003, A&A, 403, 55

Chen Y.Q., Nissen P.E., Zhao G., Zhang H.W., Benoni T., 2000, A&AS, 141, 491

Chen H-W., Lanzetta K. M., 2003, ApJ, 597, 706

Chen H. W., Kennicutt R. C., & Rauch M., 2005, ApJ, 620, 703

Christensen L., Schulte-Ladbeck R. E., Sanchez S. F., Becker T., Jahnke K., Kelz A., Roth M. M., Wisotzki L., 2005, A&A, 429, 477

Churchill C. W., Mellon R. R., Charlton J. C., Jannuzi B. T., Kirhakos S., Steidel C. C., Schneider D. P., 2000, ApJS, 130, 91

Churchill C. W., Vogt S. S., 2001, AJ, 122, 679

Davé R., Oppenheimer B. D., 2007, MNRAS, 374, 427

de la Varga A., Reimers D., Tytler D., Barlow T., Burles S., 2000, A&A, 363, 69

Dessauges-Zavadsky M., Péroux C., Kim T.-S., D'Odorico S., McMahon R. G., 2003, MNRAS, 345, 447

Dessauges-Zavadsky M., Ellison S. L., Murphy M. T., 2009, MNRAS, 396, L61

Ellison S. L., Lopez S., 2001, A&A, 380, 117

Erb D. K., Shapley A. E., Pettini M., Steidel C. C., Reddy N. A., Adelberger K. L., 2006, ApJ, 644, 813

Ferland G. J., Porter R. L., van Hoof P. A. M., Williams R. J. R., Abel N. P., Lykins M. L., Shaw G., Henney W. J., Stancil P. C., 2013, RMxAA, 49, 137

Fynbo J. P. U., Ledoux C., Noterdaeme P., Christensen L., Møller P., Durgapal A. K., et al., 2011, MNRAS, 413, 2481

Ge J., Bechtold J., Kulkarni V. P., 2001, ApJ, 547, L1

Gharanfoli S., Kulkarni V. P., Chun M. R., Takamiya M., 2007, ApJ, 133, 130

Gibson B.K., Fenner Y., Renda A., Kawata D., Lee H., 2003, PASA, 20, 401

Gratton R. G., Caretta E., Claudi R., Lucatello S., Barbieri M., 2004, A&A, 404, 187

Haardt F., Madau P., 1996, ApJ, 461, 20

Henry R. B. C., Edmunds M. G., Koppen J., 2000, ApJ, 541, 660

Holland S. T., et al. 2014, "Cosmic Origins Spectrograph Instrument Handbook, Version 6.0" (Baltimore: STScI)

Howk J.C., Sembach K.R., 1999, ApJ, 523, L141

Jenkins E.B., Bowen D.V., Tripp T.M., Sembach K.R., 2005, ApJ, 623, 767

Izotov Y. I., Thuan T. X., 2004, ApJ, 602, 200

Kaplan E.L., Meier P., 1958, JASA, 53, 282

Kaplan K. F., Prochaska J. X., Herbert-Fort S. Ellison S. L., Dessauges-Zavadsky M., 2010, PASP, 122, 619

Kanekar N., Chengalur J. N., Subrahmanyan R., Petitjean, P., 2001, A&A, 367, 46

Karakas A., Lattanzio J.C., 2007, PASA, 24, 103

Khare P., Kulkarni V. P., Lauroesch J. T., York D. G, Crotts P. S., Nakamura O., 2004, ApJ, 616, 86

Khare P., Kulkarni V. P., Péroux C., York D. G., Lauroesch J. T., Meiring J. D., 2007, A&A, 464, 487

Kim T.-S.,Carswell R.F., Cristiani S., D'Odorico S., Giallongo E., 2002, MNRAS, 335, 555

Kisielius R., Kulkarni V. P., Ferland G. J., Bogdanovich P., Lykins M. L., 2014, ApJ,

780, 76

Krumholz M. R., Ellison S. L., Prochaska J. X., Tumlinson J., 2009, ApJ, 701, L12

Kulkarni V. P., Bechtold J., Ge J., 1999, in Proc. ESO Workshop, Chemical Evolution from Zero to High Redshifts, ed. M. Rosa & J. Walsh (Berlin: Springer), 275

Kulkarni V. P., Fall S. M., 2002, ApJ, 580, 732

Kulkarni V. P., Fall S. M., Lauroesch J. T., York D. G, Welty D. E, Khare P., Truran J. W., 2005, ApJ, 618, 68

Kulkarni V. P., Khare P., Péroux C., York D. G., Lauroesch J. T., Meiring J. D., 2007, ApJ, 661, 88

Kulkarni V. P., Khare P., Som D., Meiring J., York D. G., Péroux C., Lauroesch J. T., 2010, NewA, 15, 735

Kulkarni V. P., Meiring J., Som D., Péroux C., York D. G., Khare P., Lauroesch J. T., 2012, ApJ, 749, 176

Lanzetta K. M., Turnshek D. A., Wolfe A. M., 1995, ApJ, 440, 435L

Ledoux C. Petitjean P., Møller P., Fynbo J., Srianand R., 2006, A&A, 457, 71

Lehner N., Wakker B. P., Savage B. D., 2004, ApJ, 615, 767

Lehner N., Howk J. C., Tripp T. M., Tumlinson J., Prochaska J. X., O'Meara J. M., Thom C., Werk J. K., Fox A. J., Ribaudo J., 2013, ApJ, 770 138

Lopez S., Reimers D., Rauch M., Sargent W. L. W., Smette A., 1999, ApJ, 513, 598

Lopez S., Reimers D., D'Odorico S., Prochaska J. X., 2002, A&A, 385, 778

Lopez S., Ellison S. L., 2003, A&A, 403, 573

Lu L., Savage B. D., Tripp T. M., Meyer D. M., 1995, ApJ, 447, 597

Lu L., Sargent W. L. W., Barlow T. A., Churchill C. W., Vogt S. S., 1996, ApJS, 107, 475

Madau P., Haardt F., Rees M.J., 1999, ApJ, 514, 648

Maiolino R., Nagao T., Grazian A., Cocchia F. et al., 2008, A&A, 488, 463

Massa D., York B. et al. 2013, "COS Data Handbook", Version 2.0, (Baltimore: STScI)

McWilliam A., Rich R. M., Smecker-Hane T. A., 2003, ApJ, 592, L21

Meiring J. D., Kulkarni V. P., Khare P., Bechtold J., York D. G., Cui J., Lauroesch J. T., Crotts A. P. S., Nakamura O., 2006, MNRAS,370, 43

Meiring J. D., Lauroesch J. T, Kulkarni V. P., Péroux C., Khare P., York D. G., Crotts A. P. S., 2007, MNRAS,376, 557

Meiring J. D., Kulkarni V. P., Lauroesch J. T., Péroux C., Khare P., York D. G., Crotts A. P. S., 2008, MNRAS,384, 1015

Meiring J. D., Kulkarni V. P., Lauroesch J. T., Péroux C., Khare P., York D.G., 2009, MNRAS, 393, 1513

Meiring J. D., Lauroesch, J. T., Kulkarni, V. P., Péroux C., Khare P., York, D. G., 2009, MNRAS, 397, 2037

Meyer D. M., York D. G., 1992, ApJ, 399, L121

Meyer D. M., Lanzetta K. M., Wolfe A. M., 1995, ApJ, 451, L13

Mihalas D., "Stellar Atmospheres", 1970, W.H. Freeman and Company, San Francisco, CA, USA

Momjian E., Carilli C. L., Walter F., Venemans B., 2014, AJ, 147, 6

Molaro P., Bonifacio P., Centurión M., DŎdorico S., Vladilo G., Santin P., Di Marcantonio P., 2000, ApJ, 541, 54

Morton D. C., 2003, ApJS, 149, 205

Nestor D. B., Rao S. M., Turnshek D. A., Vanden Berk D., 2003, ApJ, 595, L5

Nestor D. B., Pettini M., Hewett P. C., Rao S., Wild V., 2008, MNRAS, 390, 1670

Nissen P. E., Chen Y. Q., Schuster W. J., Zhao G., 2000, A&A, 353, 722

Nomoto, K., Iwamoto K., Nakasato N., Thielemann F.K., Brachwitz F., Tsujimoto T., Kubo, Y., Kishimoto, N., 1996, Nucl. Phys. A, A621, 467

Nomoto, K., Tominaga N., Umeda H., Kobayashi C., Maeda K., 2006, Nucl. Phys. A, 777, 424

Noterdaeme P., Ledoux C., Petitjean P., Srianand R., 2008, A&A, 481, 327

Noterdaeme P., Petitjean P., Ledoux C., Srianand R., 2009, A&A, 505, 1087

Oppenheimer, B. D., Davé, R., Katz, N., Kollmeier, J. A., Weinberg, D. H., 2012, MNRAS, 420, 829

Pagel B., "Nucleosynthesis and the Chemical Evolution of Galaxies", 1997, Cambridge University Press, Cambridge, UK

Peebles, P.J.E., "Principles of Physical Cosmology", 1976, Princeton University Press, Princeton, NJ, USA

Pei Y. C., Fall S. M., Hauser M. G., 1999, ApJ, 522, 604

Pei Y., Fall S.M., 1995, ApJ 454 69

Pei Y. C., Fall S. M., Hauser M. G., 1999, ApJ, 522, 604

Péroux C., Petitjean P., Aracil B., Srianand R., 2002, NewA, 7, 577

Péroux C., Dessauges-Zavadsky M., D'Orico S., Kim T. S., McMahon R., 2003, MNRAS, 345, 480

Péroux C., McMahon R.G., Storrie-Lombardi L.J., Irwin M.J., 2003, MNRAS, 346, 1103

Péroux C., Dessauges-Zavadsky M., D'Odorico S., Sun Kim T., McMahon R.G. MNRAS, 363, 479

Péroux C., Kulkarni V. P., Meiring J., Ferlet R., Khare P., Lauroesch J. T., Vladilo G., York D. G., 2006, A&A, 450, 53

Péroux C., Meiring J. D., Kulkarni V. P., Ferlet R., Khare P., Lauroesch J. T., Vladilo G., York D. G., 2006, MNRAS, 372, 369

Péroux C., Meiring J. D., Kulkarni V. P., Khare P., Lauroesch J. T., Vladilo G., York D. G., 2008, MNRAS, 386, 2209

Petitjean P., Webb J.K., Rauch M., Carswell R.F., Lanzetta K., 1993, MNRAS, 262, 499

Petitjean P.,Theodore B., Smette A., Lespine Y., 1996, A&A, 313, L25

Petitjean P., Srianand R., Ledoux C., 2000, A&A, 364, 26

Pettini M., Smith L. J., Hunstead R. W., King D. L., 1994, ApJ, 426, 79

Pettini M., King D.L., Smith L.J., Huntstead R.W., 1997, ApJ, 478, 536

Pettini M., Ellison S. L., Steidel C. C., Bowen D. V., 1999, ApJ, 510, 576

Pettini M., Ellison S. L., Steidel C. C., Shapley A. E., Bowen, D.V., 2000, ApJ, 532, 65

Pettini M., 2004, in Proc. XIII Canary Islands Winter School of Astrophysics, Cosmochemistry: The Melting Pot of Elements, Eds. C. Esteban, R. J. Garcí López, A. Herrero & F. Sánchez, 257

Pettini M., 2006, in "The Fabulous Destiny of Galaxies: Bridging Past and Present", Proceedings of the Vth Marseille International Cosmology conference, Eds. V. LeBrun, A. Mazure, S. Arnouts and D. Burgarella (Paris: Frontier Group), 319 (arXiv: astro-ph/0603066)

Pottasch S. R., Wesselius P. R., & van Duinen R. J., 1979, A&A, 77, 189

Prochaska J. X., Wolfe A. M., 1998, ApJ, 507, 113

Prochaska J. X., Wolfe A. M., 1999, ApJS, 121, 369

Prochaska J. X., Wolfe A. M., 2002, ApJ, 566, 68

Prochaska J. X., Gawiser E., Wolfe A. M., 2001, ApJ, 552, 99

Prochaska J.X., Howk J.C., O'Meara J.M., Tytler D., Wolfe A.M., Kirkman D., Lubin D., Suzuki N., 2002, ApJ, 571, 693

Prochaska J. X., Castro S., Djorgovski S. G., 2003, ApJS, 148, 317

Prochaska J. X., Gawiser E., Wolfe A. M., Cooke J., Gelino D., 2003, ApJS, 147, 227

Prochaska J. X., O'Meara J. M., Herbert-Fort S., Burles S., Prochter G. E., Bernstein R. A., 2006, ApJ, 648, L97

Rafelski M., Wolfe A. M., Prochaska J. X., Neeleman M., Mendez A. J., 2012, ApJ, 755, 89

Rafelski M., Neelman M., Fumagalli M., Wolfe A. M., Prochaska J. X., 2014, ApJ, 782, 29

Rao S. M., Turnshek D. A., 2000, ApJS, 130, 1

Rao S.M., Turnshek D.A., Nestor D.B., 2006, ApJ, 636, 610

Rao S. M., Prochaska J. X., Howk C., Wolfe A. M., 2005, AJ, 129, 9

Reddy B.E., Lambert D.L., Prieto C.A., 2006, MNRAS, 367, 1329

Reddy N., Steidel C. C., 2009, ApJ, 692, 778

Robertson J. G., Morton D. C., Blades J. C., York D. G., Meyer, D. M., 1988, ApJ, 325, 635

Rybicki G.B., Lightman A.P., "Radiative Processes in Astrophysics", 1979, Wiley and Sons, New York, New York, USA

Samland M., 1998, ApJ, 496, 155

Savage B.D., Sembach K.R., 1991, ApJ, 151, 313

Savage B.D., Sembach K.R., 1996, ApJ, 379, 245

Savage B.D., Sembach K.R., 1996, ARAA, 34, 279

Savaglio S., Glazebrook K., Le Borgne D., Juneau S., Abraham R. G., Chen H.-W., Crampton D., McCarthy P. J., Carlberg R. G., Marzke R. O., Roth K., Jrgensen I., Murowinski R., 2005, ApJ, 635, 260

Savaglio S., Rao A., Greiner J., et al. 2012, MNRAS, 420, 627

Schaye J., 2001, ApJ, 562, L95

Schaye J., 2006, ApJ, 643, 59

Searle L., Sargent W. L. W., 1972, ApJ, 173, 25

Shapley A. E., Erb D. K., Pettini M., Steidel C. C., Adelberger K. L., 2004, ApJ, 612, 108

Shu F., "The Physics of Astrophsics", 1991, University Science Books, Mill Valley, Ca, USA

Som D., Kulkarni V. P., Meiring J., York D. G., Péroux C., Khare P., Lauroesch J. T., 2013, MNRAS, 435, 1469

Som D., Kulkarni V. P., Meiring J., York D. G., Péroux C., Lauroesch J. T., Aller M. C., Khare P., 2014, submitted to ApJ

Somerville R. S., Primack J. R., Faber S. M., 2001, MNRAS, 320, 504

Spitzer L., "Physical Processes in the Interstellar Medium", 1978, Wiley & Sons, New

York, New York, USA

Springel V., White S.D.M., Jenkins A., Frenk C.S., Yoshida N., Gao L., Navarro J., Thacker R., et al., 2004, Nature, 425, 629

Srianand R., Petitjean P., 2000, A&A, 357, 414

Srianand R., Petitjean P., 2001, A&A, 373, 816

Storrie-Lombardi L.J., Wolfe A.M., 2000, ApJ, 543, 552

Thorne A.P., Litzen U., Johansson S., "Spectrophysics", 1999, Springer, Berlin, Germany

Timmes, F. X., Woosley S.E., Weaver T.A., 1995, ApJS, 96, 617

Tremonti C. A., Heckman T. M., Kauffmann G. et al. 2004, ApJ, 613, 898

Turnshek D. A. et al. 2005, in Proc. IAU Colloquium No. 199: Probing Galaxies through Quasar Absorption Lines, ed. P. R. Williams, C. Shu, & B. Ménard, 104

van den Bergh S., Tammann G., 1991, ARAA, 29, 363

van den Hoek L. B., Groenewegen M. A. T., 1997, A&AS, 123, 305

Van Zee L., Salzer J. J., Haynes M. P., 1998, ApJ, 497, L1

Van Zee L., Haynes M. P., 2006, ApJ, 636, 214

Vidal-Madjar A., Laurent C., Bonnet R. M., York, D. G, 1977, 211, 91

Vila-Costas M. B., Edmunds M. G., 1993, MNRAS, 265, 199

Vladilo G., Centurión M., Bonifacio P., Howk C., 2001, ApJ, 557, 1007

Vladilo G., Péroux C., 2005, A&A, 444, 461

Welty D. E., Hobbs L. M., York D.G., 1991, ApJS, 75, 425

Welty D. E., Lauroesch J. T., Blades C., Hobbs L. M., York D. G., 2001, ApJ, 554, 75

Weymann R. J., Williams R. E., Peterson B. M., Turnshek D. A., 1979, ApJ, 234, 33

Wolfe A. M., Lanzetta K. M., Foltz C. B., Chaffee F. H., 1995, ApJ, 454, 698

Wolfe A. M., & Prochaska, J. X., 1998, ApJ, 494, L15

Wolfe A. M., Gawiser E., Prochaska J. X., 2003, ApJ, 593, 235

Woosley S.E., Heger A., Weaver T.A., 2002, Rev. of Mod. Phys., 74, 1015

York D. G., & Kinahan B. F., 1979, ApJ, 228, 127

York D.G., Adelman J., Anderson J. E., et al. 2000, AJ, 120, 1579

York D. G., Khare P., Vanden Berk D., Kulkarni V. P., et al. 2006, MNRAS, 367, 945

Zafar T., Péroux C., Popping A., Millard B., Deharveng J. -M., Frank S., 2013, A&A, 556, 141

Zafar T., Centurion M., Péroux C., et al. 2014, MNRAS, submitted

Zhang Y., Meiksin A., Anninos P., Norman, M.L., 1998, ApJ, 495, 63

Zheng, W., Kriss, G.A., Telfer, R.C., Grimes, J.P., Davidsen, A.F., ApJ, 475, 469

Zwaan M., Walter F., Ryan-Weber E., Brinks E., de Blok W. J. G., Kennicutt R. C., 2008, AJ, 136, 2886

APPENDIX A

The Cosmological Redshift

Observationally, the redshift is measure of how much the wavelength of light from an object shift towards the red end of the spectrum during its passage to the observer. In terms of Cosmology, the redshift is a parametric representation of the expansion of the Universe. Considering the Friedmann-Robertson-Walker-Lemaître (FRWL) metric (see, e.g., Peebles 1976) a radially moving light ray ($ds \equiv 0$) can be described as

$$dt^2 = a^2(t)\frac{dr^2}{1-kr^2}, \tag{A.1}$$

where k is the curvature parameter and $a(t)$ is the dimensionless scale factor of expansion. For the crest of a light wave emitted from some galaxy at a distance $r = r_1$ and time $t = t_1$ and reaching us at $r = 0$ and $t = t_0$, we can write

$$\int_{r_1}^{0} \frac{dr}{\sqrt{1-kr^2}} = \int_{t_1}^{t_0} \frac{dt}{a(t)}. \tag{A.2}$$

Now, if wavelength of the emitted light is λ_{rest} and that of the observed light is λ_{obs}, then the next wave crest leaves the same galaxy at time $t_1 + (\lambda_{rest}/c)$ and reaches the observer at time $t_0 + (\lambda_{obs}/c)$. Therefore,

$$\int_{r_1}^{0} \frac{dr}{\sqrt{1-kr^2}} = \int_{t_1+\frac{\lambda_{rest}}{c}}^{t_0+\frac{\lambda_{obs}}{c}} \frac{dt}{a(t)}. \tag{A.3}$$

Subtracting equation A.2 from A.3 and assuming $a(t)$ remains unchanged over a small time interval $\delta t = \lambda/c$ we obtain,

$$\frac{\lambda_{obs}}{a(t_0)} = \frac{\lambda_{rest}}{a(t_1)}. \tag{A.4}$$

The cosmological redshift is defined as

$$z = \frac{\lambda_{obs} - \lambda_{rest}}{\lambda_{rest}}. \tag{A.5}$$

Combining equations A.4 and A.5 we get the relation between the observed redshift z and the scale factor $a(t)$ as

$$z = \frac{a(t_0)}{a(t_1)} - 1. \tag{A.6}$$

In other words, the ratio of the sizes of the Universe at the epochs of emission and detection of the photon is given by $1 + z$. For an expanding Universe, the ratio is positive and therefore, redshift can also be viewed as the stretching of the light wave during its propagation due to the expansion of the Universe. The cosmological redshift can also be thought of as resulting from the recessional velocity of the source, i.e., it can be identified with the Doppler redshift which is given by

$$\lambda_{obs} = \lambda_{rest}\sqrt{\frac{1+\beta}{1-\beta}}, \tag{A.7}$$

where, $\beta = (v/c)$ and v is the apparent speed of the source being observed relative to the observer. For very small velocities $v << c$, the redshift can be written simply as

$$z = \frac{\lambda_{obs} - \lambda_{rest}}{\lambda_{rest}} = \frac{v}{c}. \tag{A.8}$$

APPENDIX B

Solar System Abundances

Table B.1 Solar system abundances (from Asplund et al. 2009), in logarithmic units, for various elements commonly seen in the ISM.

Element	Solar Abundance Relative to H
He	-1.07
C	-3.57
N	-4.17
O	-3.31
Na	-5.76
Mg	-4.40
Al	-5.55
Si	-4.49
P	-6.59
S	-4.88
Cl	-6.50
Ar	-5.60
Ca	-5.66
Ti	-7.05
Cr	-6.36
Mn	-6.57
Fe	-4.50
Co	-7.01
Ni	-5.78
Cu	-7.81
Zn	-7.44